



HERSCHEL/HIFI SPECTRAL MAPPING OF C⁺, CH⁺, AND CH IN ORION BN/KL: THE PREVAILING ROLE OF ULTRAVIOLET IRRADIATION IN CH⁺ FORMATION

PATRICK W. MORRIS¹, HARSHAL GUPTA^{1,2}, ZSOFIA NAGY^{3,4}, JOHN C. PEARSON⁵, VOLKER OSSENKOPF-OKADA³, EDITH FALGARONE⁶,
DARIUSZ C. LIS^{7,8}, MARYVONNE GERIN⁶, GARY MELNICK⁹, DAVID A. NEUFELD¹⁰, AND EDWIN A. BERGIN¹¹

¹ California Institute of Technology, NASA Herschel Science Center, IPAC M/C 100-22, Pasadena, CA 91125, USA; pmorris@ipac.caltech.edu

² Division of Astronomical Sciences, National Science Foundation, 4201 Wilson Boulevard, Suite 1045, Arlington, VA 22230, USA

³ I. Physikalisches Institut, Universität zu Köln, Zùlpicher Str. 77, D-50937 Köln, Germany

⁴ Department of Physics and Astronomy, University of Toledo, 2801 West Bancroft Street, Toledo, OH 43606, USA

⁵ California Institute of Technology, Jet Propulsion Laboratory, 4800 Oak Grove Drive, Pasadena, CA 91109, USA

⁶ LERMA, Observatoire de Paris, PSL Research University, CNRS, Sorbonne Universités, UPMC Univ. Paris 06, École normale supérieure, F-75005, Paris, France

⁷ LERMA, Observatoire de Paris, PSL Research University, CNRS, Sorbonne Universités, UPMC Univ. Paris 06, F-75014, Paris, France

⁸ California Institute of Technology, Cahill Center for Astronomy and Astrophysics M/C 301-17, Pasadena, CA 91125, USA

⁹ Harvard-Smithsonian Center for Astrophysics, 60 Garden Street, Mail Stop 66, Cambridge, MA 02138, USA

¹⁰ Department of Physics and Astronomy, Johns Hopkins University, 3400 North Charles Street, Baltimore, MD 21218, USA

¹¹ Department of Astronomy, University of Michigan, 500 Church Street, Ann Arbor, MI 48109, USA

Received 2015 December 31; revised 2016 March 22; accepted 2016 April 18; published 2016 September 14

ABSTRACT

The CH⁺ ion is a key species in the initial steps of interstellar carbon chemistry. Its formation in diverse environments where it is observed is not well understood, however, because the main production pathway is so endothermic (4280 K) that it is unlikely to proceed at the typical temperatures of molecular clouds. We investigate the formation of this highly reactive molecule with the first velocity-resolved spectral mapping of the CH⁺ $J = 1-0$, $2-1$ rotational transitions, three sets of CH Λ -doubled triplet lines, ¹²C⁺ and ¹³C⁺ $^2P_{3/2}-^2P_{1/2}$, and CH₃OH 835 GHz E-symmetry Q-branch transitions, obtained with *Herschel*/HIFI over a region of ≈ 12 arcmin² centered on the Orion BN/KL source. We present the spatial morphologies and kinematics, cloud boundary conditions, excitation temperatures, column densities, and ¹²C⁺ optical depths. Emission from all of C⁺, CH⁺, and CH is indicated to arise in the diluted gas, outside the explosive, dense BN/KL outflow. Our models show that UV irradiation provides favorable conditions for steady-state production of CH⁺ in this environment. Surprisingly, no spatial or kinematic correspondences of the observed species are found with H₂ $S(1)$ emission tracing shocked gas in the outflow. We propose that C⁺ is being consumed by rapid production of CO to explain the lack of both C⁺ and CH⁺ in the outflow. Hence, in star-forming environments containing sources of shocks and strong UV radiation, a description of the conditions leading to CH⁺ formation and excitation is incomplete without including the important—possibly dominant—role of UV irradiation.

Key words: astrochemistry – ISM: abundances – ISM: clouds – ISM: lines and bands – ISM: molecules – molecular processes

1. INTRODUCTION

The diatomic hydrides CH and CH⁺ were, along with CN, the first molecules to be identified from their optical absorption spectra in diffuse molecular clouds, some 75 years ago (McKellar 1940; Adams 1941; Douglas & Herzberg 1941). Advances in detector technologies and observing techniques now make the optical lines readily observable toward bright background stars (e.g., Crane et al. 1995; Zsargó & Federman 2003; Le Petit et al. 2004; Shaw et al. 2006; Nehmé et al. 2008; Boissé et al. 2009), yet fundamental carbon chemistry involving C⁺, CH, and CH⁺ in interstellar gas is not well enough understood to explain the observed abundances of CH⁺ in particular. The standard gas-phase model with a chemistry in which heating is provided by a background far-ultraviolet (FUV) field from hot stars generally works well for matching the abundances of CH observed in photon-dominated regions (PDRs), but falls short by orders of magnitude for CH⁺ (van Dishoeck & Black 1986; Gredel et al. 1993; Crane et al. 1995; Gredel 1997; Pan et al. 2004, 2005; Sheffer et al. 2008; Godard et al. 2009).

Direct formation pathways involving C⁺, H, and H₂ fail to explain the high abundances of CH⁺. First, the radiative association between C⁺ and H is too slow at the typical

temperatures of molecular clouds: the rate coefficient of the process $C^+(^2P_{3/2,1/2}) + H(^2S_{1/2}) \rightarrow CH^+(^1\Sigma^+) + h\nu$ was calculated by Kramers & Ter Haar (1946) and Bates (1951) to be around 2×10^{-18} cm³ s⁻¹ at 100 K, a few orders of magnitude too low to yield the observed abundances. More detailed calculations involving coupling between spin-orbit and rotational states were carried out by Graff et al. (1983) and Barinovs & van Hemert (2006) over temperatures up to 1000 K, but the rate increases significantly only at temperatures below 1 K, where the frequency of resonances in the radiative association rate coefficients increases substantially. Second, the reaction of C⁺ with molecular hydrogen, $C^+ + H_2 \rightarrow CH^+ + H$, is highly endothermic ($-\Delta E/k = 4280$ K; Hiel et al. 1997), requiring high gas temperatures, which likely result from non-equilibrium processes, or a reservoir of H₂ vibrationally excited by FUV fluorescence (Sternberg & Dalgarno 1995). Additionally, the reaction must proceed fast enough to counteract the high destruction rate of CH⁺ by collisions with H₂, H, and electrons.

The observed mean column density of CH⁺, $\log_{10}[N(\text{CH}^+)/N(\text{H})] = -8.11 \pm 0.33$, in the interstellar medium (ISM) (from a compilation of references by Godard & Cernicharo 2013) has been proposed to trace production through non-equilibrium processes, as may arise in relatively low-velocity (~ 10 km s⁻¹)

magnetohydrodynamic (MHD) waves and C-type shocks, turbulent mixing, or dissipation of turbulence. The importance of CH_n^+ chemistry in MHD shocks for the abundances of CH, OH, and HCO^+ in warm diffuse clouds was emphasized by Draine & Katz (1986a, 1986b) and Flower & Pineau des Forêts (1998), although both neutral and MHD shocks in the ISM have been disfavored in some observations (Gredel et al. 1993; Crawford 1995). Draine et al. (1983) had earlier pointed out that ion–neutral drift in MHD waves preferentially helps drive endothermic ion–neutral reactions in molecular clouds, not just by raising the temperature but also by increasing the collision energies to values $\gg kT$. Zsargó & Federman (2003) have also addressed the effects of non-thermal CH^+ chemistry on C-bearing molecules in diffuse clouds with low molecular abundances. In the turbulent dissipation region (TDR) model of Godard et al. (2009), the abundances of CH^+ , SH^+ , CN, H_2O , and many other molecules rise by more than two orders of magnitude when the activation barriers are overcome, as gas is heated via ion–neutral friction in the magnetized structure of a turbulent dissipative burst and during the subsequent relaxation period. This model has been applied by Falgarone et al. (2010) to observations of the CH^+ ground-state rotational ($J = 1-0$) transition in emission and absorption toward the bright massive star-forming region DR 21(OH), providing evidence that non-equilibrium chemistry successfully explains the high CH^+ abundances without overproduction of other molecules.

In denser gas around star-forming regions with strong FUV radiation fields and in PDRs, the internal energy of vibrationally excited H_2 ($\nu > 0$) can overcome the high activation barrier to form CH^+ (Sternberg & Dalgarno 1995; Hierl et al. 1997; Agúndez et al. 2010). Indeed the CH^+ intensities up to $J = 6-5$ observed in the Orion Bar have been reproduced by Nagy et al. (2013) with PDR models involving collisions of C^+ with vibrationally excited H_2 . Their results indicate that the CH^+ abundance peaks in the warm, high-pressure ($T \approx 500-1000$ K; $p/k = 10^8 \text{ cm}^3 \text{ K}$) surface regions of the PDR. Godard & Cernicharo (2013) have modeled the complete energy structure of CH^+ during formation, treating pumping of the vibrational and bound and unbound electronic states over all levels and including non-reactive collisions with H, H_2 , He, and electrons. Their results show that chemical pumping or formation in excited states drives the distribution over its rotational levels, while both photodissociation and radiative pumping of bound states have only a minor influence on the distribution. One of the surprising consequences of their results is that the intensities of the rotational lines of CH^+ observed toward the Orion Bar and the NGC 7027 PDRs are reproduced with H densities one to two orders of magnitude lower than those inferred from previous excitation models.

It is important to stress that while the reaction of C^+ with H_2 is the main production route to CH^+ , it can operate through the different mechanisms mentioned above in different environments, i.e., with H_2 in different excited states (e.g., Hierl et al. 1997; Agúndez et al. 2010; Zanchet et al. 2013). In diffuse gas of the ISM with H densities of a few tens to a few hundreds per cubic centimeter, the route is dominated by the intermittent dissipation regions of turbulence. In star-forming regions where warm and dense molecular material is exposed to FUV radiation or shocked outflows, reactions may proceed much faster because C^+ and vibrationally excited H_2 are both abundant. In either scenario, CH^+ is produced with an excess energy, and should be rapidly destroyed by reacting with H_2

and electrons. Hence the distribution of the population in the rotational levels may not be at equilibrium, depending on the environment and dominant formation pathway, i.e., in TDRs, or through UV- or shock-driven chemistries in denser molecular clouds. Until now, there have been very few opportunities to study the physical characteristics of CH^+ in dense clouds of star-forming regions (SFRs), in relation to shock-heated versus UV-irradiated gas.

Observations of the two lowest rotational transitions of CH^+ have been made possible with the Heterodyne Instrument for the Far Infrared (HIFI: de Graauw et al. 2010; Roelfsema et al. 2012), which flew on board the *Herschel Space Observatory* (Pilbratt et al. 2010). The majority of these observations were taken in single pointings or as spatially composite measurements. As such, radial velocity measurements are the only means to differentiate between ISM components in these observations. The nearby Orion Molecular Cloud 1 (OMC 1) surrounding the BN/KL massive SFR offers a varied and complex environment in which to study the characteristics of the CH^+ molecule. The embedded BN/KL SFR is the second most luminous site of star formation in the OMC and exhibits evidence for an energetic outburst, possibly the result of a stellar merger some 500–1000 years ago (Bally & Zinnecker 2005; Bally et al. 2011; Zapata et al. 2011). The feature is observed as loosely collimated bipolar outflows producing H_2O masers (Genzel et al. 1981; Genzel & Stutzki 1989; Greenhill et al. 1998), shock-excited H_2 (Beckwith et al. 1978), and high- J CO and various other molecules with broadened line wings (Kwan & Scoville 1976; Zuckerman et al. 1976; Erickson et al. 1982; Chermin & Wright 1996). The striking butterfly-shaped H_2 outflow is extended over ~ 30 arcsec (0.4 pc at a distance of 420 pc; Hirota et al. 2007; Menten et al. 2007) in a NW–SE direction, tracing the faster ($30-100 \text{ km s}^{-1}$) of the two outflows detected from H_2O maser emission by Genzel et al. (1981). We should naturally expect that H_2 excited to sufficient vibrational or rotational levels in gas heated by the powerful molecular outflow (or more accurately an explosive, momentum-driven outburst; e.g., Bally & Zinnecker 2005) will react with C^+ , if also present, to form CH^+ . In Orion BN/KL we must account for the strong extended thermal continuum emission from heated dust.

The principal aim of this paper is to investigate the spatial, kinematic, and physical conditions in the C^+ and CH^+ gas around Orion BN/KL, and their relations to the vibrationally excited H_2 emission, allowing us to further describe the conditions that lead to the endothermic formation of CH^+ . The intermediate-frequency (IF) coverage of our CH^+ $J = 1-0$ observations includes several CH_3OH ground-state E-symmetry transitions, allowing us to trace the regions of highest density where dust grain evaporation is presumed to be taking place (Caselli et al. 1993). We also present spectral maps of the $\text{CH } ^2\Pi_{3/2}-^2\Pi_{1/2}$ triplet lines at 537 GHz, and fixed-position observations of the $^2\Pi_{3/2}-^2\Pi_{3/2}$ (1471/1477 GHz) and $^2\Pi_{5/2}-^2\Pi_{3/2}$ (1657/1661 GHz) triplets toward the dense Hot Core. The formation of CH is believed to occur where both C^+ and excited H_2 are abundant and can react by radiative association in a UV-driven chemistry (Black & Dalgarno 1973). When collision temperatures are below 400 K, radiative association between C^+ and H_2 proceeds slowly to produce CH_2^+ , which reacts with H_2 to produce CH_3^+ , subsequently forming CH_2 , CH, and C by dissociative electronic recombination of CH_3^+ and CH_2^+ , and CH^+ by photodissociation of CH_3^+

(e.g., Godard et al. 2009; Agúndez et al. 2010; Indriolo et al. 2010). In the dense gas of SFRs, CH abundances relative to CH^+ range from factors of 1 to 3 (Godard et al. 2012). In more diffuse, translucent gas where high abundances of CH^+ are observed, non-thermal CH^+ chemistry may be important for production of CH and CO, as shown by Zsargó & Federman (2003). Their results suggest that non-thermal chemistry is necessary to account for the observed abundance of CH in these clouds, where on average some 30%–40% (but as much as 90%) of the observed CH along some sightlines has been attributed to originating from non-equilibrium synthesis of CH^+ . A linear relation between CH and H_2 column densities, $N(\text{CH}) = 3.5 \times 10^{-8} N(\text{H}_2)$, has been derived by Sheffer et al. (2008) to A_V of around 5 mag. In steady-state chemical models, on the other hand CH traces H_2 at hydrogen densities greater than about 100 cm^{-3} (Liszt & Lucas 2002; Levrier et al. 2012). Thus in warm and dense environments such as Orion BN/KL, the relationship between H_2 and CH could be more complex, because the abundances of CH may be at least partially a result of radiative association between C^+ and H_2 , which are more abundant in this environment than in the ISM.

2. OBSERVATIONS AND DATA REDUCTION

The observations presented here were obtained with the HIFI instrument, principally using the on-the-fly (OTF) spectral mapping mode, centered approximately on the BN source, as shown schematically in Figure 1. Most maps employ both the High Resolution Spectrometer (HRS) and the Wide Band Spectrometer (WBS). The nominal WBS resolution of 1.1 MHz, with a channel spacing of 0.5 MHz, provides a maximum velocity resolution of $\sim 0.2 \text{ km s}^{-1}$ at 1900 GHz and 0.7 km s^{-1} at 835 GHz, resolving all lines of interest to this study. At 835 GHz in band 3a, $\text{CH}_3\text{OH } K = 5 \rightarrow 4$ Q-branch torsional ground-state ($v_t = 0$) transitions with $J_{u,l} = 5$ through 18 are contained in the lower sideband within the 4.0 GHz IF range. Since HRS and WBS noise is correlated (using the same mixer assemblies), co-addition of those data does not improve data quality, thus we present only the WBS observations here. The $\text{C}^+ \ ^2P_{3/2} - ^2P_{1/2}$ maps at 1900.537 GHz and $\text{CH}^+ J = 1-0$ maps at 835.137 GHz were executed in calibration time by the HIFI Instrument Control Center for performance validations of the HIFI Astronomical Observing Templates. As summarized in Table 1, the observations have been acquired using each of the three calibration schemes available with the OTF mode, and Nyquist or half-beam spacing of the map points. While most maps were taken with scanning in a north–south direction, two maps were taken in an east–west direction for evaluation of non-uniform beam sampling effects and repeatability. The $^{12}\text{C}^+$ observations include the three $^{13}\text{C}^+ \ ^2P_{3/2} - ^2P_{1/2}$ fine-structure lines within the 2.4 GHz wide IF bandpass of band 7b.

We also include the analysis of spectral maps taken in the *Herschel* Observations of EXtraOrdinary Sources (HEXOS) Key Program (PI E. Bergin), which target water transitions and cover the $\text{CH}^+ J = 2-1$ triplet line at 1669.281 GHz and the $\text{CH } ^2\Pi_{3/2} - ^2\Pi_{1/2}$ triplet line at 537 GHz. The $\text{CH}^+ J = 2-1$ observation was carried out as a raster map using fast dual beam switching (DBS), which applies alternating nods of the telescope and chopping of the internal M3 pick-up mirror by $3'$ on the sky on either side of the mapped region for calibrations of the baseline. A chop frequency of 3.5 Hz and phase length of

0.14 s were timed for optimum stabilization of the baseline at this LO frequency. No contamination from $\text{CH}^+ J = 2-1$ emission or absorption has been detected in the alternated sky reference positions, by inspection of data from both nod positions processed through standing-wave corrections in the *Herschel* Interactive Processing Environment (HIPE) 14.0.

Every OTF observation includes measurements at a blank sky reference position, offset from the center of the map by typically $20'$. The reference measurement was taken to correct for the standing waves internal to the optical paths between the instrument mixer assemblies and the telescope secondary mirror, and electrical standing waves (ESWs) originating in the mixer amplifier chains at LO frequencies of 1897 GHz (C^+ mapping) and 1666 GHz ($\text{CH } ^2\Pi_{5/2} - ^2\Pi_{3/2}$ mapping). Spectra at the OFF positions were inspected for contamination, particularly from extended C^+ emission; however, no contaminations could be noticed within our adopted line detection criterion (described below) in the response-calibrated OFF data, or in the resulting spectral map, in the appearance of absorption at constant strength and velocity that would occur from a contaminated sky reference subtraction.

All data have been processed in the HIFI pipeline with HIPE, initially to Level 1 products using either version 13.0 or 14.0, which both include updated reconstruction of telescope pointing^{12,13}, and then using software and calibrations that correspond to the HIPE v14.0.1 User Release version. The WBS spectrum data sets at each map position were treated interactively to inspect for LO spurs or impurities, which might affect the calibration or measurements, and to remove other baseline artifacts prior to gridding the scans into spectral data cubes. Artifacts include standing waves and baseline offsets left as residuals of the reference sky subtraction in the pipeline. These residuals are generally associated with the mixer currents having drifted out of phase with the timing loops of the calibration measurement, and are most evident in data taken in HIFI bands 6 and 7, which have the shortest Allan times (Roelfsema et al. 2012). Data in these bands often exhibit non-sinusoidal standing waves with periods around 300 MHz that are electrical in origin (from the mixer amplifier chains). HIPE v13.0 (with updates in v14.0) includes corrections to the ESWs and accompanying baseline drift, successfully recovering source continuum levels, based on an algorithm that fits the ESWs from a mission-wide catalog of standing-wave patterns (Kester et al. 2014). The algorithm is susceptible to line-rich spectra, especially broad or complex profiles and absorption features, and we have verified that the ESW solutions applied to our observations were well treated with respect to selection of line-free baselines. All data were also inspected for optical (LO to mixer path) standing waves, typically dominated by a 93 MHz ripple, and treated where necessary with a sine-wave approximation using the HIPE task *fitHifiFringe*. Remaining residuals after fitting each scan in HIPE are mitigated in maps with more than one cycle of scans.

After baseline corrections, data from observations of the same transition (i.e., with overlapping sky frequency coverage), including the two polarizations, have been interactively merged into a single timeline product, and then into a single spectral cube for each of the upper and lower sideband frequency

¹² <http://herschel.esac.esa.int/twiki/bin/view/Public/ImprovedPointingGyro>

¹³ http://herschel.esac.esa.int/twiki/pub/Public/HifiCalibrationWeb/HIFI_PointingAccuracyNote.pdf

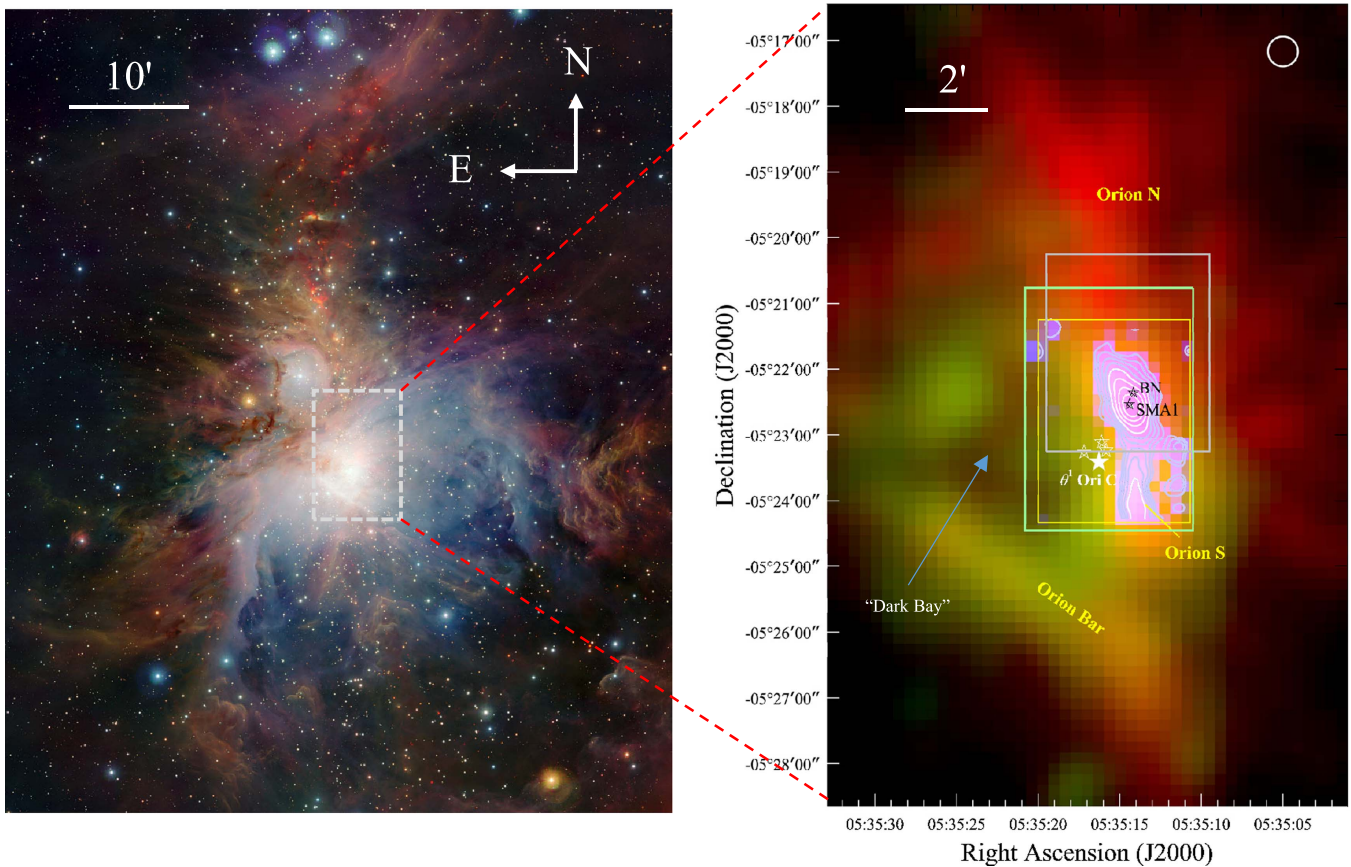


Figure 1. On the left, a wide-field composite image of M42 taken with the VIRCAM instrument on the European Southern Observatory’s Visible and Infrared Survey for Astronomy (VISTA) telescope at $2.15 \mu\text{m}$ (red), $1.25 \mu\text{m}$ (green), and $0.88 \mu\text{m}$ (blue) (credit: ESO/J. Emerson/VISTA). On the right, a composite image of OMC 1 using *Herschel*/SPIRE $350 \mu\text{m}$ (red), HIFI $\text{CH}^+ J = 1-0$ (green), and HIFI 1900 GHz ($158 \mu\text{m}$) continuum (light blue), each on a normalized intensity scale. Overlaid boxes indicate HIFI spectral mapping regions that are the subject of this study: C^+ (yellow), $\text{CH}^+ J = 1-0$ (green), and $\text{CH}^2\Pi_{3/2}-^2\Pi_{1/2}$ $1657/1661 \text{ GHz}$ and $\text{CH}^+ J = 2-1$ (gray). Continuum contours in light blue and white indicate the upper 50% and 30% of emitted power, respectively, within the indicated region of C^+ mapping. The HIFI beam size of $25''.3$ half-power beam width at 835 GHz corresponding to the $\text{CH}^+ J = 1-0$ observations is represented in the top corner of the *Herschel* composite image. The SPIRE beam at $350 \mu\text{m}$ (850 GHz) is very similar, $23''.9$ FWHM. The $7.5 \times 10'$ $\text{CH}^+ J = 1-0$ map is from the Open Time program OT1_jgoicoec_4 (PI J. Goicoechea), and the SPIRE scan map is from GT2_pandre_5 (PI: P. André).

scales. The *doGridding* routine in HIPE uses a Gaussian (for OTF maps) or box (for raster maps) filter function for spatially weighting signal readouts during scanning, according to the astrometric assignments to each spectrum, and frequency-dependent beam shapes that are approximated as two-dimensional Gaussian profiles for this purpose. The gridding and convolution technique is very similar to that used in the GILDASS/CLASS¹⁴ at most ground-based submillimeter telescopes.¹⁵ The final spectral cubes yield excellent signal-to-noise ratios (S/Ns), well above 100 for the $\text{CH}^+ J = 1-0$ line and exceptionally high in the strong $^{12}\text{C}^+$ line, at the beam resolutions of $11''.2$ (1900 GHz), $12''.5$ (1670 GHz), $14''.3$ (1470 GHz), $25''.2$ (835 GHz), and $38''.5$ (537 GHz). It is important to note that source features with angular dimensions that are a fraction of the beam size can be detected when S/Ns are high, so that positional information with $1''-4''$ relative uncertainty can be measured from strong sources of compact emission. S/Ns are estimated to be around 10–20 for the much weaker $^{13}\text{C}^+$ fine-structure transitions. For fitting the weaker $\text{CH}^+ J = 2-1$ and CH line emission we follow the standard

detection criterion for the integrated line intensity, namely 3σ [K km s^{-1}] = $3 \times \sigma_{\text{rms}} \sqrt{2\Delta v_{\text{bin}} \Delta v_{\text{FWHM}}}$, where σ_{rms} is the rms noise of the line-free baseline, Δv_{bin} is the channel binning width in km s^{-1} , and Δv_{FWHM} is the full width at half maximum intensity of the spectral line fitted as a Gaussian profile.

3. OBSERVATIONAL RESULTS

3.1. Overview of Kinematic Features in Orion BN/KL

As part of the description of our observational results for the spectrally mapped region around Orion BN/KL, it is helpful to place this region in morphological context with its wider OMC 1 surroundings. Figure 1 (right) indicates where our “deep” maps have been constructed from multiple observations, especially for C^+ and $\text{CH}^+ J = 1-0$ (see Table 1), by the boxes overlaid on the composite SPIRE 850 GHz , $\text{CH}^+ J = 1-0$, and 1900 GHz continuum observations, over an area of $7.5 \times 10'$ on a normalized intensity scale. All of these components were observed at similar angular resolutions, $\approx 12''-25''$ (half-power beam width, HPBW). The archival OMC 1 CH^+ map from the *Herschel* program OT1_jgoicoec_4 was observed at lower sensitivity, using a lower total integration time in a single observation (5.5 s per map point)

¹⁴ See www.iram.fr/IRAMFR/GILDAS/.

¹⁵ A detailed description is at herschel.esac.esa.int/hcss-doc-14.0/load/hifi_um/html/hdrg_dogridding_detail.html.

Table 1
Summary of HIFI Observations

Obs. ID	Obs. Mode ^a	Map Area	Sampling ^b	Obs. Date	Program ^c	Obs. Time (s)	LO freq. ^{d,e} (GHz)	η_{mb} ^f
1342190786	2	1/2 × 1/1	H	2010 Feb 18	C	6637	1896.9	0.60
1342190787	1	2/2 × 2/3	H	2010 Feb 18	C	17287	1896.9	0.60
1342192562	5	2010 Mar 22	H	13336	1578–1698	0.57
1342203225	1	2/1 × 2/4	H	2010 Aug 19	C	1382	841.2	0.63
1342203226	1	2/1 × 2/4	H	2010 Aug 19	C	1051	841.2	0.63
1342203240	3 ^g	1/1 × 1/2	N	2010 Aug 20	C	8210	1897.4	0.60
1342203241	2	1/1 × 1/2	N	2010 Aug 20	C	2680	1897.4	0.60
1342203242 ^h	1	1/1 × 1/2	N	2010 Aug 20	C	8935	1897.4	0.60
1342203731	1	3/4 × 4/1	H	2010 Aug 30	H	1114	543.0	0.61
1342203926	6	2010 Sep 01	C	2152	1474.1	0.57
1342203949	4	2/5 × 2/5	H	2010 Sep 02	H	27069	1666.2	0.57
1342205541	4	1/8 × 1/9	N	2010 Oct 02	H	1838.3	28003	0.60
1342227557	1	1/7 × 1/9	N	2011 Aug 27	C	551	1158.2	0.63
1342228593	1	2/3 × 2/7	N	2011 Sep 14	C	1543	841.2	0.63
1342229765 ^h	2	1/9 × 2/0	N	2011 Sep 16	C	4000	1897.4	0.60
1342239586	1	2/5 × 3/2	N	2012 Feb 23	C	1788	841.2	0.63
1342239623	2	2/0 × 3/0	N	2012 Feb 24	C	5488	1897.4	0.60
1342251025	1	2/5 × 3/2	N	2012 Sep 13	C	1788	841.2	0.63
1342251084	2	2/0 × 3/0	N	2012 Sep 17	C	5488	1897.4	0.60
1342266602	2	2/7 × 1/9	N	2013 Feb 28	C	5488	1897.4	0.60
1342266892	1	2/8 × 2/3	N	2013 Mar 09	C	1788	841.2	0.63

Notes.

^a Observing modes: (1) OTF map; (2) OTF map with load chop; (3) OTF map with frequency switch; (4) fast DBS raster map; (5) spectral scan with fast DBS; (6) point DBS.

^b Sampling: N = Nyquist; H = half-beam.

^c Program: C = HIFI calibration; H = HEXOS.

^d LO frequency is the setting requested in HSpot.

^e Noise requirements over a line-free 1 GHz wide WBS subband for both H and V polarizations combined: 300–500 mK at 1897 GHz; 100 mK at 841 GHz; 300 mK at 1666 GHz; 60 mK at 1841 GHz.

^f η_{mb} are the HIFI main-beam efficiencies, taken from calibrations with HIPE 14.0

^g Processed but excluded from this study; see text.

^h Maps are oriented with a rotation angle of 90°.

and uses half-beam rather than Nyquist sampling, but the S/N ≈ 50 mK per beam at maximum WBS resolution (1.1 MHz) is clearly sufficient to show the widespread spatial distribution of line emission. Overall the intensity distribution of CH⁺ is very similar to that of C⁺ mapped over the same area by Goicoechea et al. (2015a, 2015b).

In comparison to the SPIRE 850 GHz map, which is dominated by CO and thermal dust emission, the relative distribution of C⁺ is characteristic of a stratification of neutral and photoionized gas around the ionizing Trapezium stars. The 1900 GHz continuum is strongest toward the dense Hot Core, and secondarily in Orion South. The neutral/ionized stratification has been observed via comparison of integrated emission from H recombination, CO $J = 2-1$, and C⁺ (similarly mapped in OMC 1 with HIFI but at lower sensitivities) by Goicoechea et al. (2015b).

The region immediately around the dense Hot Core contains several physical features that give rise to spatially and kinematically distinct molecular line emission. The main features described in Crockett et al. (2014a) are summarized here and shown schematically in Figure 2. The main velocity components are identified with different colors, showing the locations of the BN object, IRc 2, and the directional relation to the massive and luminous OB stars of the Trapezium. Also shown is the submillimeter source SMA 1, where vibrationally excited transitions of CH₃OH, HC₃N, and SO₂ have been detected (Beuther et al. 2004) and interpreted to indicate the

presence of an embedded protostar. Close to SMA 1 and IRc 2 is the radio “source I” (not labeled, $\approx 0''.5$ to the south), which is an embedded protostar with no detectable submillimeter or IR emission (Menten & Reid 1995; Plambeck et al. 2009) and is thought to be driving the so-called “low velocity flow” (LVF) of molecular gas, detected by Genzel & Stutzki (1989), in a NE–SW direction; see also Crockett et al. (2014a) and references therein. A distinct and more extended “high velocity flow” in the NW–SE direction may be driven by another embedded protostar associated with SMA 1, and gives rise to the well-known butterfly-shaped bipolar outflow traced by vibrationally excited H₂ (e.g., Bally et al. 2011 and references therein) and other species tracing shocked gas. The H₂ outflow is important to the discussion of the dominant CH⁺ formation mechanism over our mapped region (Section 4). Both flows constitute part of a molecular “plateau” characterized by broad lines ($\Delta v \gtrsim 20$ km s⁻¹) and $v_{LSR} \approx 7-11$ km s⁻¹. To the southwest of the Hot Core region is the so-called “Compact Ridge,” a group of quiescent gas clumps containing complex oxygen-bearing organics, with emission lines typically at velocities $v_{LSR} \approx 7-9$ km s⁻¹ and widths $\Delta v = 3-6$ km s⁻¹ (Blake et al. 1987; Beuther et al. 2005; Friedel & Snyder 2008; Crockett et al. 2014a).

The Hot Core itself has been so named because of the hot ($T_{kin} \geq 150$ K) and dense ($\gtrsim 10^7$ cm⁻³) material hosting massive protostars, although whether one or more protostars is the source of heating as opposed to an external source is a

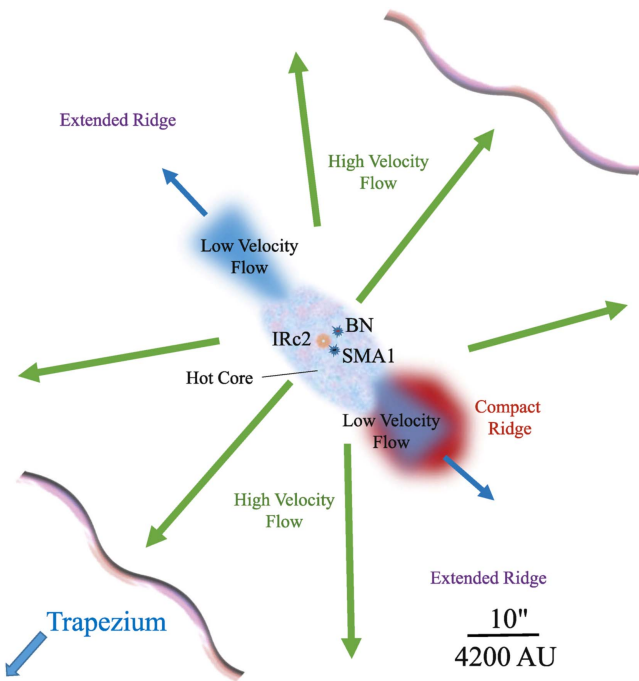


Figure 2. Schematic representation of principal kinematic features in the vicinity of the Orion Hot Core, based on Figure 7 in Crockett et al. (2014a), representing approximate coverage of the mapping in the study drawn on the plane of the sky. Each distinct velocity component is labeled in a different color, and they are summarized in Section 3.1. The angular scale in AU assumes a distance of 420 pc.

matter of debate in the literature (see de Vicente et al. 2002; Goddi et al. 2011; Zapata et al. 2011). Line widths are typically $\Delta v \approx 7\text{--}11 \text{ km s}^{-1}$ at $v_{\text{LSR}} \approx 4\text{--}6 \text{ km s}^{-1}$.

3.2. Properties of the C^+ Gas

Emission from $^{12}C^+$ is strong, with up to six velocity peaks that can be resolved with a confidence of detection $>5\sigma$ across the region, tracing a complex photodissociated cloud structure. The distribution of integrated line intensities is shown in Figure 3, covering the range of LSR velocities -10 to $+15 \text{ km s}^{-1}$ (avoiding minor contributions from $^{13}C^+$ $F = 2 - 1$ emission). The integrated emission shows maximum intensity $I(^{12}C^+) \approx 1160 \text{ K km s}^{-1}$ at $0'.5$ SW of θ^1 Ori C (labeled as Peak B in Figure 3), in part of a loosely projected ring of gas $\sim 1'.4$ south of IRC 2. While there are numerous nearby young stellar objects and OB-type stars, the emission structure does not correlate with any particular stellar (e.g., the Trapezium) or protostellar source, nor is there any particular source near the projected center of the southern emission ring. Secondary peaks of C^+ emission occur just to the NE of IRC 2, labeled A and A', where the latter coincides more closely with the CH^+ peak nearest to the Hot Core, as will be shown in Section 3.4. By contrast, the integrated emission toward the Hot Core is nearly a factor of ~ 4 lower, possibly from line-of-sight absorption of the strong continuum, which we shall address further below in this section.

Figure 4 shows spectra extracted at the labeled locations of strongest emission, and an overall average that excludes a region of $25''$ diameter centered on IRC 2, illustrating the range of profiles. Each spectrum is plotted on the scale of antenna temperature T_A , and has been extracted in synthetic circular apertures of width $11''.2$ corresponding to the HPBW of HIFI at

1900 GHz. In these and other figures showing local spectral extractions, we have employed a method of fitting Gaussian profiles that minimizes the residual spectrum in order to efficiently identify and characterize LSR velocities and line widths. In reality, gas turbulence and moderate changes in optical depth (which are explored below) will cause departures from a Gaussian profile shape. The residuals shown in Figures 4 and 5 show the levels where the approximations fail, typically at the 2%–4% level of peak intensity near line center. The residuals are non-Gaussian (and thus cannot be minimized further with an arbitrary increase in the number of Gaussian fit components), and widths of the residual features are $\approx 1\text{--}2 \text{ km s}^{-1}$.

The dominant C^+ feature can be fitted by two Gaussian components with a principal component at $\langle v_{1,\text{LSR}} \rangle = 9.3 \text{ km s}^{-1}$ and a weaker secondary component at $\langle v_{2,\text{LSR}} \rangle = 8.3 \text{ km s}^{-1}$, with line widths (FWHM) $\langle \Delta v \rangle$ of 4.6 and 2.4 km s^{-1} , respectively. The strongest emission from other locations can be similarly decomposed into two components, varying in LSR velocity of the primary component between 8.6 and 11.0 km s^{-1} . Emission at these velocities is strongest in the plateau to the NE of the Hot Core and south of the Trapezium stars, as seen in the velocity channel maps in Figure 6. The dominant velocities and dispersions are consistent on average with early $^{12}C^+$ observations of Orion A with $3'$ resolution by Balick et al. (1974), who suggested a dynamically distinct and quiescent cloud interface between Orion KL and the Trapezium stars, compared to the H II emitting region.

The spectrum centered on the Hot Core source SMA 1 is shown in Figure 5 on a wider velocity scale to show the spectral complexity along this sightline. In this spectrum we find evidence of C^+ line absorption near 5.5 km s^{-1} ; this will be treated in the next subsection. The $^{13}C^+$ triplet is also detected everywhere in our mapped region, although this is sometimes limited to the $F = 2\text{--}1$ transition, which is expected from the partition function to be strongest (see Section 3.3.1).

Very similar characteristics have been reported in HIFI observations of OH^+ and H_2O^+ absorption (Gupta et al. 2010) and HF P-Cygni profiles (Phillips et al. 2010) toward Orion BN/KL, and in these lines plus CH^+ absorption toward OMC-2 FIR4 roughly $13'$ to the NNE of the BN object (López-Sepulcre et al. 2013). While there is a considerable amount of spatial and kinematic variation of the C^+ emission in our HIFI map of 12 arcmin^2 around BN/KL (note the complexity of the profiles particularly at Position A and toward the Hot Core in Figure 4, and the spatial variations in Figure 6), the general kinematic similarities with CH^+ toward OMC-2 FIR4 add support for the conclusion by López-Sepulcre et al. (2013) that the cloud observed further to the north is an extension of the C^+ interface between Orion KL and the Trapezium, and thus interpreted to be part of the larger parent cloud of OMC 1. At the higher resolution of our observations around BN/KL (HPBW $\approx 11''$), the C^+ gas exhibits a high level of velocity variation among multiple components.

3.3. C^+ Absorption

The Hot Core spectrum (Figure 5) can be decomposed into a predominant and relatively narrow emission component at $+8.7 \text{ km s}^{-1}$ and two weaker flows at $+5.8$ and -7.4 km s^{-1} . This compares with $v_{\text{LSR}} = 3\text{--}5 \text{ km s}^{-1}$ of molecular emission from the Hot Core (Blake et al. 1987), indicating that most of

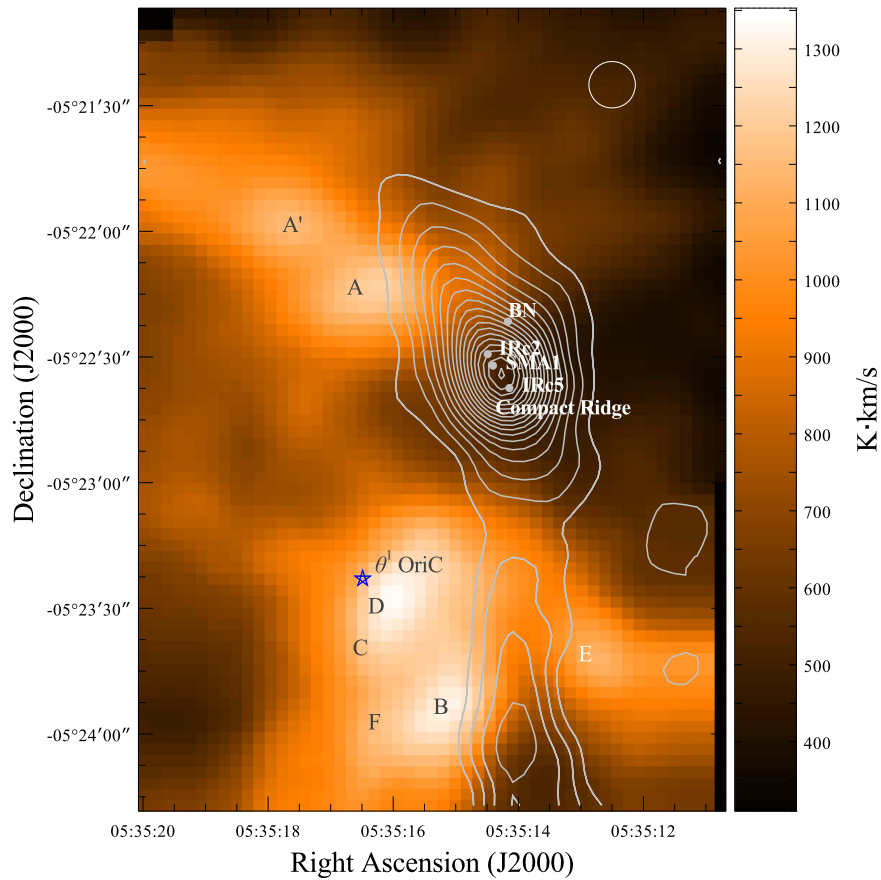


Figure 3. C^+ emission integrated on a main-beam temperature scale over -10 to $+15$ km s^{-1} , and the continuum at 1900 GHz shown in white contours on a linear scale between 0.5 and 35 K at intervals of 1.0 K. The $1\sigma_{\text{rms}}$ noise level is 0.1 K km s^{-1} per beam. The HIFI beam size at 1900.5 GHz is $11''.2$ (HPBW), represented in the upper right. Locations of peak emission are labeled for reference to spectral extractions presented in Figure 4.

the detected C^+ emission is emitted from outside this warm and dense region. The profile fit includes narrow ($\Delta v = 1.3$ km s^{-1}) absorption against the continuum at $v_{\text{LSR}} = +5.5$ km s^{-1} , with an optical depth of 1.0–1.3 at line center. Absorption is expected when a significant column of low-density gas is observed toward a strong source of background emission at temperature T_{bg} , and the excitation temperature T_{ex} is less than the brightness temperature of the background; i.e.,

$$T_{\text{ex}}(C^+) < \frac{91.2}{\ln(1 + 91.2/T_c(1900.5))} \simeq 25.0 \text{ K} \quad (1)$$

where the continuum brightness temperature at 1900.5 GHz is $T_c(\text{K}) = 91.2/(e^{91.2/T_{\text{bg}}} - 1)$. The value 91.2 K is the equivalent temperature $T_* \equiv h\nu/k$ at 1900.5 GHz. At the position of SMA 1 where we observe the absorption, the continuum temperature peaks at around 25.0 K, and if we add 2.7 K for the cosmic microwave background temperature (thus $T_{\text{bg}} = 27.7$ K), then $T_c \simeq 3.5$ K and $T_{\text{ex}} \lesssim 28$ K for the absorption component. Goicoechea et al. (2015b) suggest that absorption may be indicated in C^+ profiles for some sightlines in Orion’s extended Veil region (a collection of absorbing H I layers with low H_2 densities) and predict the ranges of T_{ex} and H I densities where absorption by C^+ should occur. Here we can at least confirm detection of C^+ absorption toward the Hot Core where τ is around unity. At other positions in our map we cannot be as certain, because all profiles can be well

represented by emission only. We should note that the kinematics reported here are consistent with those by Goicoechea et al. (2015b) using HIFI observations of the larger OMC 1 region, but there are differences in line profiles and peak intensities, highlighted by the BN/KL spectrum, for example. The spectrum shown in their Figure 3 lacks both the structure of the main C^+ emission components over -20 to $+30$ km s^{-1} and significant emission of molecular lines near ± 50 km s^{-1} relative to the main C^+ line. This is probably a result of differences in sensitivities in the two sets of observations, as noted above.

Velocity channel maps are shown in Figure 6. Each channel is an integration of ± 0.25 km s^{-1} around the labeled velocity. The structure is striking at velocities where emission peaks are spectrally resolved, owing to the high data quality of the baselines (particularly, good corrections for the optical and ESWs, as described in Section 2). At $v_{\text{LSR}} = -12.5$ and -3.5 km s^{-1} , for example, the spectrally resolved emission can be measured to better than 5σ detection in “velocity clumps” (loosely speaking), which are spatially resolvable to as small as $11''.0$ – $11''.5$ FWHM in a representative profile tracing (see Figure 7), i.e., comparable to the $11''.2$ HPBW of HIFI at these frequencies. These sizes correspond to ≈ 0.02 pc (4.8×10^3 AU) at a distance of 420 pc to Orion BN/KL (Hirota et al. 2007). The C^+ structures are relatively smoothly distributed and do not appear to follow any particular correlation in distribution or intensity with the embedded

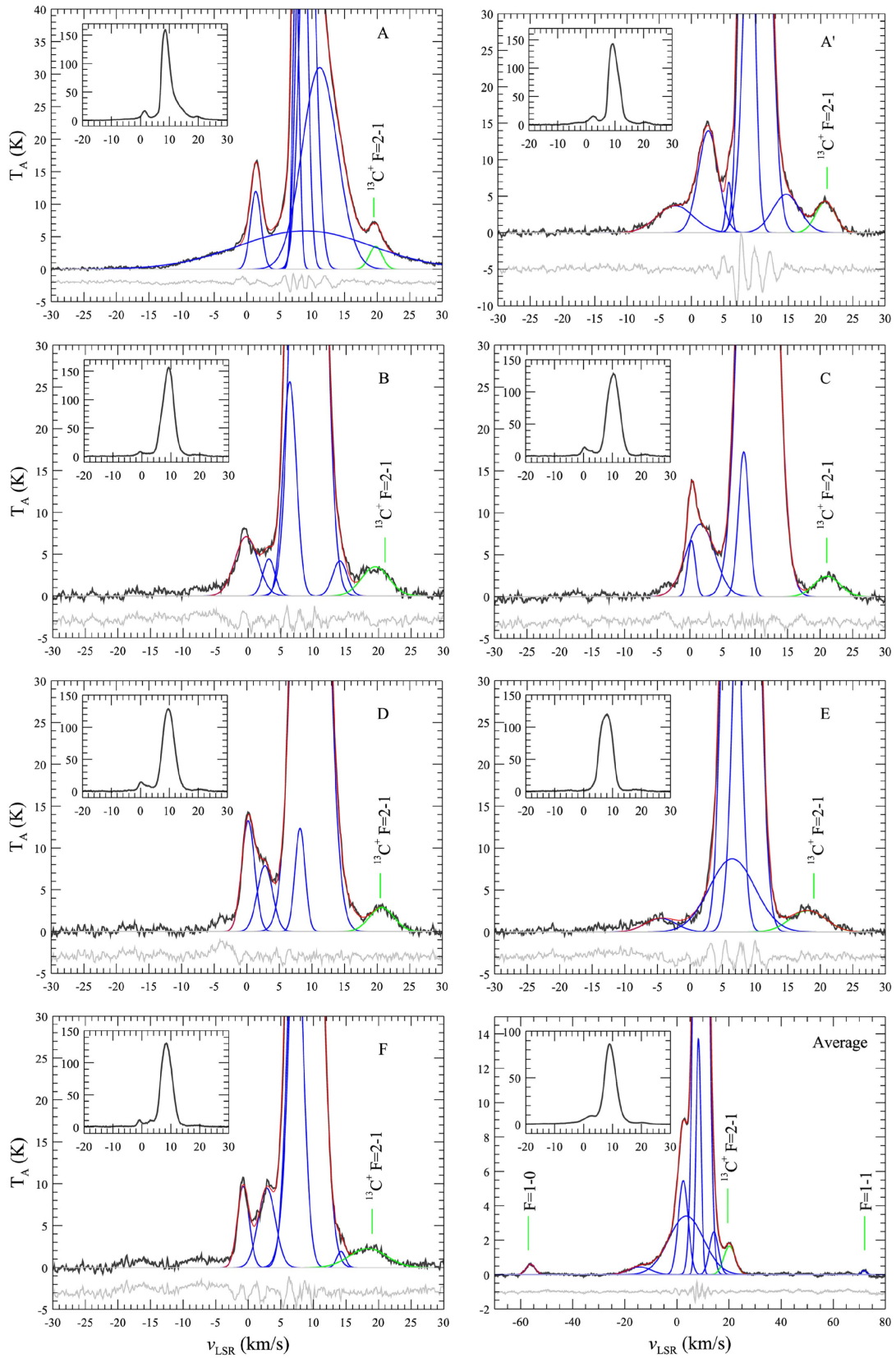


Figure 4. HIFI spectra of $\text{C}^+ 2P_{3/2,1/2}$ as an average and at positions marked in Figure 3, extracted using a circular aperture of width $11''/2$ corresponding to the HPBW at 1900 GHz. The spectrum labeled Average (bottom right) excludes the inner $15''$ centered on BN/KL, which is shown in Figure 5. Observed spectra (black) are fitted with Gaussian profiles (blue) using χ^2 minimization of the residual differences between the total model (red) and the observations. Only the number of profiles is constrained; intensities and widths are free parameters during the minimization. The residuals (gray) near the bottom of each panel are offset for clarity. Integrated fluxes of the two strongest components are given in Table 3.

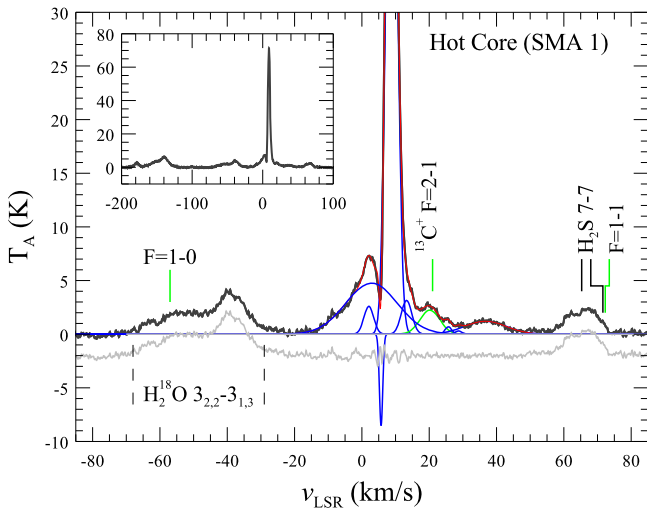


Figure 5. HIFI spectrum of C^+ in the Hot Core region using a circular extraction aperture of width $15''$ centered on the position of SMA 1 indicated in Figure 3. Observed spectra (black) are fitted with Gaussian profiles (blue) using χ^2 minimization of the residual differences between the total model (red) and the observations. The residuals (gray) near the bottom of each panel are offset for clarity. Integrated fluxes of the two strongest components are given in Table 3.

sources in the core region or with the hot UV source θ^1 Ori C, which is located some 0.3 pc in front of OMC 1 (Bally 2008, p. 459).

The most blueshifted emission from C^+ occurs at $v_{\text{LSR}} = -12.5 \text{ km s}^{-1}$, as shown in the upper left plot of Figure 6, and is concentrated very close (in projection) to the BN object with a clumpy appearance. The intensities at this velocity are at the detection limit of these observations. More blueshifted emission from velocity channels at the spatial resolution of these maps cannot be discerned to better than $2\sigma_{\text{rms}}$. Detection of C^+ at velocities $< -10 \text{ km s}^{-1}$ is an interesting question for its possible relation to the H I absorbing cloud observed in the south near the Orion Bar in the range -20 to -10 km s^{-1} by van der Werf et al. (2013), i.e., as part of the neutral atomic layers characterizing the Orion Veil, as discussed by Goicoechea et al. (2015b). A portion of this blueshifted C^+ emission should arise in the ionized region between the Veil and the Trapezium. Spectral extractions around θ^1 Ori C and at random locations throughout our mapped region do not reveal emission in that range of blueshifted velocities. By comparison, the redshifted velocities of peak C^+ emission, $\approx 14.5 \text{ km s}^{-1}$, are similar to those of S III and P III absorptions observed in the UV by Abel et al. (2006). The C^+ at this redshifted velocity is part of a more generally distributed ionized cloud around BN/KL, not concentrated in way that can be associated with a foreground H II region between the low-density H I Veil and Trapezium stars as suggested by Goicoechea et al. As we noted in the description of the data processing (Section 2), no C^+ contamination is present in the reference sky positions that might “hide” emission (by accidental subtraction) from the Veil in our observations.

The structure of the kinematically distributed gas, isolating the low-intensity emission at velocities away from the peak emission, is shown in Figure 8, composed of -8.25 km s^{-1} (blue), -3.5 km s^{-1} (green), and $+4.0 \text{ km s}^{-1}$

(red) channels, each normalized to peak intensity. The granular nature of the expanding and receding emission sources occurs at scale sizes similar to that measured from Figure 7, and possibly traces local enhancements in the electron density n_e . Weilbacher et al. (2015) have recently estimated electron temperatures and densities over a region of $\sim 6' \times 5'$ that covers our observed area, using high-quality spectroscopic observations of [N II] and [S III] (for electron temperature) and [S II] and [Cl III] (for electron density) doublets obtained with the MUSE optical integral-field spectrograph at the ESO Very Large Telescope. The values of n_e based on the [S II] $\lambda 6731/\lambda 6716$ ratio range from ~ 500 to 10^4 cm^{-3} , while n_e based on the [Cl III] $\lambda 5538/\lambda 5518$ is much higher, ranging between 4000 and $2.5 \times 10^4 \text{ cm}^{-3}$ (but is numerically noisier; see Weilbacher et al. 2015). Both are broadly consistent in their spatial distribution, but neither exhibits a clumped morphology that correlates very well with our C^+ observations. The MUSE observations were sampled at $0''.2$ angular resolution, and applying a Gaussian filter to smooth the MUSE n_e maps to the approximate beam width of our HIFI data does not reveal a morphology on any spatial scale that resembles the C^+ emission at any velocity shown in Figure 6, in a combination of channels as shown in Figure 8, or integrated across the full range of C^+ velocities as in Figure 3. On the other hand, the distribution of the main C^+ emission component near $v_{\text{LSR}} \simeq +9.0 \text{ km s}^{-1}$ does broadly follow changes in excitation temperature and optical depth, which are discussed in Section 3.3.2.

At velocities outside the range shown in Figure 4 we do not detect any higher velocity (i.e., $|v_{\text{LSR}}| > 20 \text{ km s}^{-1}$) emission from C^+ . The emission features at -38.9 and $+65.6 \text{ km s}^{-1}$ in the Hot Core spectrum (Figure 5), which are relatively symmetric around the main emission component at 8.7 km s^{-1} , are at first suggestive of velocities in molecular lines such as HF $J = 1-0$ and $\text{H}_2\text{O}^+ J = 3/2-1/2$ absorptions, or in the wings of broad CO $J = 1-0$ emission that have been associated with the LVF (e.g., Zuckerman et al. 1976; Schulz et al. 1995; Wilson et al. 2001; Gupta et al. 2010; Phillips et al. 2010; Zapata et al. 2010; Peng et al. 2012a). However, careful inspection shows that the blueshifted feature can be attributed to H_2^{18}O while the redshifted feature is dominated by H_2S , which have both been modeled by Crockett et al. (2014b). The modeled profiles tend to underestimate the strengths observed here, which is possibly a result of uncertainties in the size of the emitting source, but they are sufficient to rule out any obvious contribution from C^+ at velocities that are typical of the molecular LVF.

3.3.1. Hyperfine $^{13}\text{C}^+ 2P_{3/2}-2P_{1/2}$

In the same range of velocities of $^{12}\text{C}^+$ we also detect the three hyperfine transitions of $^{13}\text{C}^+$, $F = 1-1$, $2-1$, and $1-0$, as shown in the average spectrum in Figure 4. The $F = 1-1$ and $1-0$ transitions do not meet our detection criterion everywhere over our mapped region, nor at every selected position above 3σ of the baseline noise, but the $F = 2-1$ line is detected everywhere and is sufficiently resolved (spectrally) from the main $^{12}\text{C}^+$ emission that we can interactively fit the individual components to provide estimates of the $^{13}\text{C}^+$ contribution at these positions. It is not possible to construct a reliable map of $F = 2-1$ integrated intensity by profile decomposition over the entire region due to the very large

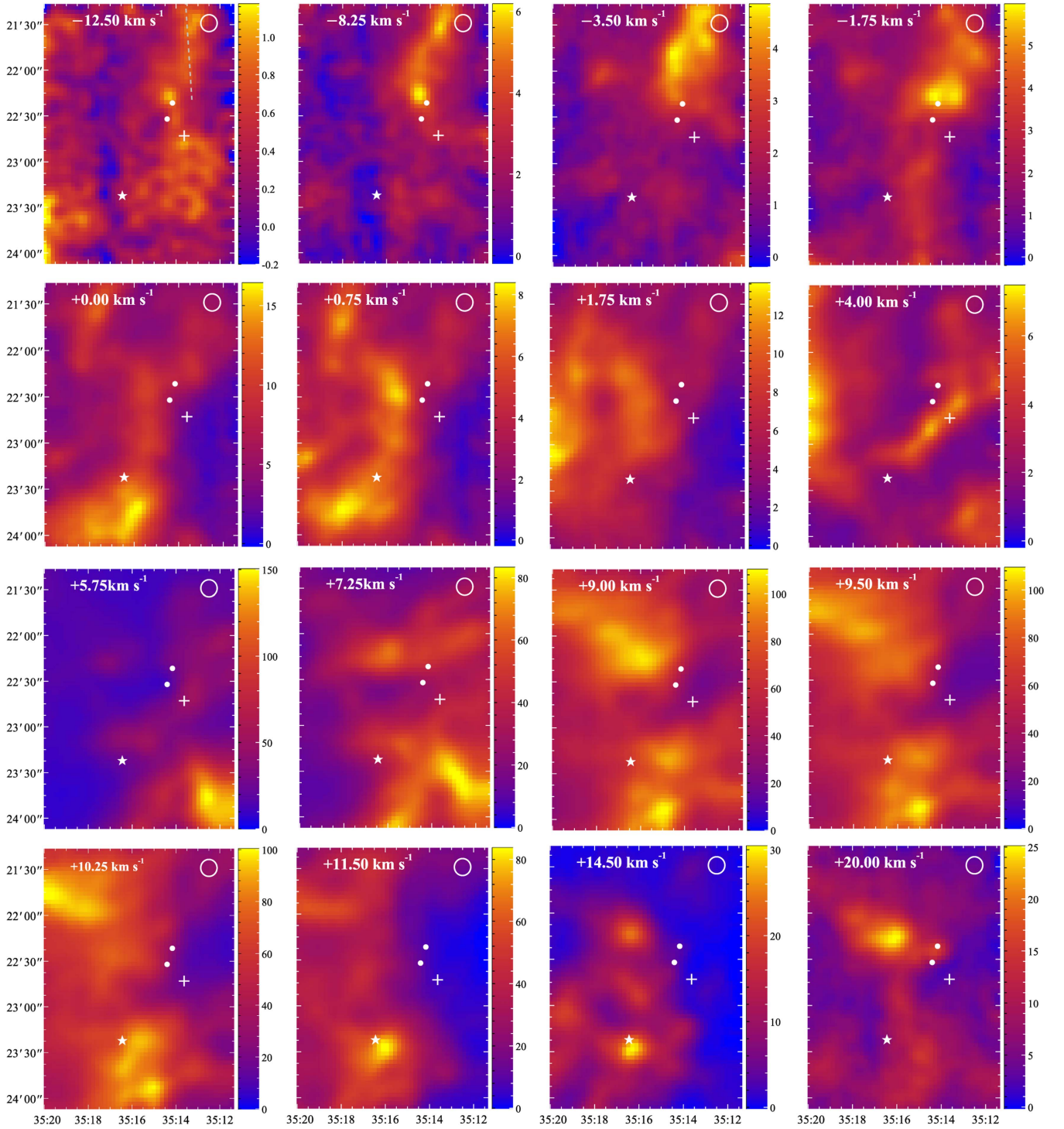


Figure 6. Velocity channels of $^{12}\text{C}^+$. Each channel map is an integration over $\pm 0.5 \text{ km s}^{-1}$ around the labeled velocity, on a linear intensity scale of K km s^{-1} . Coordinates on horizontal and vertical axes are referenced to R.A. $5^{\text{h}}00^{\text{m}}00^{\text{s}}$ and decl. $-5^{\circ}00'00''$ (J2000.0), respectively. The HIFI $11''/4$ beam size is indicated in all plots, and the location of the cut for the intensity profile in Figure 7 is shown in the -12.5 km s^{-1} channel map. The $+20.0 \text{ km s}^{-1}$ channel in the panel in the bottom right corner corresponds to the $^{13}\text{C}^+$ $F = 2-1$ fine-structure line at $v_{\text{LSR}} = +8.4 \text{ km s}^{-1}$. The filled white circles indicate the locations of the BN (northern) and SMA 1 (southern) sources. The cross and filled star indicate the locations of the Compact Ridge and θ^1 Ori C, respectively.

variations in the number of $^{12}\text{C}^+$ components, LSR velocities, intensities, and widths (as can be seen from Figure 6), restricting reliable fits to the representative positions given in Table 3.

The $+19.5 \text{ km s}^{-1}$ velocity channel shown in the bottom right panel of Figure 6 shows peak emission of the $F = 2-1$ transition corresponding to $v_{\text{LSR}} = +8.4 \text{ km s}^{-1}$ coincident

with Peak A of $^{12}\text{C}^+$. At that position, the v_{LSR} and width of $^{13}\text{C}^+$ are consistent with those of the dominant $+8.6 \text{ km s}^{-1}$ component of $^{12}\text{C}^+$. The fact that $^{13}\text{C}^+$ does not reach peak intensity at the same locations B and D as $^{12}\text{C}^+$ could be due to variations in isotopic abundance, but is more likely due to differences in optical depth of $^{12}\text{C}^+$, discussed next.

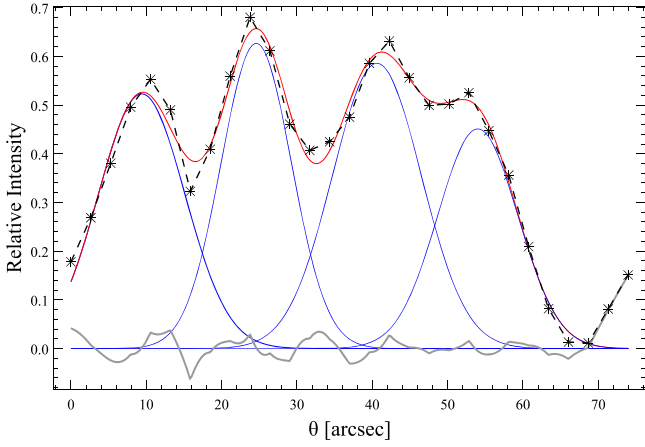


Figure 7. Spatial profile of C^+ emission traced along a cut in the -12.5 km s^{-1} channel map as indicated in Figure 6 in the same units. The trace is fitted by Gaussian profiles with FWHM between $11''.0$ and $14''.4$ with the residual shown in gray.

3.3.2. The C^+ Optical Depth, Excitation Temperature, and Column Density

A determination of the C^+ gas column densities depends on line opacities and excitation temperatures through the equation (e.g., Ossenkopf et al. 2013)

$$\begin{aligned} N(^{12}C^+) &= 1.40 \times 10^{17} \frac{1 + 2 \exp(-91.2/T_{\text{ex}})}{1 - \exp(-91.2/T_{\text{ex}})} \int \tau d\nu \\ &\simeq 1.49 \times 10^{17} \frac{1 + 2 \exp(-91.2/T_{\text{ex}})}{1 - \exp(-91.2/T_{\text{ex}})} \Delta\nu \times \tau_{12} \text{ (cm}^{-2}\text{)} \end{aligned} \quad (2)$$

where τ_{12} is the $^{12}C^+$ optical depth at line center and $\Delta\nu$ is the FWHM Gaussian line width in km s^{-1} . In order to estimate τ_{12} , we recognize that the $^{12}C^+/^{13}C^+$ integrated intensity ratio reflects the $^{12}C/^{13}C$ abundance ratio of the gas, provided that the $^{13}C^+$ emission can be treated as optically thin. Following Boreiko & Betz (1996), the total isotopic abundance ratio $R \equiv ^{12}C/^{13}C$ is related to the ionic line intensity ratio I_{13}/I_{12} and τ_{12} by

$$R = \frac{-\tau_{12}}{\ln\left[1 - \frac{I_{13}}{I_{12}}(1 - e^{-\tau_{12}})\right]}. \quad (3)$$

There is no dependence on the excitation temperature, but it is implicitly assumed that both isotopes are emitting from the same gas. The total integrated intensities are tabulated in Table 3 at the positions indicated in Figure 3. The $^{13}C^+$ intensities have been obtained by summing over all three measured hyperfine components following our detection criterion (Section 3) or otherwise by measurement of the strongest $F = 2-1$ component and applying the theoretical 0.25:0.125:0.625 partitioning of $F = 1-0:1-1:2-1$, when either or both of the two weaker components are below the detection limit. We find that this partitioning holds up very well where we can measure all three components, as can be seen in Table 3, where we give the I_{13} integrated sum using both

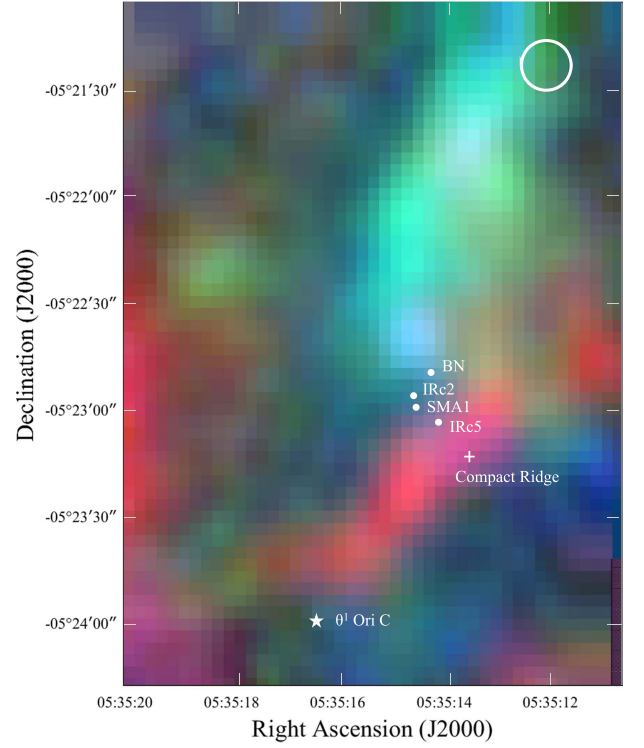


Figure 8. Distribution of the quiescent C^+ emission from -8.25 km s^{-1} (blue), -3.5 km s^{-1} (green), and $+4.0 \text{ km s}^{-1}$ (red) channels, each normalized to its own peak integrated intensity.

methods, thus supporting the assumption of a low $^{13}C^+$ optical depth.

If $^{12}C^+$ line emission is also treated as optically thin, then R matches the tabulated values of I_{12}/I_{13} . However, these would yield abundance ratios that are a factor of 2–3 lower than the total ratio of 67 based on local $^{12}C^{18}O$ and $^{13}C^{18}O$ observations in Orion by Langer & Penzias (1990, 1993). Boreiko & Betz (1996) derived $\tau_{12} = 1.2$ toward θ^1 Ori C, based on a kinetic temperature $T_{\text{kin}} = 185 \pm 15 \text{ K}$ calculated from O I and C II observations along that sightline. If we set $\tau_{12} = 1.2$ as an average over our mapped region around KL, then we obtain an abundance ratio $R = 53$ for the diffuse medium outside the Hot Core. This is very close to the value of 57 given by the relationship of $^{12}C/^{13}C$ with Galactocentric radius obtained by Langer & Penzias (1990), and the value 58_{-5}^{+6} for θ^1 Ori C by Boreiko & Betz (1996) based on their measured ionic intensity ratio and independently derived value of τ_{12} .

This demonstrates that our result for the average isotopic abundance ratio based on a fixed value of τ_{12} is consistent with previous results along the specific sightline of θ^1 Ori C, and also according to the $^{12}C/^{13}C$ ratio with Galactocentric radius. We could assume that the isotopic abundance ratio R is constant within the mapped region, and take all variations of the intensity ratio to reflect changes in the column density. Thus we can switch to exploring the spatial variations in the $^{12}C^+$ optical depth more quantitatively at a fixed value of R . For R we adopt a value of 67_{-5}^{+6} . This is high (but within the uncertainty) compared to the value calculated by Boreiko & Betz (1996), which we used as a consistency check with the value of τ_{12} they derived toward θ^1 Ori C. Here we adopt the estimate by Langer & Penzias (1993) since we are re-deriving

Table 2
Physical Parameters of the Transitions Observed with HIFI in This Study

Species	Transition	Rest Freq. (GHz)	References ^a	E_{up} (K)	$\log_{10}(A_{ij})$ (s^{-1})	BN/KL Line Crowding ^b
$^{12}\text{C}^+$	$^2P_{3/2}-^2P_{1/2}$	1900.5369	C, 1	91.2	-5.64	
$^{13}\text{C}^+$	$^2P_{3/2}-^2P_{1/2} F = 1-1$	1900.1360	C, 1, 2	91.2	-6.11	$\text{H}_2\text{S } 7_{1,6}-7_{0,7} \text{ 1900.14, } 7_{2,6}-7_{1,7} \text{ 1900.18 GHz}$
	$^2P_{3/2}-^2P_{1/2} F = 2-1$	1900.4661	C, 1, 2	91.2	-5.63	$^{12}\text{C}^+ \text{ 1900.5369 GHz}$
	$^2P_{3/2}-^2P_{1/2} F = 1-0$	1900.9500	C, 1, 2	91.2	-5.81	$\text{H}_2^{18}\text{O } 3_{2,2}-3_{1,3} \text{ 1894.32 GHz}$
$^{12}\text{CH}^+$	$J = 1-0$	835.1369	C, 3, 4	40.1	-2.20	
	$J = 2-1$	1669.2810	C, 4	120.2	-1.21	
^{12}CH	$^2\Pi_{3/2}-^2\Pi_{1/2} F = 2^- - 1^+$	536.76266	J, 5, 6	25.8	-3.20	
	$^2\Pi_{3/2}-^2\Pi_{1/2} F = 1^- - 1^+$	536.78354	J, 5, 6	25.8	-3.67	
	$^2\Pi_{3/2}-^2\Pi_{1/2} F = 1^- - 0^+$	536.79729	J, 5, 6	25.8	-3.38	$\text{SO}_2 10_{4,6}-9_{3,7} \text{ 549.30 GHz}$
	$^2\Pi_{3/2}-^2\Pi_{3/2} F = 1^+ - 2^-$	1470.68940	C, 5, 6	96.3	-3.05326	
	$^2\Pi_{3/2}-^2\Pi_{3/2} F = 1^+ - 1^-$	1470.69169	C, 5, 6	96.3	-2.35435	
	$^2\Pi_{3/2}-^2\Pi_{3/2} F = 2^+ - 2^-$	1470.73960	C, 5, 6	96.3	-2.32069	
	$^2\Pi_{3/2}-^2\Pi_{3/2} F = 2^+ - 1^-$	1470.74189	C, 5, 6	96.3	-3.27559	
	$^2\Pi_{3/2}-^2\Pi_{3/2} F = 1^+ - 1^-$	1477.29211	C, 5, 6	96.7	-2.35264	
	$^2\Pi_{3/2}-^2\Pi_{3/2} F = 1^+ - 2^-$	1477.31293	C, 5, 6	96.7	-3.05513	
	$^2\Pi_{3/2}-^2\Pi_{3/2} F = 2^+ - 1^-$	1477.36552	C, 5, 6	96.7	-3.27726	
	$^2\Pi_{3/2}-^2\Pi_{3/2} F = 2^+ - 2^-$	1477.38634	C, 5, 6	96.7	-2.32266	
	$^2\Pi_{5/2}-^2\Pi_{3/2} F = 3^+ - 2^-$	1656.96136	C, 5, 6	105.2	-1.42954	
	$^2\Pi_{5/2}-^2\Pi_{3/2} F = 2^+ - 2^-$	1656.97065	C, 5, 6	105.2	-2.42971	
	$^2\Pi_{5/2}-^2\Pi_{3/2} F = 2^+ - 1^-$	1656.96136	C, 5, 6	105.2	-1.47521	
	$^2\Pi_{5/2}-^2\Pi_{3/2} F = 3^+ - 2^-$	1661.10745	C, 5, 6	105.5	-1.42587	$\text{H}_2\text{O } 2_{2,1}-2_{1,2} \text{ 1660.0 GHz}$
	$^2\Pi_{5/2}-^2\Pi_{3/2} F = 2^+ - 1^-$	1661.11822	C, 5, 6	105.5	-1.47163	$\text{H}_2\text{O } 2_{2,1}-2_{1,2} \text{ 1660.0 GHz}$
	$^2\Pi_{5/2}-^2\Pi_{3/2} F = 2^+ - 2^-$	1651.13903	C, 5, 6	105.5	-2.42603	$\text{H}_2\text{O } 2_{2,1}-2_{1,2} \text{ 1660.0 GHz}$
CH_3OH^c	$5_{5,1} \rightarrow 5_{4,1}$	835.00376	C, 7, 8	170.9	-2.99	
	$6_{5,2} \rightarrow 6_{4,2}$	834.95935	C, 7, 8	184.8	-2.80	
	$7_{5,3} \rightarrow 7_{4,3}$	834.90431	C, 7, 8	201.1	-2.71	
	$8_{5,4} \rightarrow 8_{4,4}$	834.83715	C, 7, 8	219.6	-2.66	
	$9_{5,5} \rightarrow 9_{4,5}$	834.75617	C, 7, 8	240.5	-2.62	
	$10_{5,6} \rightarrow 10_{4,6}$	834.65944	C, 7, 8	263.7	-2.60	
	$11_{5,7} \rightarrow 11_{4,7}$	834.54485	C, 7, 8	289.2	-2.59	
	$12_{5,8} \rightarrow 12_{4,8}$	834.41005	C, 7, 8	317.1	-2.58	
	$13_{5,9} \rightarrow 13_{4,9}$	834.25251	C, 7, 8	347.2	-2.57	
	$14_{5,10} \rightarrow 14_{4,10}$	834.06946	C, 7, 8	379.7	-2.56	$\text{SO}_2 15_6-14_5 \text{ 848.52 GHz}$
	$15_{5,11} \rightarrow 15_{4,11}$	833.85794	C, 7, 8	414.5	-2.56	
	$16_{5,12} \rightarrow 16_{4,12}$	833.61481	C, 7, 8	451.6	-2.56	$\text{HDO } 2_{1,2}-1_{1,1} \text{ 848.96 GHz}$

Notes.

^a References: (C) Cologne Database for Molecular Spectroscopy (Müller et al. 2005), (J) JPL Molecular Spectroscopy Database (Pickett et al. 1998), (1) Cooksy et al. (1986), (2) Ossenkopf et al. (2013), (3) Pearson & Drouin (2006), (4) Müller (2010), (5) Brown & Evenson (1983), (6) Davidson et al. (2001), (7) Xu & Lovas (1997), (8) Comito et al. (2005).

^b Notable line blending or crowding refers to the inner 15'' of the BN/KL complex centered on IRc 2. Species separated by more than 12 GHz from the rest frequencies of column 3 are from the image sideband.

^c CH_3OH transitions are of E-symmetry $K_5 \leftrightarrow 4 v_t = 0$.

τ_{12} based on our HIFI observations, and this value of R has been adopted by Ossenkopf et al. (2013) for the Orion Bar, with which we will compare our results. The assumptions that the $^{13}\text{C}^+$ emission is optically thin and that the excitation temperature is the same for $^{12}\text{C}^+$ and $^{13}\text{C}^+$ are included in the 15% uncertainty.

Our results for the $^{12}\text{C}^+$ optical depths, given in Table 3, show large variations around the average value, because the $^{12}\text{C}^+ / ^{13}\text{C}^+$ intensity ratio varies with position. Generally, the optical depth of the $^{12}\text{C}^+$ line ranges from 1.4 to 2.6 outside the Hot Core, and from 4.0 to 6.2 for the Hot Core sightline. The tabulated values are consistent overall with results by Goicoechea et al. (2015b) for the whole of OMC 1 at the same value of R (although they do not quote an estimate for the Hot Core region where we find very high values of τ_{12}), considering the differences in sensitivity of the observations.

Our estimates are based on measurements of the two strongest emission components of $^{12}\text{C}^+$ with v_{LSR} and widths similar to observed $^{13}\text{C}^+$ (and CH^+ and CH presented below). If we had restricted our estimates to the main emission component, as done by Goicoechea et al., our values of τ_{12} would increase by $\approx 20\%$ (on average). Conversely, if we include the full range of observed $^{12}\text{C}^+$ velocity components, -10 to $+15 \text{ km s}^{-1}$, the optical depths will decrease by about the same amount.

The variation of $^{12}\text{C}^+$ optical depths around Orion BN/KL is similar to that observed in the Orion Bar PDR (Ossenkopf et al. 2013). There, as in Orion BN/KL, the role of chemical fractionation of carbon driven by the reaction $^{13}\text{C}^+ + \text{CO} \rightleftharpoons ^{12}\text{C}^+ + ^{13}\text{CO} + 34.8 \text{ K}$ (Langer et al. 1984) is difficult to quantify due to the variation in optical depth of the main isotopologues. A significant fractionation into ^{13}CO would enhance the $^{12}\text{C}^+ / ^{13}\text{C}^+$ abundance ratio, yielding I_{12} / I_{13} that is

Table 3
Optical Depth and Column Density of $^{12}\text{C}^+$ at Selected Positions

Position	α_{2000} (h m s)	δ_{2000} ($^{\circ}$ ' ")	$I_{12} (^{12}\text{C}^+)^{\text{a}}$ (K km s $^{-1}$)	$I (^{13}\text{C}^+)^{\text{b}}$ (K km s $^{-1}$)	$v_{1,\text{LSR}}^{\text{c}}$ (km s $^{-1}$)	Δv_1^{c} (km s $^{-1}$)	$v_{2,\text{LSR}}^{\text{c}}$ (km s $^{-1}$)	Δv_2^{c} (km s $^{-1}$)	$\langle \tau (^{12}\text{C}^+) \rangle$	T_{ex} (K)	$N(\text{C}^+)$ (10^{18} cm $^{-2}$)
Average ^d	05 35 14.5	−05 21 59.5	621 ± 21	21.6 ± 0.4 18.4 ± 0.7	7.07	2.60	9.38	4.50	2.0 $^{+0.5}_{-0.4}$ 1.6 $^{+0.5}_{-0.4}$	178.1	13 $^{+4}_{-3}$ 10 $^{+4}_{-3}$
A	05 35 16.1	−05 22 15.2	617 ± 20	22.8 ± 0.5 23.9 ± 1.2	8.93	2.49	10.95	6.61	2.2 $^{+0.6}_{-0.4}$ 2.3 $^{+0.6}_{-0.5}$	257.2 ± 3.2	9.7 $^{+1.9}_{-1.5}$ 10 $^{+2}_{-2}$
A'	05 35 17.4	−05 21 58.5	905 ± 30	38.4 ± 0.5 38.0 ± 2	8.93	2.49	10.95	6.61	2.6 $^{+0.6}_{-0.5}$ 2.4 $^{+0.6}_{-0.5}$	274.5 ± 1.5	18 $^{+3}_{-2}$ 17 $^{+3}_{-2}$
B	05 35 15.0	−05 23 52.5	1160 ± 38	44.7 ± 0.7	6.60	2.00	9.07	4.18	2.3 $^{+0.6}_{-0.4}$	298.7 ± 2.1	24 $^{+4}_{-3}$
C	05 35 16.5	−05 23 37.3	1034 ± 34	28.3 ± 0.9	8.09	2.27	10.22	4.90	1.4 $^{+0.5}_{-0.4}$	226.7 ± 3.5	10 $^{+3}_{-2}$
D	05 35 16.2	−05 23 29.0	1002 ± 33	32.5 ± 0.8 33.4 ± 1.6	8.14	2.96	11.00	4.16	1.8 $^{+0.5}_{-0.4}$ 1.9 $^{+0.6}_{-0.4}$	188.1 ± 3.1	11 $^{+3}_{-2}$ 11 $^{+4}_{-3}$
E	05 35 12.5	−05 23 42.0	1009 ± 33	42.3 ± 2.6	6.07	2.79	8.78	3.69	2.6 $^{+0.7}_{-0.5}$	202.4 ± 2.7	24 $^{+6}_{-5}$
F	05 35 15.4	−05 24 08.1	932 ± 31	38.5 ± 0.4	7.12	2.52	8.98	3.88	2.5 $^{+0.6}_{-0.5}$	250.5 ± 1.6	30 $^{+6}_{-4}$
Hot Core	05 35 14.4	−05 22 30.0	423 ± 14	39.4 ± 1.9	3.67	6.90	8.69	3.67	6.2 $^{+1.3}_{-0.9}$	117.7 ± 5.4	35 $^{+9}_{-5}$
Hot Core-S	05 35 14.3	−05 22 34.5	496 ± 16	30.1 ± 1.8	3.67	6.90	8.69	3.67	4.0 $^{+0.9}_{-0.7}$	116.9 ± 5.9	25 $^{+7}_{-5}$

Notes.

^a The $^{12}\text{C}^+$ emission $I_{12} (^{12}\text{C}^+)$ is an integration of the two strongest components between +5 and +15 km s $^{-1}$.

^b Integrated $^{13}\text{C}^+$ intensities are estimated as a sum of all three hyperfine transitions (see Table 2), using a fit to the $F = 2-1$ component and the partition rule (see Section 3.3.2). Second values of $I(^{13}\text{C}^+)$ for the Average and positions A, A', and D are from direct measurements of all three observed components.

^c LSR velocities and widths are measured from the two strongest $^{12}\text{C}^+$ emission components peaking between +5 and +15 km s $^{-1}$.

^d The “average” position refers to the area in common to all spectral maps in this study, excluding the inner 12" around IRc 2; see Figure 1.

equal to or higher than the elemental abundance ratio. However, our measured $^{12}\text{C}^+ / ^{13}\text{C}^+$ intensity ratios at all positions in Orion BN/KL are *lower* than the adopted $^{12}\text{C} / ^{13}\text{C}$ isotopic abundance ratio of 67_{-5}^{+6} , indicating that moderate to high optical depths of C^+ lead to a reduction in the $^{12}\text{C}^+ / ^{13}\text{C}^+$ intensity ratio, thereby offsetting the effect of a $^{12}\text{C}^+ / ^{13}\text{C}^+$ abundance ratio enhanced by chemical fractionation or isotope-selective photodissociation. A similar conclusion was reached by Keene et al. (1998) with ^{12}C I, ^{13}C I, $^{12}\text{C}^{18}\text{O}$, and $^{13}\text{C}^{18}\text{O}$ observations at a position near Orion S. Their derived $\langle \tau \rangle$ for C 14' south of IRc 2 is comparable to what we estimate for C^+ in Orion KL, while isotopic abundance ratios in Orion S are also close to that of the ISM. This indicates either that carbon fractionation is negligible or that the $^{13}\text{C}^+$ abundance is enhanced by photodissociation of ^{13}CO in the strong FUV field. Ossenkopf et al. (2013) have concluded that isotope-selective photodissociation plays a very minor role in their PDR models for the Orion Bar region.

The excitation temperature T_{ex} is related to the measured radiation temperature T_{R} through the equation (e.g., Goldsmith & Langer 1999)

$$T_{\text{R}} = \left(\frac{T_{*}}{\exp(T_{*}/T_{\text{ex}}) - 1} - \frac{T_{*}}{\exp(T_{*}/T_{\text{bg}}) - 1} \right) [1 - e^{-\tau}] \quad (\text{K}). \quad (4)$$

For optically thick C^+ line emission that fills the HIFI beams,

$$T_{\text{ex}}(\text{C}^+) = \frac{91.2}{\ln[1 + 91.2/(T_{\text{MB}}(^{12}\text{C}^+) + T_{\text{c}}(1900.5))]} \quad (\text{K}) \quad (5)$$

where $T_{\text{MB}}(^{12}\text{C}^+)$ is the line peak on a main-beam temperature scale and $T_{\text{c}}(1900.5)$ is the continuum brightness temperature (as defined in Section 3.2) in K, including source continuum emission and a cosmic microwave background component of 2.74 K. Goicoechea et al. (2015) have noted the rather low brightness temperatures compared to the peak temperatures of the main spectral component across OMC 1. Over our mapped region, $T_{\text{c}}/T_{\text{MB}}$ is at most $\approx 5\%$, occurring at the location where peak continuum emission is strongest, which is where C^+ line emission is weak in the direction of SMA 1. Equation (4) assumes that the HIFI beam is filled, while Figures 7 and 8 prove that some of the emission is very structured, with spatial variations below the beam widths. For this weak, structured emission the assumption of a filled beam is not well justified, but for the peak emission, the spatial profile is much smoother.

The distribution of C^+ excitation temperatures estimated using Equation (5) is shown Figure 9. Over this region $T_{\text{ex}}(\text{C}^+)$ ranges from a minimum of 73 K to the west of SMA 1, to a maximum of 300 K at Position B, with an average $\langle T_{\text{ex}} \rangle = 178$ K. This value is comparable to that estimated toward θ^1 Ori C by Boreiko & Betz (1996) and adopted for the Orion Bar PDR by Ossenkopf et al. (2013), but is almost a factor of 2 higher than the average $T_{\text{ex}}(\text{C}^+)$ reported over the larger area of 75 arcmin² mapped over OMC 1 by Goicoechea et al. (2015b), who also assumed that all C^+ emission is optically thick. The higher Orion BN/KL average is probably explained by the closer proximity of the mapped gas to the

Trapezium stars, although there is no strict trend of temperature decreasing with projected distance from the Trapezium within this region, as can be seen in values of T_{ex} in Table 3 for the different locations. For the values of T_{ex} given in Table 3, we used the form of Equation (5) without taking a limit on τ , instead using the optical depths derived specifically for each location.

The column densities of C^+ are given in Table 3, calculated using the derived optical depths and excitation temperatures. Outside the Hot Core region, the average column density $\langle N(\text{C}^+) \rangle \simeq 1.0 \times 10^{19} \text{ cm}^{-2}$ agrees almost exactly with the value estimated by Ossenkopf et al. (2013) for the Orion Bar where C^+ intensity peaks and is a factor of 3 higher than the OMC 1 average quoted by Goicoechea et al. (2015b), while the column densities at the positions marked in Figure 3 around BN/KL are a factor of 2–3 higher than at the Orion Bar peak.

3.4. Morphology of $\text{CH}^+ J = 1-0, 2-1$

The distributions of emission intensity around Orion BN/KL from transitions to the ground and first excited levels of CH^+ are shown in Figures 10 and 11, integrated over v_{LSR} between 0 and +20 km s⁻¹. Column densities $N(\text{CH}^+)$ based on the $J = 1-0$ measurements, where we have largest spatial coverage, are included with Figure 10, calculated at an excitation temperature $T_{\text{ex}}(\text{CH}^+) = 30$ K, as discussed below. For comparison, the overall distribution of the $\text{CH}^+ J = 1-0$ emission in OMC 1 (right panel of Figure 1) appears similar to that of the 350 μm (857 GHz) emission mapped with SPIRE. The $\text{CH}^+ J = 1-0$ line falls within the SPIRE filter bandpass, but CO $J_{\text{upper}} = 5$ through 8 probably dominates the extended emission, especially toward the BN/KL complex. Continuum emission extending from Orion South to Orion North, peaking in the Hot Core region, also contributes. The extended CH^+ emission from the larger OMC 1 map (see Figure 1, right) roughly encircles a 3.1 diameter region of cloud surfaces bound by strongest emission from the Orion Bar PDR, the Orion South star formation site, the Hot Core and BN/KL complex, and a diffuse arc of emission extending to a bright region of CH^+ emission just to the north of the Orion Bar at its eastern extent.

The emission of CH^+ is somewhat more smoothly distributed than that of C^+ , exhibiting lower variations in peak intensity overall. There are no convincing indications of $\text{CH}^+ J = 1-0$ absorption along any line of sight. Toward the BN/KL complex, the $J = 1-0$ intensity is $\approx 30\%$ lower whereas the C^+ emission is more than a factor of 2 lower (see Tables 3 and 4) compared to the respective averages. In this line of sight, the baseline around the CH^+ line is partially blended with other molecules such as SO_2 and CH_3OH and their isotopologues emitting at nearby frequencies, so that we cannot be certain about possible $\text{CH}^+ J = 1-0$ absorption.

The CH^+ emission peaks exhibit a range of v_{LSR} between 7.0 and 11.0 km s⁻¹, while the distribution of large bright features is similar to that of C^+ , i.e., there are similar locations of the C^+ Peak A and a CH^+ peak emission near the Hot Core, as well as in the peaks to the south of the Compact Ridge. The highest $\text{CH}^+ J = 1-0$ emission peak is similarly located in an arc of material projected to the south of θ^1 Ori C. There is a tendency for the strongest CH^+ emission to occur where C^+ intensity gradients are strongest, but a notable distinction of the CH^+ emission is that LSR velocities are redshifted $\approx +2$ km s⁻¹ and are almost twice as broad on average as the main emission component of C^+ . At C^+ velocities below 8 km s⁻¹ and above

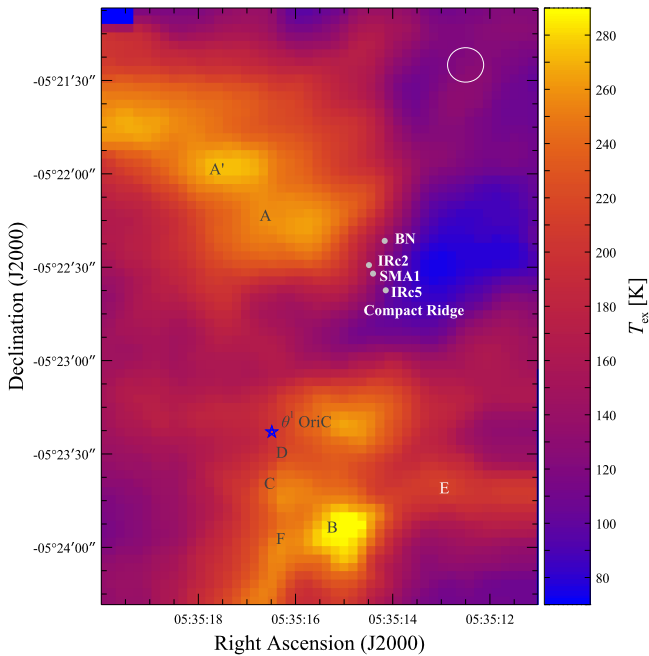


Figure 9. Excitation temperatures for main emission component of $^{12}\text{C}^+$ estimated from Equation (1).

10 km s^{-1} there is far less correspondence with the distribution of CH^+ emission (comparing Figure 6 with Figure 10). The coarse radial layering of C^+ and CH^+ around $\theta^1 \text{ Ori C}$, in which the C^+ emission peak is closer to the Trapezium stars, is compatible with photodissociation of the molecular gas in the hot stars' strong UV field. By contrast, C^+ peaks in projection further to the NE of BN/KL than CH^+ , which does not match a PDR scenario for a source of UV radiation from the BN/KL complex or the Trapezium on the arcminute scale. Goicoechea et al. (2015a, 2015b) showed that the C^+ emitting region is widespread in OMC 1, and although it is not exactly following the distribution of CO, which has its own velocity-dependent morphology, the overall ionized/PDR/molecular gas interfaces are revealed on the *larger* scales across OMC 1, through comparison of hydrogen recombination, CO $J = 2-1$, and C^+ integrated intensity distributions.

3.4.1. CH^+ Absorption

The distribution of CH^+ $J = 2-1$ emission is consistent with that of $J = 1-0$ over the region mapped in common, as seen by comparing Figures 10 and 11. The only difference is toward the dense core region where strong $J = 2-1$ absorption is detected. As noted above, there is no indication of absorption in the $J = 1-0$ line, though we cannot rule it out due to strong emission and crowding by other emitting molecules. We can only conclude that the relative strengths of the absorption lines are $I_{\text{abs}}(1-0)/I_{\text{abs}}(2-1) < 1$. Figure 12 compares profiles at Position A and the Hot Core (centered on SMA 1) with a $30''$ extraction aperture, and shows the overall averages. The comparison shows that the $J = 1-0$ line fluxes extracted over the same aperture size (which gives the same result if we convolve the 1670 GHz observations to the beam size at 835 GHz) are below average strength toward the Hot Core (see also columns 1 and 2 of Table 4). A low absorption ratio of $I_{\text{abs}}(J_u = 1)/I_{\text{abs}}(J_u > 1)$ is thought to be an excitation signature of a diffuse column of material undergoing processes

of dissipative turbulence, in contrast to regions in which the level populations are governed by formation pumping (Godard & Cernicharo 2013). On an optical depth scale, as in Figure 13, the $J = 2-1$ line is a 25% absorber of the 14 K continuum toward BN/KL, using a spectral extraction aperture of $30''$ diameter. The absorption implies an excitation temperature of the absorbing material

$$T_{\text{ex}}(\text{CH}^+) < \frac{80.1}{\ln[1 + 80.1/T_c(1669)]} \simeq 25.0 \text{ K} \quad (6)$$

where the continuum brightness temperature at 1669 GHz, $T_c = 80.1/(e^{80.1/T_{\text{bg}}} - 1) \simeq 3.4 \text{ K}$. The continuum levels are much lower at 850 GHz, $\approx 5.5 \text{ K}$, yielding $T_c = 0.7 \text{ K}$ and an absorption condition $T_{\text{ex}} < 10 \text{ K}$ on the $J = 1-0$ line. While we cannot claim that $J = 1-0$ is not in absorption due to the mentioned emission line crowding, we can assert that it is *not detected* either directly or by profile decomposition, thus $10 \text{ K} < T_{\text{ex}}(\text{CH}^+) < 25 \text{ K}$.

The Gaussian decompositions of the Hot Core CH^+ spectra are numerical best fits, but are not unique due to blending with nearby emission features. For example, the best fit to the $J = 2-1$ profile yields an emission component at $v_{\text{LSR}} = 12.6 \text{ km s}^{-1}$, considerably redshifted from the average of 9.5 km s^{-1} . If we were to fix the emission component to the average LSR velocity, the next best fit at nearly equal confidence level yields 30% weaker emission, and the absorption profile must be fit by two Gaussian profiles at LSR velocities v_{LSR} of 6.1 and 8.4 km s^{-1} , and widths Δv of 5.9 and 3.8 km s^{-1} . Hence, the column densities tabulated in Table 4, which are based on an average of measurements of both $J = 1-0$ and $2-1$ (weighted by S/Ns), may be somewhat overestimated toward the Hot Core due to this fitting uncertainty. If we rely on only the $J = 1-0$ line in the Hot Core spectrum, which is how Figure 10 has been produced, then the value of $N(\text{CH}^+)$ toward the Hot Core decreases by around 35%. The uncertainty is entirely attributable to blending with nearby species and the mixed gas temperatures in this line of sight.

3.4.2. CH^+ Emission

Outside the Hot Core line of sight, the ground and first excited CH^+ transitions share a similar kinematic structure; see Table 4 for v_{LSR} and line widths. Both $J = 1-0$ and $2-1$ emission lines are well fit by a single Gaussian profile over most of the mapped regions with v_{LSR} in the range of $9.3-10.0 \text{ km s}^{-1}$ (with the exception of Position E with $J = 1-0$ emission at 7.3 km s^{-1}), and widths Δv_{LSR} in the range of $4.6-6.4 \text{ km s}^{-1}$. At Peaks A, A', and toward the nearby Hot Core we detect a secondary component of $J = 1-0$ emission redshifted to $13-15 \text{ km s}^{-1}$, which is strong enough to be observed in the overall average spectrum. Only at Position A can we detect the second component in the $J = 2-1$ emission profile, consistently redshifted but at a lower intensity ratio with respect to the main component compared to the corresponding $J = 1-0$ ratio of the two velocity components at the same position.

A minimum of two rotational transitions of CH^+ can be used to derive rotational temperatures T_{rot} following the analytical expressions by Goldsmith & Langer (1999), using a linear fit to a Boltzmann excitation diagram of the emission lines at each map point. With this approach, plotting the logarithm of the

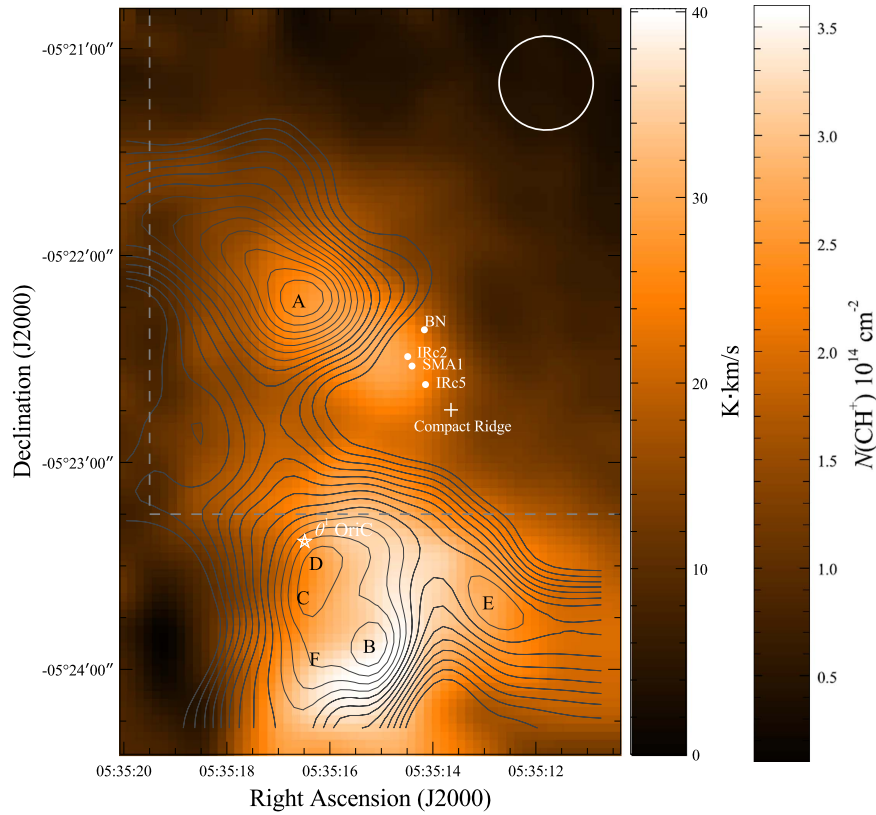


Figure 10. $\text{CH}^+ J = 1-0$ intensity integrated over -5 to $+20 \text{ km s}^{-1}$ and a column density scale calculated at $T_{\text{ex}} = 30 \text{ K}$, with contours of $^{12}\text{C}^+$ integrated over -10 to $+15 \text{ km s}^{-1}$ in gray on a linear scale between 450 and 850 K km s^{-1} (approximating the upper 65% of the total power) at intervals of 25 K km s^{-1} . The dashed box represents the area mapped in the $\text{CH}^+ J = 2-1$ line (see Figure 11).

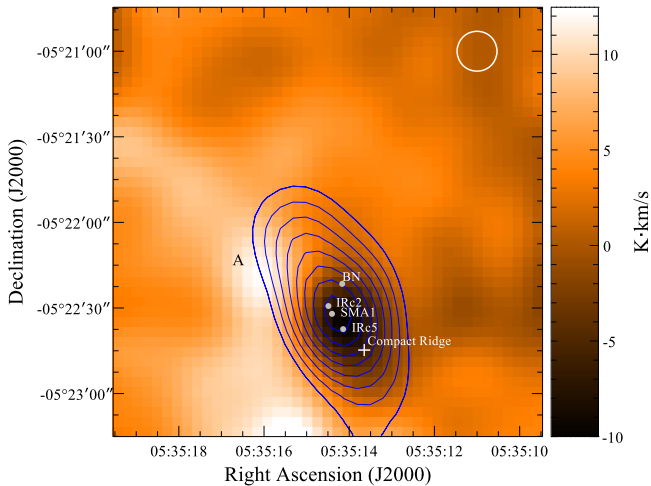


Figure 11. Integrated $\text{CH}^+ J = 2-1$ intensity with contours of the 1900 GHz continuum as in Figure 3.

column density per rotational level, $\ln(N_J/g_J)$, versus energy, E_J , and fitting a straight line between the two CH^+ transitions yields rotational temperatures in the range $25-35 \text{ K}$ (Figure 14), which is clearly sub-thermal. The column densities are a few times 10^{13} cm^{-2} .

The assumption of a single temperature (or of strict LTE) of the emitting gas is required along all sightlines in order to derive the column density from a linear slope ($-1/kT$) in the Boltzmann diagram. If this condition is not met, the shape of the curve can deviate from linearity, as Neufeld (2012) has

shown with *Herschel*/PACS observations of the CO ladder along various warm ISM sightlines. The sub-thermal value of T_{rot} derived from these Orion BN/KL observations of the two lowest rotational lines of CH^+ could be an indicator of negative curvature of the Boltzmann excitation curve that would be revealed when higher- J transitions are included. A nonlinear curve does not necessarily mean that non-LTE conditions prevail, but to get a reliable estimate of column density, the partition function must be known, and for this we need to know T_{ex} for all transitions. This is the same number only in LTE. Otherwise the column densities based on only two lines may be incorrect. Nonetheless, the excitation (i.e., rotation) temperature of the absorbing material revealed by the $\text{CH}^+ J = 2-1$ Hot Core profile (Figure 12) that we estimated using Equation (6) is in very close agreement with T_{rot} along that sightline. Similarly, the range of excitation temperatures based on the emission lines is $25 \text{ K} \leq T_{\text{ex}}(\text{CH}^+) \leq 32 \text{ K}$ at Peaks A, A', and the Hot Core, using the appropriate form of Equation (4) with $T_* = 80.1 \text{ K}$, again in very good agreement with the temperatures from the simple rotation diagram. Hence a consistent value of T_{ex} is reached by different analytical approaches, further implying that a single CH^+ gas temperature is a good approximation.

In order to further explore the formation and excitation of CH^+ in this region, we next compare the observed line intensities to predictions by PDR and full radiative transfer modeling, proceeding in a similar way to the recent study by Nagy et al. (2013) of reactive ions CH^+ , SH^+ , and CF^+ observed in the Orion Bar. To do so, we must include higher- J transitions which were observed as part of the HEXOS

Table 4
Line Measurements of CH⁺ at Selected Positions

Position	I_1 ($J = 1-0$ comp. 1)	$v_{\text{LSR},1}$	Δv_1	I_2 ($J = 1-0$ comp. 2)	$v_{\text{LSR},2}$	Δv_2	I_1 ($J = 2-1$ comp. 1)	$v_{\text{LSR},1}$	Δv_1	I_2 ($J = 2-1$ comp. 2)	$v_{\text{LSR},2}$	Δv_2	$N(\text{CH}^+)$ (10^{14} cm^{-2})
Average	10.1	9.4	5.4	1.1	12.9	14.7	1.9	8.7	3.9	0.8
A	16.4	9.3	4.7	12.2	12.8	12.1	5.5	10.0	4.7	1.7	14.8	3.3	2.6
A'	12.8	9.3	5.1	13.6	12.6	13.5	4.9	10.3	4.1	1.4
B	36.8	9.0	5.4	nc	nc	nc	nc	nc	nc	3.3
C	24.6	10.1	6.1	nc	nc	nc	nc	nc	nc	2.3
D	30.2	10.2	6.4	nc	nc	nc	nc	nc	nc	2.5
E	27.5	7.3	6.1	nc	nc	nc	nc	nc	nc	2.4
F	36.9	8.8	4.6	nc	nc	nc	nc	nc	nc	3.1
Hot Core	7.2	8.6	5.4	2.4	11.8	15.3	6.5	12.6	4.8	-28.9	8.8	9.3	3.1

Note. Column 1 positions are the same as in Table 3. Measurement uncertainties at all positions are 5%, except toward the Hot Core where the uncertainty in the $J = 2-1$ intensity is 20% due to strong blending with LOS absorption. Line-integrated intensities I are in units of K km s^{-1} , peak velocities v_{LSR} and velocity widths Δv are in km s^{-1} . Subscripts “1” and “2” denote the strongest and secondary components, where detected. Dotted entries indicate non-detections, “nc” at Positions B through F for the $J = 2-1$ line indicates no observational coverage. Column densities are computed with $T_{\text{ex}}(\text{CH}^+) = 30 \text{ K}$, and are based on averaging weighted by S/Ns of the emission measured from the ground and first excited level transitions at Positions A, A', the Hot Core (the fitted line emission component only), and the Average. All other positions are based on the $J = 1-0$ line only. The Hot Core South is not included due to strong overlap of signal with the Hot Core (due to the beam size at 835 GHz).

program, using the *Herschel*/PACS integral field unit spectrometer. The coverage of the PACS data is similar to that of our HIFI map of the $J = 2-1$ transition, represented as the gray box in Figure 1. From these data, we can measure only the $J = 4-3$ and $5-4$ lines toward C⁺ Peak A, and in overall averages that exclude the saturated BN/KL complex. We obtain estimates of 1.05 and 0.21 K km s^{-1} for $J = 4-3$ emission at Peak A and for the average, and similarly 0.33 and 0.13 K km s^{-1} (both upper limits accounting for uncertainty in surrounding baseline levels) for $J = 5-4$. Unfortunately, nonlinear photometric responses caused by high brightnesses of the BN/KL region and spectral line confusion make it difficult to extract reliable $J = 3-2$ through $6-5$ line fluxes from these data. A full description of the observations and reductions of the PACS observations will be provided by J. R. Goicoechea et al. (2016, in preparation).

3.4.3. “RADEX” Radiative Transfer Models

We first analyze the observed CH⁺ line intensities using the non-LTE radiative transfer code RADEX (van der Tak et al. 2007), by applying physical parameters that are expected for the CH⁺ emitting gas. We include a continuum model based on measurements with the Short and Long Wavelength Spectrometers that flew on the *Infrared Space Observatory*, and with *Herschel*/HIFI as described in Crockett et al. (2014) and references therein. The collisional rates for CH⁺-He collisions were taken from Turpin et al. (2010) and were scaled to represent CH⁺-H₂ collisions based on Schöier et al. (2005). Collisional rates for CH⁺-e⁻ collisions are taken from Lim et al. (1999); see also Hamilton et al. (2016). As CH⁺ is very reactive, inelastic collision rates with H₂ and electrons are similar to the chemical reaction rates with these species (e.g., Stäuber & Bruderer 2009). Therefore, we consider the chemical formation and destruction rates in the statistical equilibrium calculation as described in Nagy et al. (2013). However, in Nagy et al., due to the lack of knowledge of the state-to-state formation rates of CH⁺, the formation rate into level i was expressed as a Boltzmann distribution over all states at an effective formation temperature T_f . In this paper we use the state-to-state formation rates for the reaction $\text{H}_2(v=1) + \text{C}^+ \rightarrow \text{CH}^+ + \text{H}$ computed by Zanchet et al. (2013).

Line intensities or upper limits are available for four transitions toward the C⁺ Peak A position and in the average spectrum toward the measured area. RADEX models for CH⁺ line intensities toward the Orion Bar suggested high kinetic temperatures, such as 500 K. Assuming a kinetic temperature of 500 K and an H₂ volume density of $5 \times 10^5 \text{ cm}^{-3}$, the observed line intensities are consistent with a CH⁺ column density of $1 \times 10^{14} \text{ cm}^{-2}$ for the Orion BN/KL Average and $3 \times 10^{14} \text{ cm}^{-2}$ at Peak A; see Figure 15. The excitation temperatures are in the range between 23 and 40 K from low to high J for both models. For these results we assumed an electron density of 10 cm^{-3} . Increasing the electron density to 100 cm^{-3} increases the predicted integrated intensities by factors of 1.3–1.4. If we assume an electron density of 100 cm^{-3} and apply the H₂ volume density and kinetic temperature quoted above, then the CH⁺ column densities decrease to $8 \times 10^{13} \text{ cm}^{-2}$ and $2 \times 10^{14} \text{ cm}^{-2}$ toward the Orion BN/KL average and Peak A, respectively. The value of 100 cm^{-3} is approximately where n_e peaks at maximum cloud penetration depth, as will be shown in the next section. Furthermore, since CH⁺ is produced where C⁺ is the dominant ion, n_e scales with n_{H_2} ; then at the H₂ density of $5 \times 10^5 \text{ cm}^{-3}$ assumed above, $\text{C}/\text{H} = 1.4 \times 10^{-4}$, all carbon is ionized, and $n_e \approx 140 \text{ cm}^{-3}$.

To investigate the role of the background continuum in the excitation of CH⁺, we ran models where we ignored the background continuum measured toward Orion BN/KL (which has a mean dust temperature of $\approx 30 \text{ K}$; Goicoechea et al. 2015b) and assumed only a cosmic microwave background temperature of 2.76 K. In this case, the excitation temperatures drop by factors of 1.2–2.9. The integrated intensities for the three lowest transitions increase from 1%–50%, and then decrease by 8%–21% for the $J = 4-3$ and $5-4$ transitions.

In conclusion, the CH⁺ column density is $(0.8-1.0) \times 10^{14} \text{ cm}^{-2}$ for the Orion BN/KL average, and it is $(2-3) \times 10^{14} \text{ cm}^{-2}$ toward the C⁺ Peak A. The excitation of CH⁺ is affected by its formation and destruction, the continuum radiation field (such as for other reactive ions like OH⁺, van der Tak et al. 2013), and the electron density.

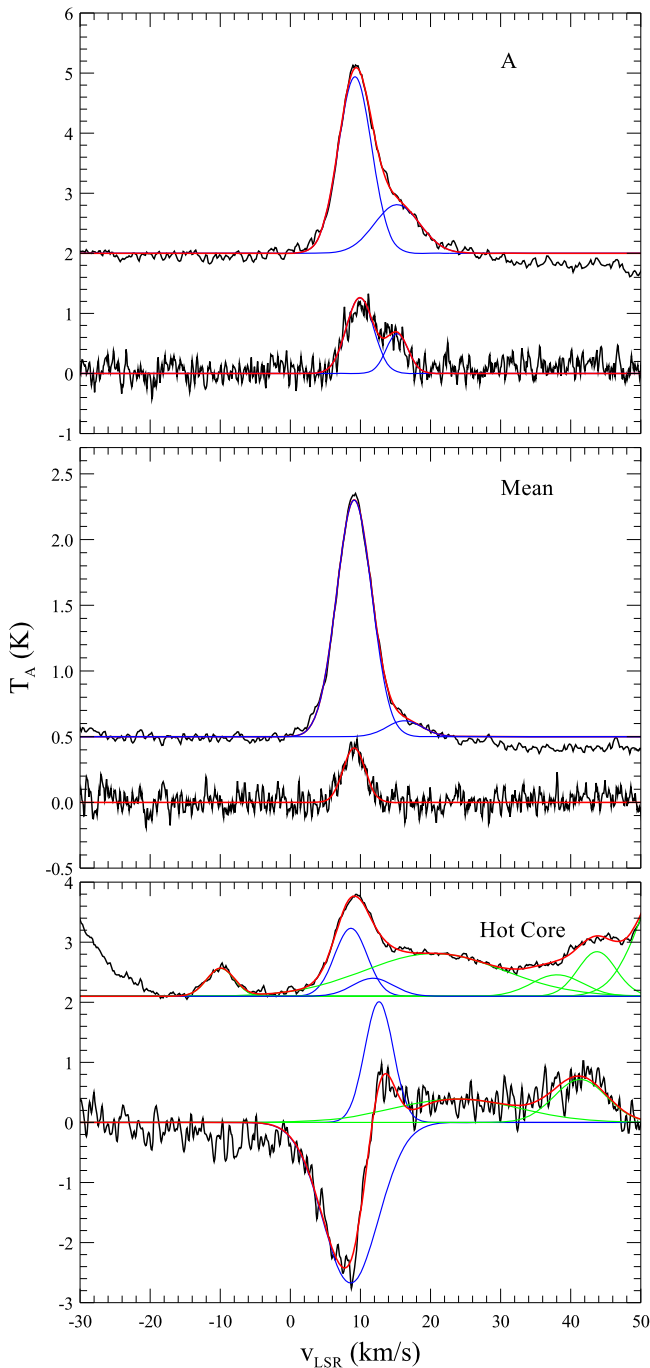


Figure 12. CH^+ $J=1-0$ and $2-1$ spectra at Position A (top panel), averaged over the common mapped area around BN/KL (middle panel), and toward the Hot Core region (bottom panel). Continuum levels have been subtracted, and in each panel the $J=1-0$ spectrum is plotted on top, offset for clarity. Spectra at C^+ Peak A and the Core regions have been extracted over a circular aperture of $30''$ diameter suited to the HIFI beam at 835 GHz. The mean spectrum corresponds to the region marked by the dashed box in Figure 10, excluding a region of $30''$ diameter centered on IRe 2 where CH^+ $J=2-1$ is in absorption. Gaussian profiles obtained by Levenberg–Marquardt minimization are shown in blue for each attributed CH^+ component, in green for nearby features from other species contributing to the overall fit, and in red for the total model. Best-fit parameters for the CH^+ components are given in Table 4.

3.4.4. PDR Models

Intensities of the CH^+ emission lines in Orion KL have been further modeled using the Meudon PDR code v 1.4.4 (Le Petit et al. 2006; Goicoechea & Le Bourlot 2007; Le Bourlot

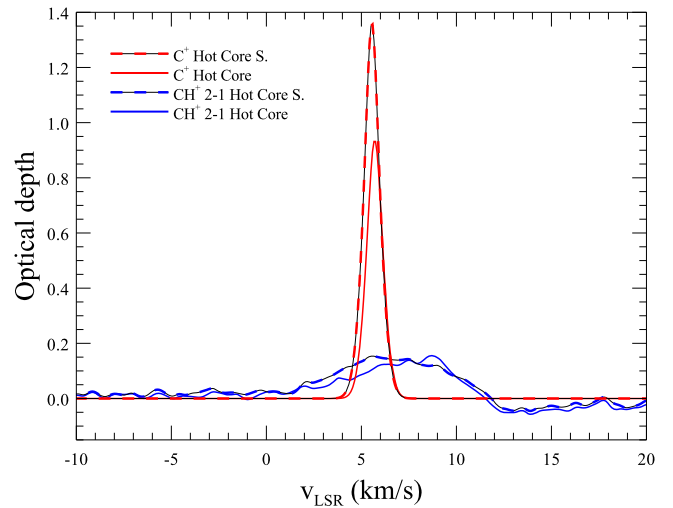


Figure 13. Optical depths of the C^+ and CH^+ $J=2-1$ lines toward the Orion Hot Core and Hot Core South as indicated, each extracted in an aperture of $30''$ diameter. No CH^+ $J=1-0$ absorption is observed (see text).

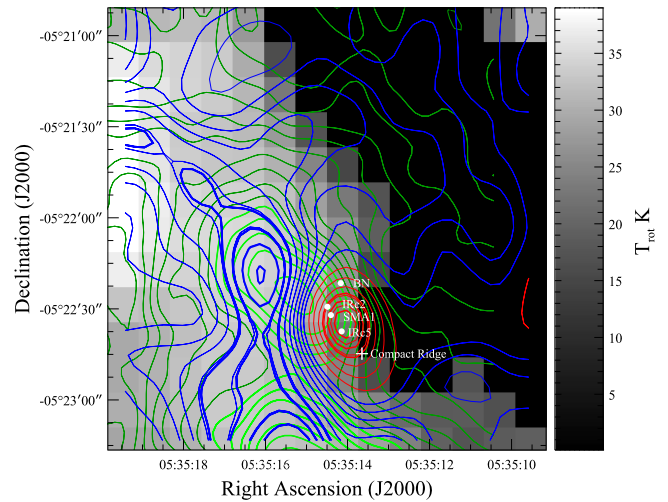


Figure 14. Rotational temperature map of CH^+ derived from the $J=1-0$ and $2-1$ emission lines, under the assumption that the emitting gas is in LTE at a single temperature, i.e., there is a linear slope ($-1/kT$) in the Boltzmann excitation representation. Overlaid are contours of integrated intensities: the $J=1-0$ emission (green) between 0 and 34 K km s^{-1} at intervals of 2 K km s^{-1} ; $J=2-1$ emission (blue) between 0 and 10 K km s^{-1} at intervals of 1 K km s^{-1} ; and $J=2-1$ absorption (red) between -0.5 and $-12.5 \text{ K km s}^{-1}$ at intervals of 2 K km s^{-1} . Thick contours indicate the upper 60% power of integrated intensities. The two pixels in the upper right (NW) corner of the map are spurious, where detection of $J=2-1$ emission is at the noise limit.

et al. 2012), following the approach of Nagy et al. (2013). Isobaric models were run for a grid of pressures and radiation fields around the best-fit parameters for the Orion Bar PDR through a depth equivalent of $A_V = 10$ mag (comparable to the beam size of the $J=1-0$ observations, or $\approx 5.0 \times 10^3$ AU at the distance of 420 pc to Orion BN/KL), with the gas illuminated from two sides by a radiation field $\chi = \chi_{\text{front}} = 1000\chi_{\text{back}}$ in Draine units, and a cosmic-ray ionization rate $\zeta = 2 \times 10^{-16} \text{ s}^{-1}$. The initial elemental abundances of He, C, N, O, S, and Fe that we adopt in our models are the values in the Meudon PDR code suited to diffuse clouds (see Table 6 in Le Petit et al. 2006), which are relative to the total number density of H nucleons. The atomic

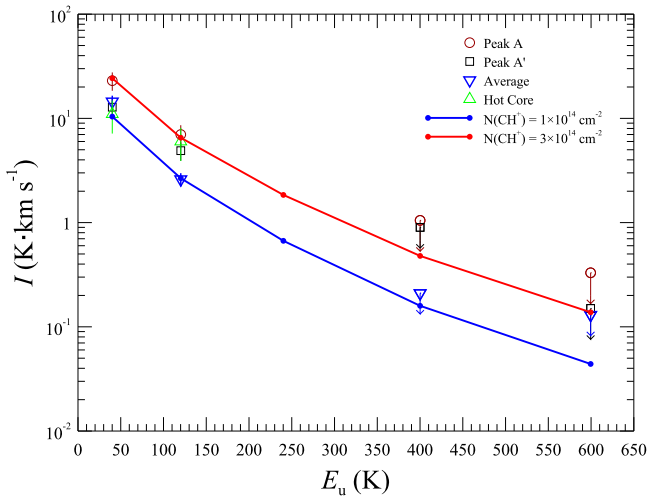
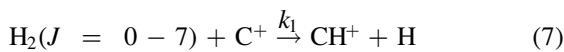


Figure 15. The CH^+ line intensities measured toward Orion BN/KL peak positions A and A', the Average, and the Hot Core (toward SMA 1), with symbols given in the legend. Plotted values for the $J = 4-3$ and $5-4$ integrated line fluxes are upper limits. The overplotted RADEX models in red and blue dots correspond to a kinetic temperature of 500 K, an H_2 volume density of $2 \times 10^5 \text{ cm}^{-3}$, an electron density of 10 cm^{-3} , and CH^+ column densities as indicated.

and molecular hydrogen number densities are given by $n_{\text{H}} = n(\text{H}) + 2n(\text{H}_2) = 2 \times 10^5 \text{ cm}^{-3}$. We also adopt a ratio of extinction to color excess $R_V \equiv A_V/E(B-V) = 5.6$, a ratio of gas to dust of 100, a grain size distribution index of 3.5 (Mathis et al. 1977 for a range of grain radii 0.003–0.3 μm), and $A_V/N(\text{H}) = 5.3 \times 10^{-22} \text{ mag cm}^2$.

Collisional excitation and de-excitation as well as the chemical pumping effect of destruction and formation of CH^+ on the level populations are treated in the Meudon code. The destruction of CH^+ occurs in collisions with H, H_2 , and electrons, and by photoionization at rates tabulated by Nagy et al. (2013), based on Woodall et al. (2007). The formation of CH^+ includes rotational and vibrational levels of H_2 to react with C^+ , as



(Hierl et al. 1997; Agúndez et al. 2010; Nagy et al. 2013), where rotational levels up to $J = 7$ (with an energy $E_{J=7} = 4586.4 \text{ K}$, close to the CH^+ activation barrier) are included for reaction, and the rate of formation through rotationally excited H_2 is $k_1 = 1.58 \times 10^{-10} \exp(-[4827 - E_J/k]/T) \text{ cm s}^{-1}$ (Gerlich et al. 1987). In the reaction with vibrationally excited H_2 , only the $\nu = 1$ level is needed since its energy $E_{\nu=1} = 5987 \text{ K}$ is sufficient to overcome the activation barrier, forming CH^+ at a rate $k_2 = 1.6 \times 10^{-9} \text{ cm s}^{-1}$ (Hierl et al. 1997).

Chemical equilibrium is assumed, though we must acknowledge some risk in the assumption due to the dynamic nature of the relatively young BN/KL outflow (e.g., Bally et al. 2011). The assumption can be justified for most of the mapped region by the lack of direct evidence of recent changes in gas dynamics that would influence the CH and CH^+ emission, for example as variations in line profiles. The profiles show very little variation across the region including sightlines to the northern and southern lobes of H_2 emission. We cannot assert

this to be true within $\approx 15''$ of the Hot Core itself, near the origin of the explosion some 500–1000 years ago, due to spectral confusion with methanol and SO_2 transitions. Therefore, the assumption of chemical equilibrium could break down for some portion of the gas, but this remains indiscernible in the current observations. In Section 4 we will also address formation timescales compared to the age of the outflow, and other chemical factors that may influence the CH^+ production there.

Figure 16 shows the results of the PDR models: good agreement with the observed intensities is obtained using a radiation field $\chi = 5 \times 10^3 \chi_D$ where χ_D denotes the field strength in Draine units, using a pressure $p/k = 1 \times 10^8 \text{ cm}^{-3} \text{ K}$ for the average line intensities, and $p/k = 2 \times 10^8 \text{ cm}^{-3} \text{ K}$ for those at Peak A. The applied radiation field is a factor of 2 lower than that required to reproduce the CH^+ emission in the Orion Bar, and the pressure is comparable to or twice the best-fit value for the Bar. Under these conditions, the total column density of CH^+ is $1-2 \times 10^{14} \text{ cm}^{-2}$ —in excellent agreement with estimates from non-LTE radiative transfer models described in Section 3.4.3, which is reassuring since both sets of models contain all of the important physical ingredients.

Figure 17 shows the calculated abundance profiles of CH^+ , CH, and the key species involved in their production, as well as the molecular fraction, ionization fraction, and gas temperature as a function of the visual extinction. The CH^+ abundance peaks in the outer layers of the cloud between 0.2 and 0.6 A_V , corresponding to low to intermediate values of the molecular fraction ($0.01 < f_{\text{H}_2} < 0.5$), an ionization fraction that is half that in the outermost layers of the cloud, and gas temperatures of 400–1000 K. By contrast, the CH abundance shows a broad peak from about 0.2 to 5 A_V over a range of ionization fractions, and reaches a maximum at $A_V = 2$, $f_{\text{H}_2} = 0.8$, and $T < 200 \text{ K}$. The C^+ abundance increases and the vibrationally excited $\text{H}_2(\nu = 1)$ abundance decreases over most of the region in which the CH^+ abundance is at its maximum. In addition, the $\text{H}_2(\nu = 1)$ abundance shows no correspondence with the CH abundance. Instead, the CH abundance corresponds well with the H_2 abundance through $A_V = 2 \text{ mag}$.

The calculated depth dependence may be understood qualitatively in terms of the chemistry of CH^+ and CH. The C^+ ion reacts with $\text{H}_2(\nu = 1)$ —produced efficiently only in the outer layers of the molecular gas—to yield CH^+ . The CH^+ thus formed can undergo dissociative recombination to yield C and H; the photoionization of C formed in this, as well as other processes, likely contributes to the increased C^+ abundance deeper into the cloud. Additionally, in gas of substantial molecular fraction, CH^+ can react exothermically with H_2 to yield CH_2^+ , which in turn undergoes dissociative recombination to yield CH. This may explain the higher calculated CH abundance deeper into the cloud, as well as the observed CH intensity peak closest to IRC 2, the region with the densest molecular gas.

We also note that while photoionization of neutral carbon provides the main source of free electrons in PDRs, additional contributing sources exist to raise the n_e/C^+ ratio above unity to depths of around $A_V = 3.0 \text{ mag}$. Other elements with low ionization potential (Mg, Si, S, etc.) contribute between 20% and 30% that of carbon. Also, H can be ionized by cosmic rays and soft X-rays and subsequently yields O^+ by charge transfer to O. The combination of these two mechanisms results in a

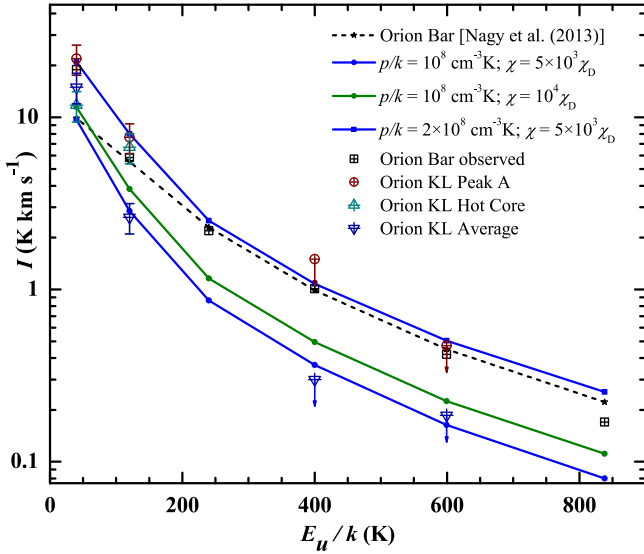


Figure 16. Observed intensities of CH^+ compared with those calculated from isobaric PDR models. The observed and calculated values for the Orion Bar PDR (Nagy et al. 2013) are shown for comparison.

higher electron abundance in the low- A_V region. In the higher- A_V region where carbon recombines, sulfur and other metals continue to provide electrons, until around $A_V = 3.0$ mag in our model. Indeed, the adopted S abundance is 1.9×10^{-5} , which alone would contribute about 15% of the electrons relative to those from carbon. The electron density n_e peaks at around the same depths as C^+ , which may result in an increase in CH production at such depths as CH_2^+ recombines.

Because the Meudon code applies to steady-state physical and chemical conditions, variations in the adopted atomic and molecular abundances have almost no effect on the output profiles of ionization abundances versus extinction. However, a more discernible effect can result from different extinction parameters. We have adopted a total to selective extinction ratio $R_V \equiv A_V/E(B-V) = 5.5$ and $A_V/N(\text{H}) = 3.5 \times 10^{-22} \text{ mag cm}^2 \text{ H}^{-1}$ (as have Nagy et al. 2013 for the Orion Bar, and Goicoechea et al. 2015b for the larger OMC 1 region) that are consistent with larger grains, leading to deeper penetration of the UV field, and producing a larger C^+ zone and higher values of $N(\text{C}^+)$. Similarly, a variation in the adopted UV field strength will have obvious impact on the atomic and molecular number densities at the cloud boundaries. The field strength and radiation pressures that we adopt give a best fit to the CH^+ line intensities and yield a C^+ layer to $A_V \approx 3$ mag, while Nagy et al. (2013) use a UV field strength for the Orion Bar that is a factor of ~ 2 higher (but no continuum radiation field), producing a C^+ layer to $A_V \approx 4$ mag. These effects are still minor and do not affect our conclusions, which demonstrate the role of UV chemistry around Orion BN/KL.

3.5. CH Λ -doubled Lines ${}^2\Pi_{3/2}$, ${}^2\Pi_{1/2}$

The ground state of CH is $X^2\Pi$ regular (i.e., $\Pi_{1/2}$ lower than $\Pi_{3/2}$), with a spin-orbit coupling constant of 843818.4 MHz. Figure 18 shows the lowest four rotational levels of CH. The unpaired electron couples with rotation, resulting in Λ doubling, and with the hydrogen spin, leading to clearly resolved hyperfine structure. We have spectrally mapped

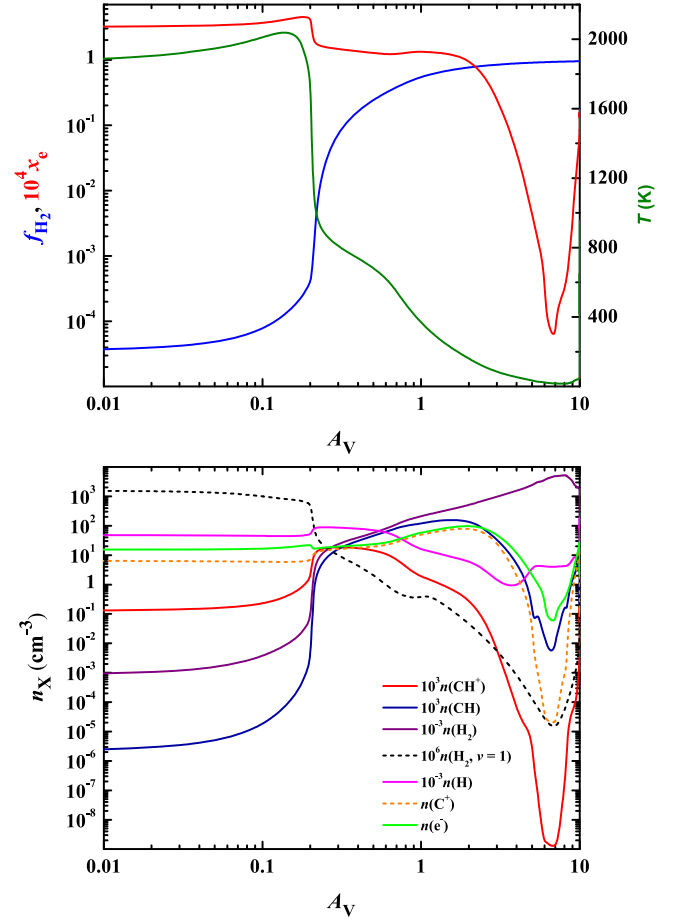


Figure 17. Depth dependence of parameters in the PDR model. Bottom: number densities of key species involved in the production of CH and CH^+ ; the values of all but C^+ and electrons are scaled for clarity of the comparisons. Top: profiles of the gas kinetic temperature, molecular fraction, and ionization fraction (scaled by a factor of 10^4). The results shown are for an isobaric PDR at a pressure $p/k = 10^8 \text{ cm}^{-3} \text{ K}$ and illuminated by a radiation field $\chi_{\text{front}} = 5 \times 10^3$, $\chi_D = 10^3 \chi_{\text{back}}$, where χ_D is the field strength in Draine units. Adopted initial atomic and molecular abundances and extinction parameters are described in the text.

emission from one of the ground-state cross-ladder pairs at 537 GHz (the 533 GHz hyperfine lines were not mapped). Continuum levels at this frequency peak at $T_c(557) = 2.1 \text{ K}$ toward SMA 1. The pairs at 1471/1477 and 1657/1661 GHz were observed only toward the Hot Core, where the continuum is much stronger, $T_c(1473) = 12.0 \text{ K}$ and $T_c(1658) \approx 13.0 \text{ K}$. These pairs both originate from the lowest level in the excited ${}^2\Pi_{3/2}$ state, and are lines in absorption; see Figure 19. The profile measurements are summarized in Table 5. The velocities and line widths are very similar to those of the CH^+ rotational lines, and likewise kinematically consistent with observations toward the Compact Ridge (e.g., Crockett et al. 2014).

All of the C^+ , $\text{CH}^+ J = 1-0$ and $2-1$, and $\text{CH}^2\Pi_{3/2} - {}^2\Pi_{1/2}$ profiles extracted from the Hot Core, Position A, as well as averages are compared in Figure 22 on a normalized intensity scale. Outside the Hot Core, the similarities in profile shape are very strong, especially in the averages where LSR velocities and line widths would be indistinguishable to within $\sim 2 \text{ km s}^{-1}$. Variance in the strength of the redshifted component can be seen in the C^+ peak Position A, but all species emit over the same redshifted velocity range.

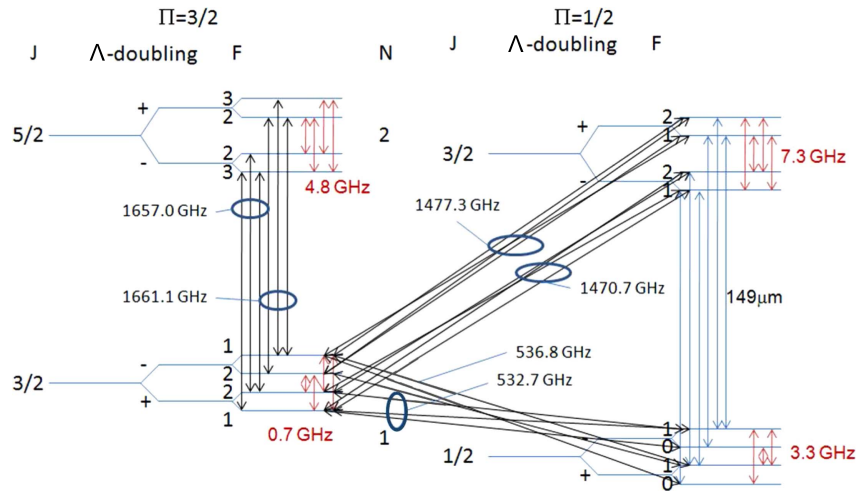


Figure 18. Level diagram for the lowest four rotational levels of CH. The Λ -doubling and hyperfine splitting are exaggerated for clarity. The red arrows represent microwave frequency Λ -doubling transitions. Black arrows are transitions that were within the HIFI frequency range, blue ellipses indicate those observed in this study and the blue lines represent the 2.0 THz transitions, which lie above the *Herschel* HIFI frequency range.

A key question concerns the location of the CH column around Orion BN/KL, and its relative abundance compared to H_2 . Previous observations show that CH traces H_2 well in the diffuse ISM. Steady-state models by Levrier et al. (2012) reproduce the observed trend of CH versus H_2 , without the need to invoke dissipation of turbulence. This might be understood from the fact that the observations sample CH in regions with a significant fraction of hydrogen in H_2 , $f(\text{H}_2) > 0.1$ up to ~ 1 , while CH^+ prefers regions of the ISM with low hydrogen fractions as H_2 , $f(\text{H}_2) < 0.5$. In the region around Orion BN/KL, however, we are in a regime of strong FUV irradiation.

The measured intensities of the 1656/1661 lines and 1471/1477 lines, -51 K km s^{-1} and $-12.6 \text{ K km s}^{-1}$, respectively, give the total column of the $\Pi_{3/2}$ $J = 3/2$ level of $1.25 \times 10^{14} \text{ cm}^{-2}$. Using the same arguments for the rotation (excitation) temperature of CH^+ in Sections 3.4.1 and 3.4.2, $T_{\text{rot}} = 35 \text{ K}$ is a reasonable upper limit for CH, and agrees well with a one-component model in LTE carried out with the XCLASS package,¹⁶ and checked with RADEX, yielding a total column from emission of $1.7 \times 10^{14} \text{ cm}^{-2}$ toward the BN/KL region. The total column decreases with higher values of T_{rot} .

Figure 20 shows the integrated intensity distribution of CH 537 GHz in the unblended and strongest $F = 2^- - 1^+$ transition. The distribution is quite similar to that of CH^+ , although the CH peak intensity is just slightly closer (in projection) to the BN/KL complex. In relation to θ^1 Ori C with its strong ionizing UV field, the highest CH intensities are radially exterior to those of CH^+ , as we might expect.

CH column densities for the $2^2\Pi_{3/2}$ state have been estimated from measurements of the 537 GHz $F = 2^- - 1^+$ line, and scaled using the partition function to include the $F = 1^- - 1^+$ and $1^- - 0^+$ contributions. Figure 21 shows $N(\text{CH})$ calculated in LTE at 35 K. We find that $N(\text{CH})$ toward the BN/KL complex is exactly as predicted using the 1471/1477 and 1656/1661 GHz absorption pairs at 35 K, which provides confirmation of the consistency of the measurements, not necessarily the LTE assumption and adopted T_{rot} .

Nonetheless, at positions where all three lines are unaffected by emission of other species (namely $\text{SO}_2 10_{4,6}-9_{3,7}$ 549.3 GHz observed toward the Hot Core in the opposite sideband and especially blending in the wings of the $F = 1^- - 0^+$ line; see Figure 19), the observed $1-0:1-1:2-1$ ratio is in excellent agreement with the theoretical partitioning 0.25:0.125:0.625. The CH column densities are generally lower than $N(\text{CH}^+)$ by factors of ≈ 1.2 to 3 at specific locations, and weaker by a factor of ≈ 5 on average over the area mapped in common. The usual relationship $[\text{CH}]/[\text{H}_2] = 3.5 \times 10^{-8}$ (Sheffer et al. 2008) gives a total column of H_2 of $\sim 5-12 \times 10^{22} \text{ cm}^{-2}$, which is consistent with that of the Compact Ridge (Plume et al. 2012) —higher than would be observed in a boundary layer and lower than would be expected from the Hot Core. The emission in the 537 GHz lines suggests that the critical density of $\sim 10^6 \text{ cm}^{-3}$ has been reached, but not by enough to cause emission in the higher lying transitions at sub-thermal excitation temperatures of $T_{\text{ex}}(\text{CH}) \lesssim 35 \text{ K}$.

3.6. Inferred $\text{C}^+/\text{CH}^+/\text{CH}$ Cloud Interfaces

Our HIFI spectral maps reveal two separate features visible in CH^+ and C^+ : one that is absorbing thermal radiation toward the BN/KL complex, and a structured cloud distribution of emission over the entire region enveloping BN/KL. Only the line profile of the first excited level of CH^+ reveals the absorption component. The ground-state profile shows no indication of absorption, and with the constraint $I_{\text{abs}}(J = 1-0)/I_{\text{abs}}(J = 2-1) < 1$ the excitation temperature of the absorbing gas is in the range 10–25 K, similar to the absorbing component of C^+ , but at lower optical depths. The excitation temperatures of the emitting CH and CH^+ gas are similarly sub-thermal, while C^+ excitation temperatures are much higher, $\approx 175 \text{ K}$ on average. Our derived C^+ excitation temperatures for the inner $3' \times 3'$ around BN/KL are higher by almost a factor of 2 compared to that toward the BN/KL as well as the overall OMC 1 average, as estimated by Goicoechea et al. (2015b), resulting in an increase by nearly the same factor in column densities. Nonetheless, the description by Goicoechea et al. based on similar PDR model predictions is confirmed here, namely that the C^+ emission across OMC 1 is tracing only the narrow cloud surface layers

¹⁶ P. Schilke, XCLASS public home page <http://www.astro.uni-koeln.de/projects/schilke/XCLASS/>.

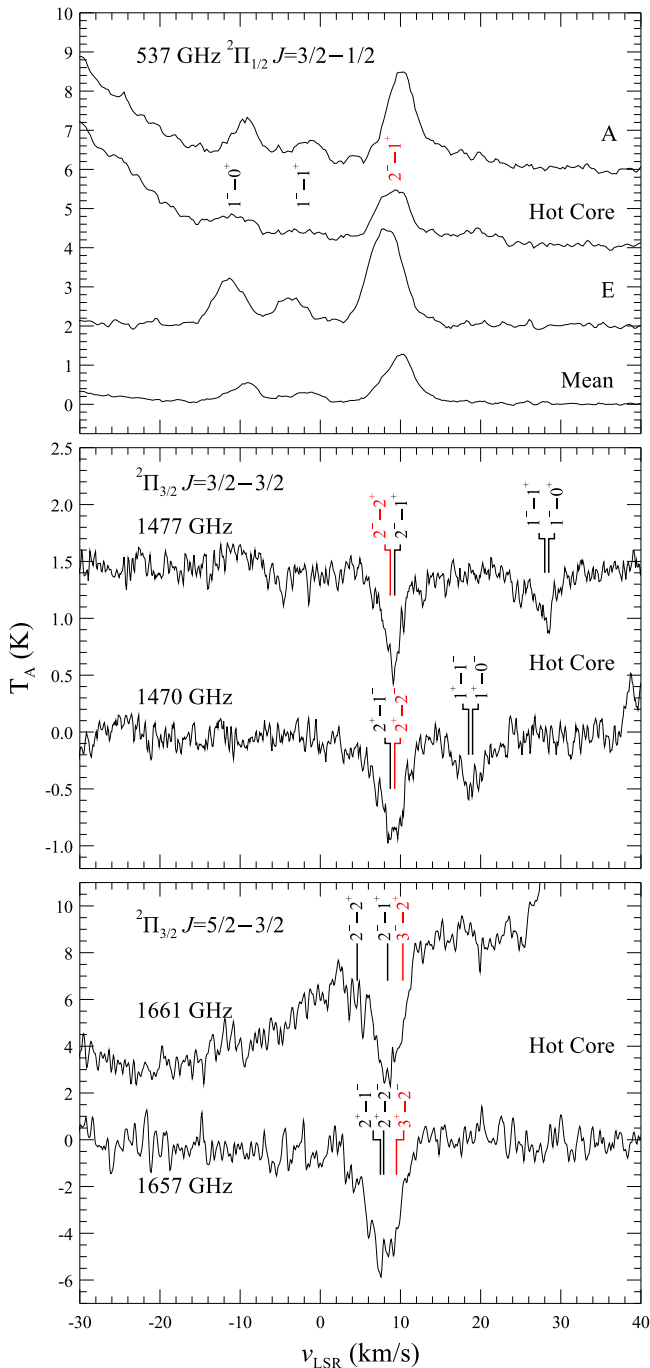


Figure 19. Observed CH Λ -doubled lines of the $^2\Pi_{1/2}$ state (upper panel) and $^2\Pi_{3/2}$ state (middle and lower panels). The 1471/1477 and 1661/1657 pairs have been observed in pointed mode toward the BN/KL complex, while the 537 GHz triplet has been spectrally mapped over an area similar to the CH^+ $J = 2-1$ line (see Table 1) and is plotted as the average. Continuum levels have been subtracted and spectra offset for clarity.

to $A_V < 4$ mag and not the full line of sight. Quantitative differences in the maximum penetration depth of C^+ in our modeling are small (peaking in abundance at $A_V \lesssim 3$ mag), partly as a result of a more detailed treatment of the dust extinction properties by Goicoechea et al. Our PDR models predict abundances of CH to peak at comparable penetration depths, while CH^+ peaks at much lower depths, $0.2 \text{ mag} \lesssim A_V \lesssim 0.6 \text{ mag}$. This is consistent with the predicted

Table 5
Line Measurements of CH $\Pi_{3/2} J = 3/2-1/2$ (537 GHz) at Selected Positions

Position	I (K km s $^{-1}$)	v_{LSR} (km s $^{-1}$)	Δv (km s $^{-1}$)	$N(\text{CH})$ (10^{14} cm $^{-2}$)
Average	10.3	9.7	5.7	0.7
A	20.0	10.4	4.7	1.5
A'	21.2	10.2	5.4	1.0
C	14.4	8.6	4.6	1.3
D	16.8	8.5	4.6	1.4
E	23.1	8.2	5.1	1.5
Hot Core	18.4	8.2	4.8	1.7

Note. Column 1 positions are the same as in Table 3. Integrated intensities I are summed over all three hyperfine components, while v_{LSR} and Δv are measured from the strongest $F = 2^+ - 1^-$. Measurement uncertainties at all positions are 5%, except toward the Hot Core and nearby Position A where the $F = 1^+ - 0^-$ and $1^+ - 1^-$ lines are weakly blended with $\text{SO}_2 10_{4,6-9_{3,7}}$ 549.30 GHz emission observed in the opposite sideband, and contribute 8%–10% uncertainty to the total integrated line intensity. Column densities $N(\text{CH})$ are calculated at $T_{\text{ex}}(\text{CH}) = 35$ K.

increase in electron densities at depths similar to the C^+ peak abundance, where CH^+ will easily react to form neutral CH.

Since the brightness distributions of C^+ , CH^+ , and CH are very similar, and indeed all profiles outside the Hot Core are very similar (see Figure 22), it is reasonable to think of these molecular components as situated in a halo around the Trapezium, with the kinematically more quiescent CH gas exterior to the CH^+ and C^+ . From the PDR model we expect an anticorrelation in an edge-on geometry at modest to low values of A_V . The good spatial correspondence of each species in emission may have three explanations: (a) face-on geometry of a veil illuminated by θ^1 Ori C; (b) very clumpy picture with surfaces everywhere; or (c) efficient dynamical mixing. Case (a) would be most consistent with conclusions for the larger OMC 1 cloud by Goicoechea et al. (2015b). The picture is more or less consistent with the ionized/PDR/molecular gas interfaces illustrated by Goicoechea et al., but the high reactivity of CH^+ allows CH to coincide with C^+ at higher A_V where electron densities are also higher. The picture illustrated by Goicoechea et al. is suited at a schematic level to the larger OMC 1 region, while the smaller region we have mapped in C^+ , CH^+ , and CH more deeply around BN/KL is inhomogeneous, with numerous projection effects from different kinematic components of C^+ and evidence for a mix of gas temperatures toward the Hot Core.

3.7. $\text{CH}_3\text{OH } K = 5 \leftrightarrow 4$ (E)

At the HIFI LO frequency setting used to map $\text{CH}^+ J = 1-0$ we have also detected a dozen of the strongest $\Delta J = 0$, $K = 5 \leftrightarrow 4$, $v_t = 0$ E-symmetry Q-branch methanol transitions centered at 834.8 GHz, with upper state energies ranging between 171 and 452 K. This is the only band in Orion that has been mapped with HIFI, and is ideal for studying the kinematics and physical conditions in the dense BN/KL core region, particularly since the observed transitions ($J_{u,l}$ 5 through 15) are isolated from CO, H_2O , OH, or other broad features. Only the $J_{u,l}$ 14 and 16 transitions in our detected set of lines are blended with SO_2 and HDO (respectively) from the opposite sideband.

The CH_3OH emission spectra are shown in Figure 23. We have taken $\sim 1/3$ beam-sized spectral extractions at positions

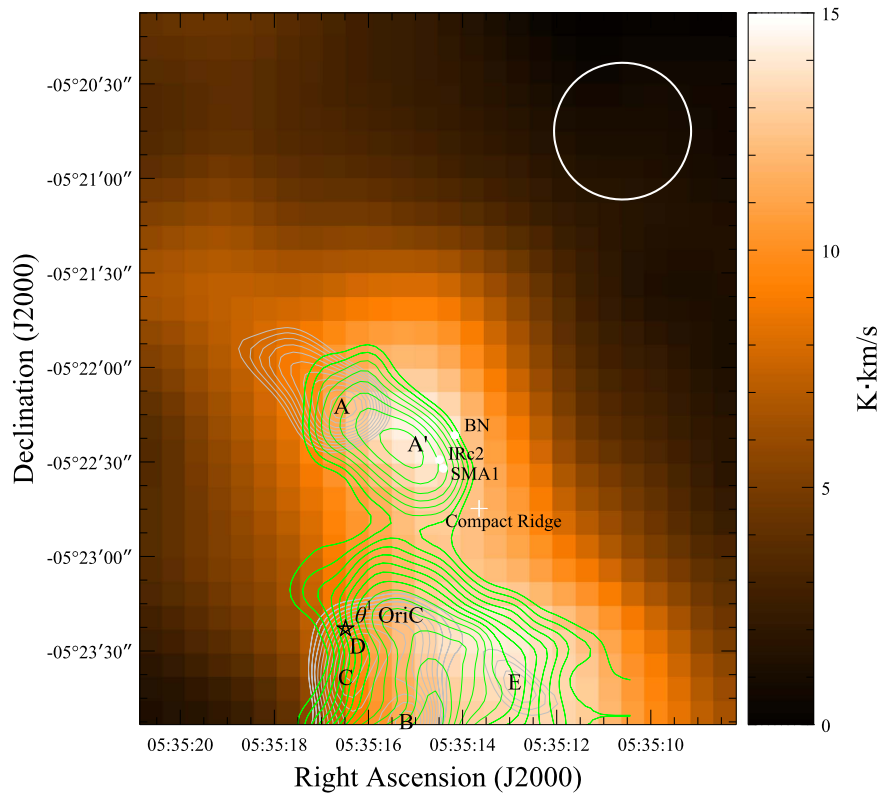


Figure 20. CH intensity integrated over the unblended $\Pi_{3/2} J = 3/2 - 1/2$ hyperfine line $F = 2^- - 1^+$. Blending of the other two hyperfine transitions occurs with SO_2 . Over the plotted range of intensities, the total integrated emission would scale by a factor of ≈ 1.6 for a theoretical 5:1:2 ratio for $F = 2 - 1 : 1 - 1 : 1 - 0$. Light gray contours indicate the upper 50% emitted power of C^+ 650–850 K km s^{-1} , green contours are of CH^+ $J = 1 - 0$ 20–40 K km s^{-1} . Labeled positions are the same as in Figure 3, with A' added to indicate a local intensity maximum; see also Table 5.

centered on SMA 1 near the 835 GHz thermal continuum peak, and at the Compact Ridge. These locations each have their own distinctive kinematic features within a single HIFI beam (e.g., Wang et al. 2011; see also Figure 2, and Persson et al. 2007 for a summary of the velocity features within $1'$ of IRc 2). Two velocity components are easily detected in each spectrum shown in the top panel, and in profile decompositions at the two positions shown in the middle and lower panels of Figure 23. The fits are derived using Gaussian profiles that are initially constrained only by the velocity at the observed emission peak; the center frequency, width, and intensity of the profile are treated as free parameters using a Levenberg–Marquardt fitting engine to minimize χ^2 between the observed and modeled spectra. A best-fit model derived from the average spectrum is then supplied as an initial guess for subsequent fitting at each map point. The fit results yield two ranges of LSR velocities and widths, $v_{\text{LSR}}(\text{broad}) = 6.5\text{--}8.5 \text{ km s}^{-1}$, $\Delta v(\text{broad}) = 7.5\text{--}14.5 \text{ km s}^{-1}$, and $v_{\text{LSR}}(\text{narrow}) = 7.3\text{--}8.2 \text{ km s}^{-1}$, $\Delta v(\text{narrow}) = 1.5\text{--}2.7 \text{ km s}^{-1}$.

The velocities and widths of the two distinctive kinematic components of the methanol line map are generally consistent with their first detection in the earliest methanol observations by Menten et al. (1986) and Wilson et al. (1989), of a single transition of the 23 GHz $10 - 9 \text{ A}^-$ band. The present results are also consistent with HIFI observations of the $\Delta J = 0$, $K = -4 \rightarrow -3$ and $K = 7 \rightarrow 6 \nu_t = 0$ Q-branch transitions at 524 and 1061 GHz by Wang et al. (2011), at a fixed position centered on the Hot Core. These distinct components were demonstrated by Wang et al. to probe gas at different temperatures.

Observations of several complex organic molecules with the Submillimeter Array (SMA) and the IRAM 30 m telescope over 220–230 GHz by Feng et al. (2015) also show a similar LSR velocity range across numerous detected methanol lines. At the higher angular resolution of the interferometric data, $\approx 3''$, emission peaks are resolved around five narrow LSR velocity ranges centered at 3, 5, 8, 11, and $>12 \text{ km s}^{-1}$. Feng et al. quote that these lines are all broad, $\sim 5\text{--}7 \text{ km s}^{-1}$, apparently lacking the additional narrow $<3 \text{ km s}^{-1}$ component observed by Menten et al. (1986), Wilson et al. (1989), Wang et al. (2011), and in our data.

Concerning spatial distribution, Wang et al. (2011) associated the narrow component with signatures of the Compact Ridge, which is usually approximated as a spherical clump of molecular gas $5''\text{--}10''$ in diameter (an idea put forth by Blake et al. 1987), and externally heated to produce the relatively low velocity widths. Menten et al. (1986, 1988) had previously identified the narrow component with a larger region $\approx 25''$ in size, centered $5''\text{--}10''$ south of the Hot Core where the broad emission component peaks. The distributions resulting from our profile decomposition analysis are shown in Figure 24, where it is seen that the narrow component peaks $\sim 8''$ to the south of the broad emission center, and $12''$ east and north of the Compact Ridge. The broad and narrow emission regions are roughly the same size, $30''\text{--}35''$ ($\approx 0.08 \text{ pc}$) after correcting for the HIFI beam, somewhat more extended than observed in the radio-frequency transitions. This difference might be attributed to higher sensitivities in our combined mapping observations or to a difference in gas temperatures being probed by the different sets of transitions.

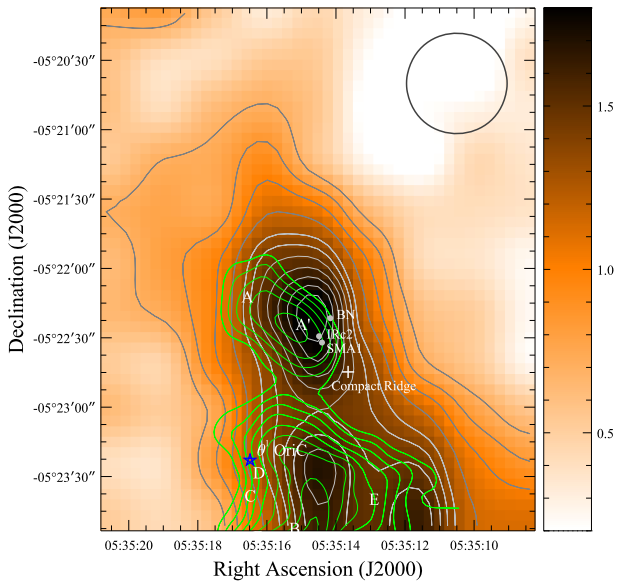


Figure 21. CH column densities at $T_{\text{rot}} = 35$ K in LTE. The calculation is based on measurements of the unblended $F = 2^- - 1^+$ triplet line, and scaled according to partition with the other two $\Pi_{3/2} J = 3/2 - 1/2$ hyperfine transitions. Gray contours follow the distribution of $N(\text{CH})$ column density at intervals of $0.1 \times 10^{14} \text{ cm}^{-2}$ and light gray contours indicate the 50% densest columns. Green contours show the 50% highest columns of $N(\text{CH}^+)$ at intervals of $0.15 \times 10^{13} \text{ cm}^{-2}$. Labeled positions are the same as in Figure 5.

In the SMA observations carried out by Feng et al. (2015), which indicate only a broad emission component, dual velocity-dependent emission peaks at the Hot Core and near the Compact Ridge (their “mm3a” and “mm3b” positions) are resolved. Feng et al. also point out emission to the south of the Compact Ridge, and newly discovered tails of emission extending toward the SE that they suggest are a part of the high-velocity outflow from the Hot Core, in part because one of their observed lines $8_{-1,8} \rightarrow 7_{0,7}$ is known to be a potential Class I maser that traces shocks. Neither feature is detected in our map of $K = 5 \leftrightarrow 4$ E-symmetry lines.

An excitation diagram analysis of the maps resulting from our Gaussian profile decompositions yields rotational temperatures and column densities of the isolated E-type transitions of the 834 GHz methanol band to probe conditions in the broad and narrow line components. Following a similar analysis with a starting point of LTE as carried out by Wang et al. (2011), the population diagram for the isolated 835 GHz lines observed toward the broad and narrow centers of emission and toward the Compact Ridge is shown in Figure 25; the total column density and excitation temperature at each position are given in Table 6.

Our derived excitation (rotation) temperatures are lower overall compared to those estimated by Wang et al. (2011) for the Hot Core, and by Feng et al. (2015) for the Hot Core and their position mm3a ($\sim 5''$ to the east of the Compact Ridge). T_{rot} increases if some of the methanol lines involved in the fitting are optically thick, as pointed out by Feng et al. from their spectral synthesis results. Uncertainties in our results may also be higher due to the smaller set of available lines, at least compared to Wang et al., who measured 33 total E-symmetry lines in the 524 and 1061 GHz bands in their HIFI observations of the Hot Core.

It can be noted that the lowest lying methanol transition is systemically offset to higher column densities (higher line

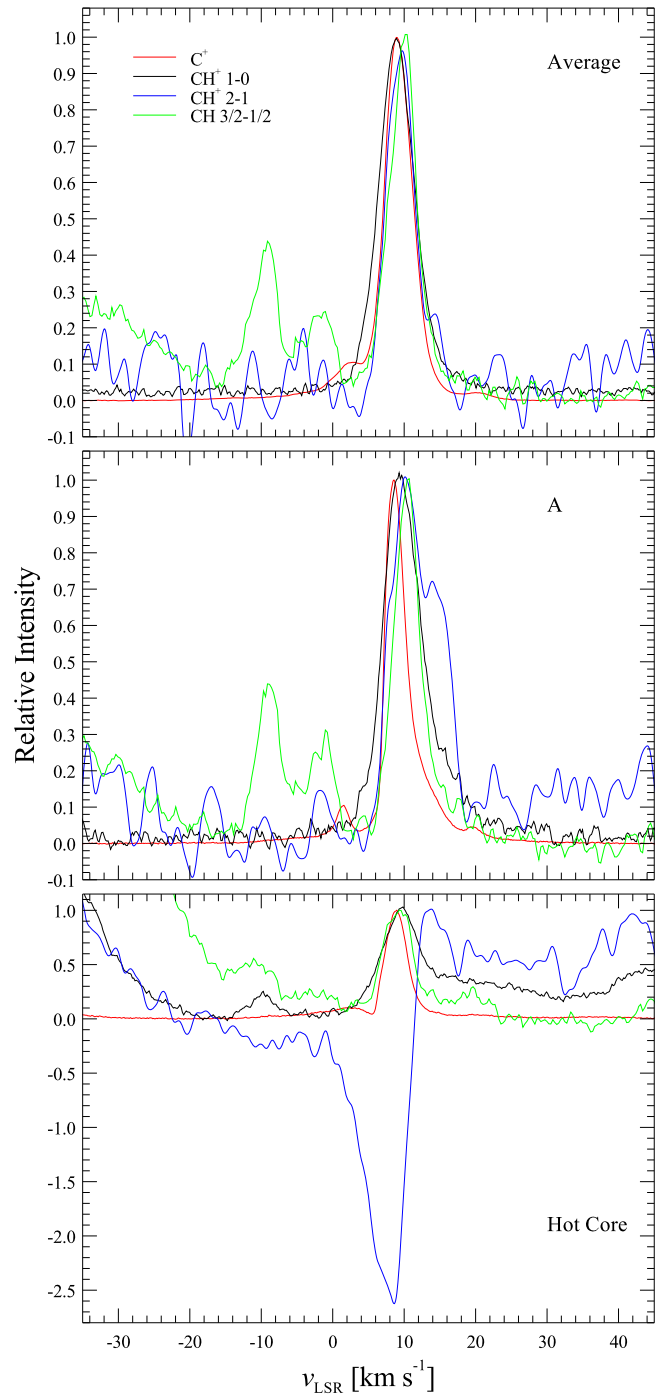


Figure 22. Comparison of the C^+ , $\text{CH}^+ J = 1-0$ and $2-1$, and $\text{CH}_2 \Pi_{3/2} - 2 \Pi_{1/2}$ profiles extracted from the Hot Core, Position A, and averages as labeled, on a normalized intensity scale. The LSR velocity for CH is based on the $F = 1^+ - 2^-$ line.

intensities) at all positions where emission is detected—an effect that can be seen in data presented by Wang et al. and Feng et al. as well, but it influences our slopes more strongly due to our smaller set of lines involved in the fitting. This behavior of the level population could be explained by optical pumping by thermal emission from the Hot Core of either the torsional state or the rotational R-branch of much colder gas. These Q-branch transitions mostly trace warmer gas, but for the lowest $J = K$ line there is also an optically pumped cold component, which is a non-LTE condition leading to deviation

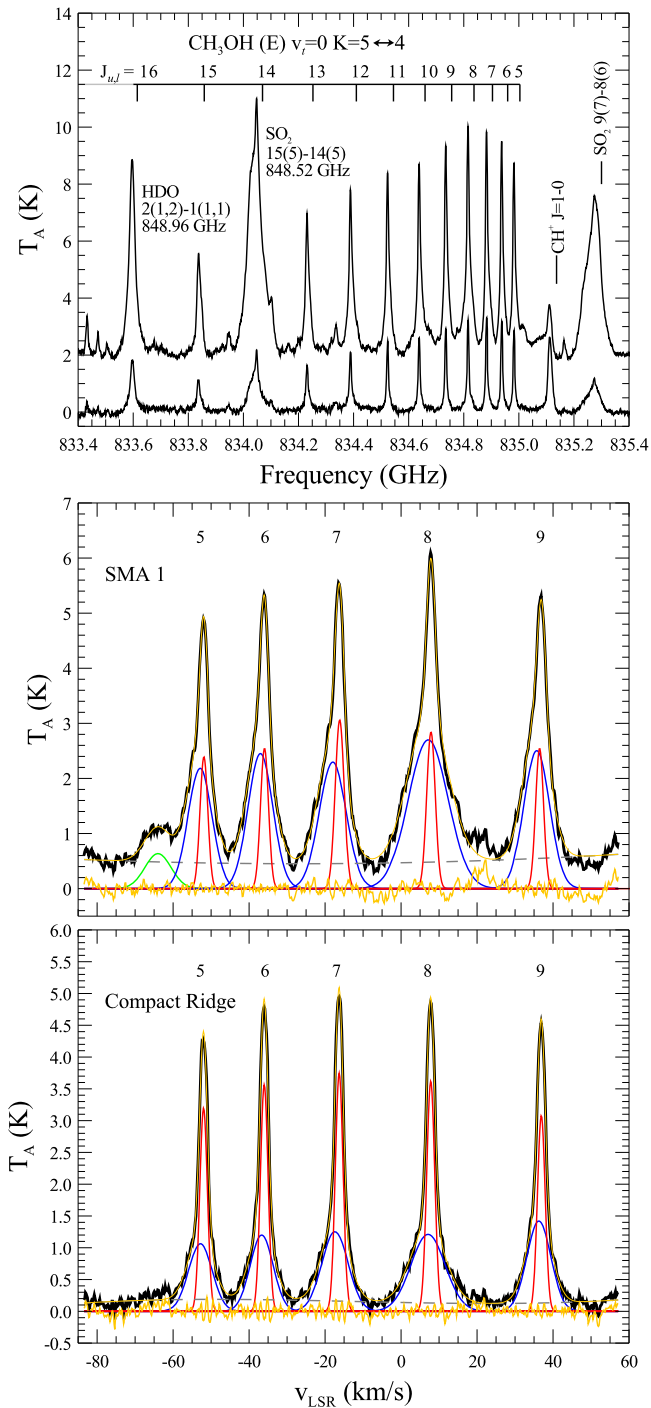


Figure 23. Continuum-subtracted spectra of CH^+ $J = 1 - 0$ and methanol observed toward SMA 1 and the Compact Ridge. In the top panel on a frequency scale in GHz, the SMA 1 spectrum is offset by +2.0 K for clarity. The SO_2 and HDO transitions labeled with frequencies outside the plotted range are from the opposite sideband. The middle and lower panels are on a v_{LSR} scale in km s^{-1} , referenced to the strongest $J_{u,l} = 8$ transition. Gaussian profile fits are shown for the first five E-branch methanol transitions, indicated by narrow (red) and broad (blue) components; the total model fits and residual fluxes are shown in orange. The component in green in the fit to the SMA 1 spectrum is included to improve the overall fit.

from linearity of the population diagrams. Nonlinearity is difficult to discern in Figure 25 (first- and second-order fits have equal rms of the residuals). If we exclude the $J_{5,5}$ line from fitting, T_{rot} would increase by 10–15 K, i.e., closer but still somewhat low compared to Wang et al.

With a larger set of observed transitions, curvature in the population diagram for the narrow velocity component has been discerned by Wang et al. (2011). They calculated a model spectrum that gives a reasonably good match to the observed spectrum by approximating the emitting material as being confined to a clump of gas $7''.5$ in diameter and externally heated, using a temperature profile with constant 30 K for $r < 5''.0$, $T \sim r^{3.8}$ for $r > 5''.0$, and constant methanol abundances of 3×10^{-6} and 3×10^{-7} , corresponding to column densities of $9.5 \times 10^{18} \text{ cm}^{-2}$ and $9.5 \times 10^{17} \text{ cm}^{-2}$ in the inner and outer parts of the clump, respectively. This gives a temperature of 120 K on the clump surface. The column densities we estimate for the Hot Core are comparable to those of Wang et al. in the outer part of their modeled clump but a factor of ~ 20 low at the inner radius. Feng et al. (2015) show that the emission is quite a bit more extended in some transitions in the 220–230 GHz range, leading (geometrically) to lower column densities.

In summary, the 835 GHz methanol band in our mapping data indicates spatially extended and overlapping broad and narrow line components in each transition that trace different gas kinematics and temperatures, coinciding with the Hot Core (near SMA 1) and a center of emission $9''$ to the south, respectively. The southern emission peak is offset to the east of the Compact Ridge to a position that is consistent with the mm3a/b peak positions identified in SMA observations of methanol and other complex organic molecules by Feng et al. (2015), resolving the Hot Core and Compact Ridge centers of emission into dual v_{LSR} -dependent peaks. The kinematics are clearly distinct from those of the CH^+ and CH emission, which trace more quiescent gas and probe different physical and chemical conditions outside the BN/KL outflow. Our calculated methanol column densities and rotation temperatures are somewhat low compared to those derived by Wang et al. (2011), but (a) optical depth corrections may be needed for certain submillimeter lines that could invalidate the assumption of a single temperature for the emission, and (b) their results depend on an approximation of the emitting region as a clump of gas $\sim 7''.5$ in diameter, which appears too confined compared to our HIFI mapping and recent SMA observations by Feng et al.

4. DISCUSSION

The principal focus of this paper is on the endothermic formation of the CH^+ ion and its excitation in Orion KL. In the diffuse ISM, CH^+ has column densities in the range from 10^{12} to a few times 10^{13} cm^{-2} (e.g., Black et al. 1975). The columns around Orion KL traced by line emission are about an order of magnitude higher, and $I_{\text{em}}(J = 1-0)/I_{\text{em}}(J = 2-1)$, where I_{em} is the integrated line intensity, is everywhere > 1 , pointing to lines that are not optically thick and not formed in a region where turbulent dissipation is the main gas heating mechanism driving the CH^+ formation. Characterization of the emission in the Orion Bar by Nagy et al. (2013) and Orion BN/KL (this study, Sections 3.4.4 and 3.4.3) points entirely to PDR characteristics. In fact, the kinematic properties and $I_{\text{em}}(n_{\text{upper}})/I_{\text{em}}(n_{\text{upper}} + 1)$ line ratios are very similar between the two regions, and we can conclude that the same material extending around these OMC 1 features is responsible for the CH^+ emission. We can similarly conclude, based on our models, that electron collisions affect the excitation of CH^+

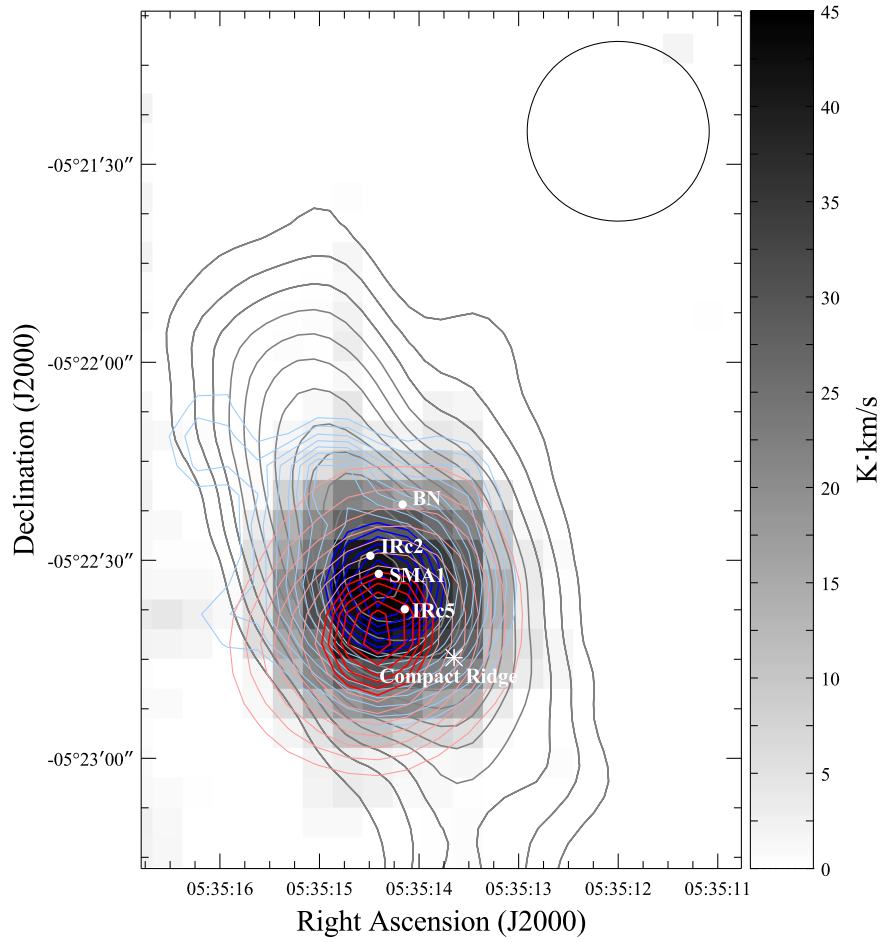


Figure 24. Average intensity in reverse grayscale of the $\text{CH}_3\text{OH } K = 5 \leftrightarrow 4, v_t = 0$ E-branch transitions between $J_{u,l}$ 5 and 15 (excluding 14 due to blending with SO_2), integrated over v_{LSR} between -7 and $+25 \text{ km s}^{-1}$ for each line. Overlaid 835 GHz continuum contours in gray are the same as in Figure 3. Blue and red contours are integrated intensities of the fitted broad and narrow components, respectively, at each position as shown for the explosive outflow and Compact Ridge spectra in Figure 23. Broad (narrow) component contours in light blue (red) are on a linear scale between 3 and 11 km s^{-1} ($0.5\text{--}1.9 \text{ km s}^{-1}$) at 1 km s^{-1} (0.5 km s^{-1}) intervals, and in dark blue between 11.5 and 15.5 km s^{-1} ($2\text{--}2.5 \text{ km s}^{-1}$) at 1 km s^{-1} (0.5 km s^{-1}) intervals. The angular separation between positions of peak broad and narrow component emission is $8''.5$. The $27''.5$ HPBW of HIFI at 835 GHz is indicated.

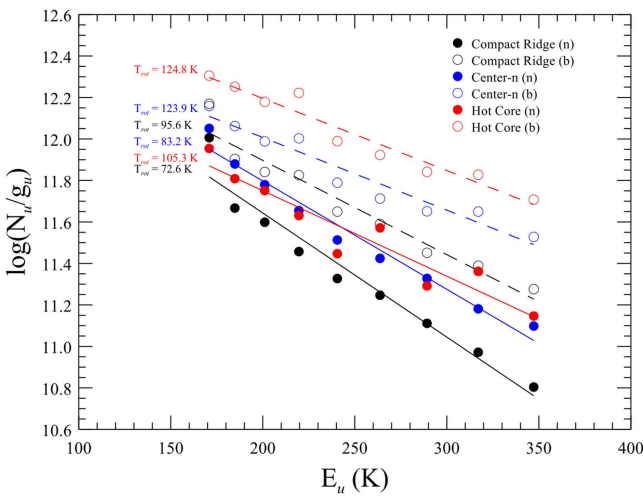


Figure 25. Population diagram of the $\text{CH}_3\text{OH } 835 \text{ GHz}$ band for nine of 12 detected transitions, $J_{u,l}$ 5 through 13, at labeled positions. LTE is assumed for the linearly fitted excitation temperatures and column densities (see Table 6) of the narrow line (n) and broad line (b) emission components.

Table 6
 $\text{CH}_3\text{OH } 835 \text{ GHz}$ Excitation Temperature and Column Density

Position	T_{ex} (K)		N (10^{17} cm^{-2})	
	b	n	b	n
SMA 1/Hot Core	125	105	7.8	3.8
Center-n	124	83	5.1	6.9
Compact Ridge	96	73	6.4	6.9

Note. Positions correspond in Figure 24 to labeled sources, where “Center-n” refers to the center of narrow-line emission. Columns “b” and “n” are for the broad and narrow line components.

and that reactive collisions also need to be taken into account in the calculations.

The models show that CH^+ is a tracer of the warm surface region ($A_V < 0.6 \text{ mag}$) of the PDR with kinetic temperatures between 500 and 1000 K, and excitation temperatures of 23 K but possibly as low as 10 K in the absorbing cloud of gas in front of the Hot Core. At velocity widths of $\sim 5 \text{ km s}^{-1}$, the

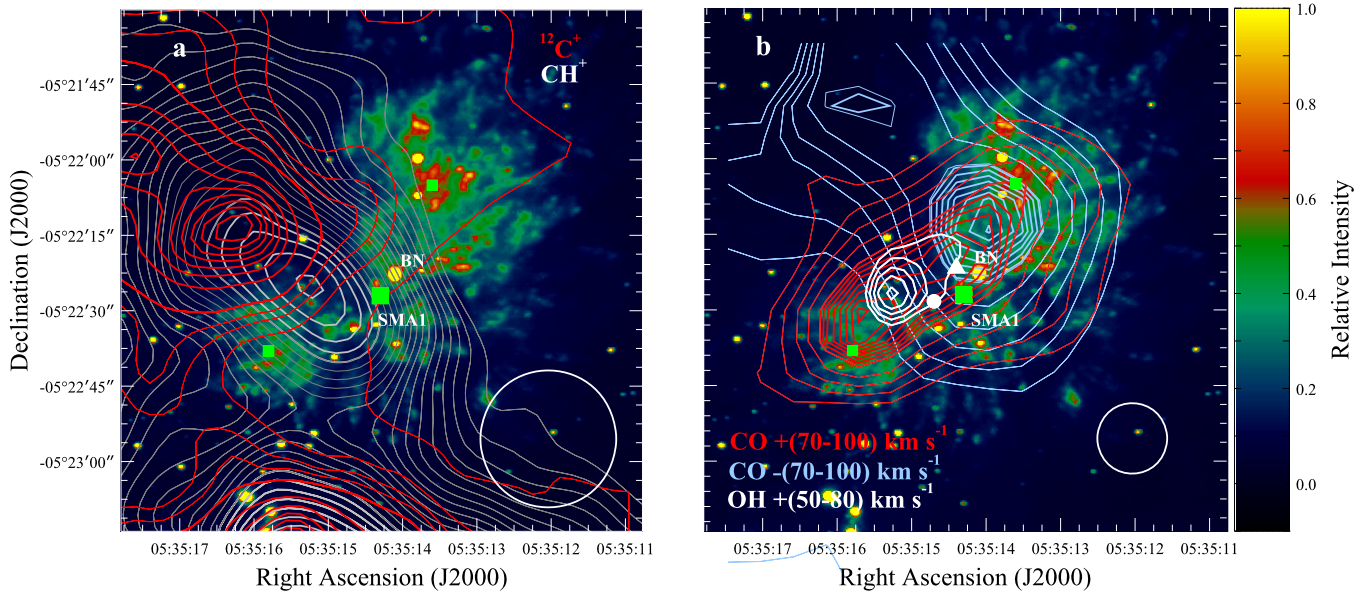


Figure 26. The energetic BN/KL outflow imaged in the $\text{H}_2 S(1) 2.12 \mu\text{m}$ filter with the Near-Infrared Camera and Fabry–Perot Spectrometer on the ARC 3.5 m telescope at the Apache Point Observatory in 2004 December, published by Cunningham (2006) and Bally et al. (2011), compared with: (a) contours of CH^+ (white and gray) and C^+ (red); (b) $\text{CO } J = 10-9$ (blue and red) and OH 1837 GHz triplet transitions between $^2\Pi_{1/2} J = 1/2$ states (white). Thick contours represent the upper 60% of radiated power, thin lines correspond to the 30%–60% power range, and all are on intensity scales normalized to peak integrated emission at intervals of 5% relative flux. The C^+ contours are for emission at the system velocity of 9.7 km s^{-1} . The red- and blueshifted emission from CO integrated between $\pm(70-100) \text{ km s}^{-1}$ (offset by -9.7 km s^{-1} for the mean system v_{LSR}) is indicated by corresponding colored contours. The white filled triangle indicates the peak location of total integrated CO $J = 10-9$ emission. White contours indicate OH redshifted emission, integrated over $+(50-80) \text{ km s}^{-1}$. Blueshifted OH could not be measured due to confusion with CO $J = 13-12$ from the image sideband of the HIFI observations. The filled white circle indicates the peak of OH emission integrated over -10 to $+80 \text{ km s}^{-1}$. In both panels, the filled large and small green squares indicate the center of the explosion and H_2 emission peaks, respectively (e.g., Peng et al. 2012b). The HIFI beam sizes at 835 and 1840 GHz are shown in panels (a) and (b), respectively.

CH^+ emission is broader than the average line width of other molecules and C^+ observed in the Orion Bar (Nagy et al. 2013). It is clear from the models that the extended CH^+ gas is dense and under comparably high pressures (in the range of $1-2 \times 10^8 \text{ cm}^{-3} \text{ K}$) in both regions.

The kinematics of the C^+ emission in the area of $\sim 11 \text{ arcmin}^2$ around Orion KL are considerably more complex than in the Orion Bar. In our mapped region, the two strongest C^+ components probe a range of A_V up to around 3 mag. The two components have velocity widths of $2-3 \text{ km s}^{-1}$ and $3.7-6.6 \text{ km s}^{-1}$ and are highly variable in their relative intensities (see Figure 4), indicating large variations in optical depth of these regions, somewhat wider than calculated for the Orion Bar by Ossenkopf et al. (2013). Measurements of $^{13}\text{C}^+$ at selected peaks of C^+ intensity around Orion BN/KL indicate a range for $\tau(^{12}\text{C}^+)$ of 1.4–2.6 outside the Hot Core, and from 4 to 6 toward the Hot Core.

Röllig & Ossenkopf (2013) have shown that isotopic fractionation can be significant for C^+ , C, and CH^+ in PDRs with high densities in moderate radiation fields. It requires a significant amount of ionized carbon at temperatures of the order of the barrier of the isotope-selective reaction of 35 K. Most gas in Orion BN/KL is, however, much hotter (see Figure 9) so that no measurable C^+ fractionation is expected, in agreement with our results from Section 3.3.2 and those of Ossenkopf et al. (2013) for the Orion Bar. Moreover, the chemical models show that CH^+ only partially inherits the isotopic fractionation from C^+ , so that a noticeable isotopic fractionation in CH^+ occurs only at column densities well below the detectable level (Figure 16 from Röllig & Ossenkopf 2013). Hence, both model computations and our $^{13}\text{C}^+$

measurements indicate that the isotopic ratio in CH^+ follows the elemental abundance ratio of $^{12}\text{C}/^{13}\text{C} \approx 67$.

While we could successfully characterize the physical conditions leading to the formation and excitation of CH^+ around Orion BN/KL in the framework of a PDR, with parameters describing physical and chemical properties similar to those of the Orion Bar, the reservoir of vibrationally excited H_2 needed to react with C^+ is not the most observationally evident source—namely in H_2 tracing shocked gas from the energetic BN/KL outflow. Figure 26(a) shows $\text{H}_2 2.122 \mu\text{m } 1-0 S(1)$ tracing the BN/KL outflow in observations published by Cunningham (2006) and Bally et al. (2011), with contour overlays of our $\text{CH}^+ J = 1-0$ and C^+ observations on a relative intensity scale. The origin of the outflow is attributed to a recent ($\sim 500-1000$ years) stellar merger associated with the IRc 2 source or the dynamical decay of a non-hierarchical multiple system, with velocities in the range $10-30 \text{ km s}^{-1}$. Neither the distribution nor kinematics of these features traced in H_2 are consistent with our CH^+ mapping data, nor can we identify a comparable morphology of C^+ in any observed velocity channel. The C^+ contours in Figure 26(a) are from the $+9.7 \text{ km s}^{-1}$ velocity channel, and it might be tempting to suggest some boundary interactions particularly in the outflows on the eastern side where the strongest C^+ emission is indicated. However, this may be purely coincidental structure of the C^+ gas, and we detect no CH^+ emission in this velocity range, particularly in the region not affected by the confusion from the strong SO_2 and CH_3OH emission lines from the dense Hot Core.

Moreover, spectral observations do not indicate formation being traced in the shocked gas, because the profiles of CH^+ and CH show no significant broadening or Doppler-shifted

emission associated with shocks and outflows. This is consistent with the lack of a correlation between CH^+ and the shock-excited $\text{H}_2(\nu = 1)$ (Figure 4). These observations do not rule out interactions or shock chemistry involving C^+ in the outflow; it is simply that we cannot detect such interactions through the gas in which the outflow is embedded, indicating that the chemistry that dominates this region is from UV irradiation. These points lead us to conclude that the relatively quiescent CH^+ gas cloud envelops OMC 1 and traces the warm surface regions of molecular clumps of gas over an extended region, from Orion North to the Orion Bar, at the system velocity of the nebula of $8\text{--}10\text{ km s}^{-1}$, but is not physically associated with the outflow source of higher-velocity vibrationally excited H_2 to a level that we can detect with HIFI.

Pumping by UV irradiation and chemical formation can supply the vibrationally excited H_2 required for efficient CH^+ formation, and evidence favors UV irradiation as a source of vibrationally excited H_2 in the regions of the nebula where CH^+ is observed. A significant fraction of the CH^+ emission in the Orion nebula probably arises in photon-dominated gas of modest density ($n_{\text{H}} \sim 10^4\text{ cm}^{-3}$) that is not prominent in the vibrational lines, but still contains sufficient vibrationally excited H_2 to efficiently form CH^+ . Where the vibrational lines are measured, they can be used to assess the gas properties. Emission from the $\nu = 1\text{--}0$ and $\nu = 2\text{--}1\text{ S}(1)$ ro-vibrational lines of H_2 near $2\text{ }\mu\text{m}$ has been detected in the Orion Bar PDR and OMC 1 (Beckwith et al. 1978; van der Werf et al. 1996). As discussed by Sternberg & Dalgarno (1989), the intensity ratio r_{21} ($\equiv I_{10}/I_{21}$) of the two lines depends on the UV flux (χ) as well as on the gas density (n_{H}). In the Orion Bar, r_{21} has been found to range from a low value (3.4 ± 1.9)—attributed to purely radiative fluorescence of H_2 from relatively low-density ($n_{\text{H}} \leq 10^4\text{ cm}^{-3}$) gas of the so-called “interclump medium” (far from the ionization front illuminated by the intense UV flux of the Trapezium stars)—to a high value (8.1 ± 0.7)—attributed to thermal H_2 line emission in warm dense ($T \sim 2000\text{ K}$, $n_{\text{H}} \geq 10^5\text{ cm}^{-3}$) molecular gas heated by intense UV radiation (van der Werf et al. 1996). Similarly large values of r_{21} have been reported for Orion BN/KL (~ 10 ; Beckwith et al. 1978) over a region that overlaps with much of the region mapped in the present study. As demonstrated by Sternberg & Dalgarno (1989), while a large r_{21} (≥ 10) is usually attributed to shock-heating, it does not prove the presence of shock waves, particularly in the vicinity of strong ultraviolet sources, because H_2 line emission produced by shock-heating of the gas may be quite difficult to distinguish from similar thermal H_2 line emission from quiescent dense gas heated by UV photons. The overall lack of correspondence in the observed CH^+ and shock-excited H_2 distribution (Figure 26(a)), and the similarity of PDR model parameters that reproduce the CH^+ line intensities in Orion BN/KL with those of the Orion Bar (Figure 16), support this view, and are strongly suggestive of the principal role of UV irradiation in the production of CH^+ in Orion BN/KL.

Further support for UV-driven rather than shock-driven production of CH^+ is provided by a straightforward estimate of the production timescales of CH^+ , which takes into account all formation and destruction processes of CH^+ . For example, obtaining $n(\text{CH}^+) = 1.86 \times 10^{-2}\text{ cm}^{-3}$ at $0.3 A_{\text{V}}$ and at a net production rate of $1.2 \times 10^{-11}\text{ cm}^{-3}\text{ s}^{-1}$ (at $T = 800\text{ K}$; see Figure 17) requires approximately 49 years—more than an

order of magnitude shorter than the dynamical age of $500\text{--}1000$ years estimated for BN/KL outflow. Thus, it seems far more likely that the CH^+ abundance is maintained by a steady-state UV-driven PDR chemistry than by shocks. Undoubtedly, the effect of shocks as well as UV must be considered to explain the molecular emission and abundances in Orion BN/KL and similar regions, but a quantitative evaluation of the relative contributions of shocks and UV to the production and excitation of H_2 and other molecules requires sophisticated models combining UV and shock excitation, which are still quite uncertain (e.g., Kristensen et al. 2008; Visser et al. 2012) and are beyond the scope of the present work.

The timescale argument that supports our observations and modeling of the CH^+ as arising in the diffuse gas with a UV-driven chemistry does not explain why, on the contrary, no CH^+ is observed in the outflow, where excited H_2 is abundant. This is possibly due in part to differences in the degree of excitation in the two environments. While C^+ coexists with H_2 in multiple vibrationally excited levels in PDRs where fluorescence populates the higher levels, propensity rules suggest that the H_2 goes mostly to the lowest vibrational level in shocks, i.e., H_2 is thermalized at $\nu = 1$. This provides the required energy for C^+ to react with the H_2 , but leaves little additional energy for the CH^+ to be hot enough to emit, in contrast with the average amount of vibrational heating of $\approx 9920\text{ K}$ available for all 15 vibrational levels of H_2 (Röllig et al. 2006; Nagy et al. 2013), some 5300 K above the activation barrier.

We should nonetheless expect some CH^+ emission where both $\text{H}_2(\nu = 1)$ and C^+ are abundant in a shocked environment, such as observed in the DR 21 outflow (Falgarone et al. 2010). Hence the apparent lack of a correlation of C^+ at any velocity with the H_2 outflow provides another clue for the absence of CH^+ there. A plausible mechanism for C^+ depletion in the outflow is in one of the CO production pathways. In a standard gas-phase chemistry (e.g., Liszt et al. 2005, p. 187), CO is formed by first producing CO^+ , via $\text{C}^+ + \text{OH} \rightarrow \text{CO}^+ + \text{H}$, followed by either $\text{CO}^+ + \text{H} \rightarrow \text{CO} + \text{H}$, or $\text{CO}^+ + \text{H}_2 \rightarrow \text{HCO}^+ + \text{H}$ and $\text{HCO}^+ + e \rightarrow \text{CO} + \text{H}$. Orion BN/KL is known to be abundant in the products of these reactions, which all proceed relatively fast. Furthermore, high-velocity ($\sim 70\text{--}100\text{ km s}^{-1}$) CO from low to very high J levels is observed to correlate well with each of the $\text{H}_2(\nu = 1)$ outflow peaks (Zapata et al. 2010; Peng et al. 2012b; Goicoechea et al. 2015a). For contrast with the distributions of CH^+ and C^+ in relation to the outflow in Figure 26(a), we also show contours of CO ($J = 10\text{--}9$) and OH (1834 GHz triplet) observed with HIFI in Figure 26(b), overlaid onto the H_2 $2.12\text{ }\mu\text{m}$ imaging. The CO was integrated between $\pm(70\text{--}100)\text{ km s}^{-1}$, where blue- and redshifted emission contours are correspondingly color-coded. The OH redshifted emission was integrated over $+(50\text{--}80)\text{ km s}^{-1}$; blueshifted emission could not be measured due to substantial blending with CO $J = 13\text{--}12$ emission occurring in the opposite sideband. The distribution of this material agrees well with the previous published results on the fast-moving CO in relation to the H_2 fingers, indicating that they are dynamically coupled (e.g., Peng et al. 2012b). Hence C^+ in the outflow may be chiefly consumed in the production of CO, with higher efficiency than the reaction with $\text{H}_2(\nu = 1)$. This hypothesis

needs to be tested with further modeling that incorporates shock chemistry to account for absent or suppressed CH^+ emission from the outflow (see Section 6).

5. SUMMARY AND CONCLUSIONS

We have presented high S/N velocity-resolved spectral mapping observations of $^{12}\text{C}^+$, $^{13}\text{C}^+$, CH^+ rotational transitions, CH Λ -doubling transitions, and CH_3OH torsional lines for the purposes of characterizing their distributions and kinematic properties around the dynamic Orion BN/KL SFR, and have focused on the formation and excitation of the CH^+ ion.

1. The C^+ observations reveal a complex ionized cloud structure of a PDR surrounding BN/KL, with multiple LSR velocity components between -15 and $+20 \text{ km s}^{-1}$ following distinct spatial distributions. The two principal emission components show narrow ($2\text{--}3 \text{ km s}^{-1}$) and broad ($4\text{--}7 \text{ km s}^{-1}$) velocity widths that we interpret as tracing (respectively) higher density material and the lower density interclump medium. Significant variation of the relative strength of each velocity component indicates a corresponding spread in optical depth conditions in the nebula. The average column density and optical depth of $^{12}\text{C}^+$ outside the Hot Core region are comparable to those of the Orion Bar peak reported by Ossenkopf et al. (2013), but at the emission peaks around Orion BN/KL the values of $N(\text{C}^+)$ and τ_{12} are factors of 2 and 3 higher than for the Orion Bar. Excitation temperatures of $200\text{--}300 \text{ K}$ also tend to be higher. The average $\langle T_{\text{ex}} \rangle$ of the C^+ -emitting gas outside the Hot Core is almost a factor of 2 higher than the average for OMC 1 estimated by Goicoechea et al. (2015b).
2. Absorption of background continuum radiation from heated dust peaking at the Hot Core source SMA 1 is observed in the $\text{CH}^+ J = 2\text{--}1$ transition, and in C^+ by decomposition of the composite profile. No absorption by the $\text{CH}^+ J = 1\text{--}0$ line in the 850 GHz continuum is detected (but weak absorption is not ruled out), setting limits of $T_{\text{ex}}(\text{CH}^+) = 10\text{--}25 \text{ K}$ in the absorbing gas. The CH^+ emission material has a similar (low) excitation temperature. The gas with C^+ in absorption similarly has $T_{\text{ex}}(\text{C}^+) < 28 \text{ K}$, but has greater optical depths than CH^+ , while $\langle T_{\text{ex}}(\text{C}^+) \rangle \simeq 175 \text{ K}$ for the emitting gas.
3. On average the kinematics of the C^+ gas around Orion BN/KL are consistent with earlier large-beam observations of Orion A (Balick et al. 1974), which is in turn similar to observations of the CH^+ absorption line of OMC-2 FIR4 and led López-Sepulcre et al. (2013) to conclude that this northern cloud region is an extension of the C^+ interface between Orion BN/KL and the Trapezium. On the finer spatial scale of our HIFI maps of this region, the C^+ , CH^+ , and CH emission profiles share similar LSR velocities, but with distinct differences in kinematic complexity—the CH and CH^+ gas is more quiescent, exhibiting much lower variations in LSR velocities and line broadening. All CH and CH^+ lines can be fit with a single Gaussian profile at most positions, with average widths $\langle \Delta v \rangle \simeq 5.3 \pm 0.6 \text{ km s}^{-1}$.
4. The distribution of CH^+ is similar to that of the main emission component of C^+ , but there is a tendency for CH^+ emission to be strongest where intensity gradients in

- C^+ are highest. At all locations, the measured v_{LSR} of CH^+ at peak line center is redshifted by $\approx +2 \text{ km s}^{-1}$ relative to the main C^+ emission feature. The distribution of C^+ over the range of CH^+ velocity channels is the same. Secondary kinematic structures of C^+ (outside the range of $+6.0$ to $+10.0 \text{ km s}^{-1}$) do not have any spatial CH^+ correspondences. A weak redshifted and broader ($\Delta v \approx 12 \text{ km s}^{-1}$) secondary component to the CH^+ profile is detected at the brightest peaks nearest to the Hot Core and toward the Hot Core itself, at $v_{\text{LSR}} \approx 13 \text{ km s}^{-1}$.
5. Measurements of $^{13}\text{C}^+$ hyperfine lines and the total $^{12}\text{C}^+$ emission at several positions of peak intensity yield τ ($^{12}\text{C}^+$) in the range 1.4–2.6 along lines of sight of strong integrated emission, and up to 6.2 toward the Hot Core. The estimates are based on assuming a constant $^{12}\text{C}/^{13}\text{C}$ abundance ratio of 67 ± 10 and our estimates $T_{\text{ex}}(\text{C}^+) = 200\text{--}300 \text{ K}$ outside the Hot Core and $\approx 120 \text{ K}$ in the Hot Core region. Our approach and results support conclusions for the Orion Bar PDR by Ossenkopf et al. (2013) that chemical fractionation of carbon does not play a detectable role in influencing the isotopic balance.
 6. CH^+ line intensities can be reproduced by PDR and non-LTE radiative transfer models, without the need to introduce shock models for the high activation barrier of CH^+ to be overcome in the reaction between C^+ and vibrationally excited H_2 . Our conclusion is that PDR conditions describing the Orion Bar in which electron collisions affect the excitation of CH^+ , requiring also the inclusion of reactive collisions, are similar in Orion BN/KL. Unlike the Orion Bar, however, the strong continuum emission from KL causes the CH^+ excitation temperatures to increase by factors of 1.2–2.9, while integrated intensities decrease for the three lowest transitions by factors of 1.5–1.0, and decrease by 8%–21% for the $J = 4\text{--}3$ and $J = 5\text{--}4$ transitions.
 7. The line shapes and excitation of CH Λ -doubling lines in the $^2\Pi_{3/2}$ and $^2\Pi_{1/2}$ states can be modeled well using a one-component model with an excitation temperature of $\sim 35 \text{ K}$. The CH abundance relative to H_2 appears to agree with the relationship of Sheffer et al. (2008), and does not seem to decline as suggested by Polehampton et al. (2005). We conclude that the CH originates in gas where the density is a few times 10^6 cm^{-3} , is not in thermal equilibrium, and is concentrated in the $^2\Pi_{1/2} J = 1/2$ and $^2\Pi_{3/2} J = 3/2$ levels. The population of the $^2\Pi_{1/2} J = 3/2$ and $^2\Pi_{3/2} J = 5/2$ levels is dominated by absorption of the continuum. However, the 1661 GHz transition, observed only toward the BN/KL complex, is in the emission wing of the $2_{2,1}\text{--}2_{1,2}$ water line ($E_u = 194 \text{ K}$), making the analysis more uncertain. Assuming that the continuum level is set by the water wing, the absorption is less deep than would be expected, implying that the absorption and emission originate at least in part from the same gas, similar to our conclusions for the absorbing and emitting CH^+ gas toward the BN/KL complex.
 8. Similar distributions and line ratios of CH and CH^+ explained by special geometry (face-on or clumpy) suggest that whatever the amount of CH^+ synthesized via non-equilibrium processes in these lines of sight, an

amount of CH that is a constant fraction of the amount of CH^+ is also formed. If this result were true in general, then we would expect some minimum amount of CH to be present whenever CH^+ is detected. Analyses like those presented here, but for other SFR lines of sight, are needed to assess how narrow a range in $N(\text{CH})/N(\text{CH}^+)$ (which is less than unity in Orion BN/KL) is generally present in the region of CH^+ synthesis.

9. We showed that the spatial morphology of the prominent BN/KL outflow traced by shock-excited H_2 does not correlate well with the observed distribution of CH^+ . Our excitation and PDR modeling demonstrates that UV irradiation plays the critical role of providing a distributed reservoir of H_2 to react with C^+ in the extended PDR to produce CH^+ . This is supported by earlier observations of $\nu = 1-0$ and $2-1$ $S(1)$ ro-vibrational lines of H_2 in thermal emission close to the Trapezium stars and in fluorescence further away. Timescales to reach equilibrium production of CH^+ are at least an order of magnitude shorter than the dynamical age of the outflow. Hence, as indicated by homogeneous line profiles across the region, production of CH^+ is more likely to be maintained by a steady-state UV-driven PDR chemistry rather than by a shock chemistry due to the large disparities between the production rate needed to reach observed abundances and the approximate age of the Orion BN/KL outflow. Furthermore, C^+ does not correlate well at any observed velocity with the shock-excited H_2 features, indicating that a shock chemistry involving C^+ may be competing with, or inhibiting, production of CH^+ . We suggest that C^+ is most likely being consumed in the production of CO, which is observed to have high-velocity wings with a spatial distribution that is consistent with the outflow, in reactions involving OH, CO^+ , HCO^+ , and H_2 . Radiative association between C^+ and H_2 to form CH is not favored, due to the same lack of spatial correspondence of observed CH as CH^+ with the outflow.
10. From our PDR models for this region C^+ is found to trace outer cloud boundary layers to depths of $A_V < 3$ mag, consistent with analysis of lower sensitivity mapping of C^+ over the larger OMC 1 region by Goicoechea et al. (2015b). In models by Goicoechea et al. the C^+ abundances peak about 1 mag deeper in A_V , a difference that is expected from the larger dust grain sizes built into their adopted extinction parameters. We also estimate higher C^+ excitation temperatures and optical depths for the inner 10 arcmin² around the BN source. Electron densities peak at similar depths as C^+ , giving the interesting result that CH abundances also peak as deeply into the clouds as C^+ , while the highly reactive CH^+ molecules trace the warmest layers only to $A_V < 0.6$ mag. Nonetheless it is clear that CH^+ is formed in the transition zone between the atomic and molecular gas. In this layer, H_2 is not optically thick to the UV field, and as a result, it is strongly excited through its electronic states. Due to the lack of an electronic dipole moment, H_2 is inefficient in cooling itself. The net result is highly excited H_2 , both rotationally and vibrationally.
11. CH_3OH transitions extracted toward SMA 1 and the Compact Ridge, tracing the densest molecular clouds to higher A_V in the dusty core region, exhibit two distinct

kinematic components at both locations. A broad set of lines with $\Delta v = 7.5\text{--}14.5$ km s⁻¹ dominates narrow $\Delta v = 1.5\text{--}2.7$ km s⁻¹ at SMA 1, and vice versa at the Compact Ridge. These kinematic results are generally consistent with previous investigations by Menten et al. (1986, 1988), Wilson et al. (1989), and Wang et al. (2011). The separate velocity components follow a distribution consistent with results by Wilson et al. (1989), but are indicated to be more extended in the submillimeter transitions than at 23 GHz (possibly due to higher sensitivities in the HIFI observations), which is generally more consistent with recent 220–230 GHz SMA observations by Feng et al. (2015). The excitation temperatures we have estimated are lower than the results of Wang et al. (2011) for the Hot Core, possibly indicating that level populations are not in statistical equilibrium or that a single excitation temperature is invalid in the population diagram analysis. Similarly, column densities are somewhat higher according to Wang et al., who approximated the emitting region as being confined to a gas clump of $7''.5$ diameter (compared to the regions of $\sim 30''$ diameter of narrow and broad emission in our maps).

The basic modeling we presented in Sections 3.4.3 and 3.4.4 captures the essential elements of the chemical and physical conditions in the regions of CH^+ and CH formation, but other processes such as shocks and intermittent turbulent dissipation may need to be included in a complete model of Orion KL. Observations do not indicate detectable levels of CH^+ that we can associate with shock chemistry, and the levels of intermittency required to reproduce the observed abundances through the dissipation of turbulence await elucidation by three-dimensional simulations (Godard et al. 2014). Even where shocks are known to be present, the importance of a UV-driven chemistry for CH^+ production should not be underestimated, especially in the case of actively star-forming galaxies where CH^+ has been detected, for example in Arp 220, NGC 253, and M83 where the $J = 1-0$ line is observed in absorption (Rangwala et al. 2011, 2014) and in Mrk 231 where it is in emission (van der Werf et al. 2010).

6. FUTURE WORK

In order to improve our understanding of the relative roles of UV and shock chemistries in Orion BN/KL with application to other SFRs, we can study other endothermic processes to test the consistency of our models. In particular the SH^+ ion shares a production pathway similar to that of CH^+ but with a factor of $\simeq 2$ higher energy barrier, $\text{S}^+ + \text{H}_2 \rightarrow \text{SH}^+ + \text{H}$ with $\Delta E = 9860$ K. This could be tested with detections of the rotational transitions of $\text{SH}^+ N_J = 1_2-0_1$ toward the bright CO peak in the Orion Bar by Nagy et al. (2013). SH^+ was not mapped across Orion BN/KL, but we can exploit HIFI spectral scans of the Hot Core and Compact Ridge (see Crockett et al. 2014) and observations of transitions accessible from the ground (e.g., Müller et al. 2014 observed the Orion Bar), which we are following up at the Atacama Pathfinder Experiment (APEX) telescope. CO^+ transitions provide another means to explore the production mechanisms of molecules in highly UV-irradiated environments. In addition, a test for the role of the radiative association between C^+ and H_2 involving the molecular ions CH_2^+ and CH_3^+ as intermediate products would

be their detection in any environment where CH^+ is abundant (see a first attempt by Indriolo et al. 2010). The CH_3^+ ion is particularly interesting and has ro-vibrational transitions that can be observed in the near IR from the ground. CF^+ is another interesting ion involving C^+ reactions with HF, and has low- J rotational transitions that have been observed from the ground toward the Orion Bar (Neufeld et al. 2006) and the Horsehead Nebula (Guzmán et al. 2012).

This work is based on observations made with the HIFI instrument on the *Herschel Space Observatory*, which was designed and built by a consortium of institutes and university departments from across Europe, Canada, and the United States (the National Aeronautics and Space Administration, NASA) under the leadership of the Netherlands Institute for Space Research (SRON), Groningen, The Netherlands, and with major contributions from Germany, France, and the US. We express our gratitude to Nathan Crockett for helpful discussions and providing the Orion BN/KL continuum data, and to John Bally and Nathan Cunningham for providing the H_2 observations of the BN/KL outflow. We also thank Octavio Roncero and Alexandre Zanchet for providing their CH^+ state-to-state formation rates, and we especially appreciate support with the Meudon PDR code from Frank Le Petit. We are grateful to the HIFI Instrument Control Center team for its many years of dedicated work and support. We also thank an anonymous referee for thorough review of the manuscript and thoughtful comments to improve its quality. Support for this work was provided by NASA (*Herschel* GT funding) through an award issued by JPL/Caltech. V.O. acknowledges support by the Deutsche Forschungsgemeinschaft (DFG) via the collaborative research grant SFB 956, project C1. E.F. and M.G. thank the CNES and the INSU program PCMI for funding. A part of this research was performed at the Jet Propulsion Laboratory, California Institute of Technology, under contract with NASA. H.G. acknowledges support from the National Science Foundation (NSF). Any opinions, findings, and conclusions in this article are those of the authors, and do not necessarily reflect the views of the NSF.

REFERENCES

- Abel, N. P., Ferland, G. J., O'Dell, C. R., Shaw, G., & Troland, T. H. 2006, *ApJ*, 644, 344
- Adams, W. S. 1941, *ApJ*, 93, 11
- Agúndez, M., Goicoechea, J. R., Cernicharo, J., Faure, A., & Roueff, E. 2010, *ApJ*, 713, 662
- Balick, B., Gammon, R. H., & Doherty, L. H. 1974, *ApJ*, 188, 45
- Bally, J. 2008, *Handbook of Star Forming Regions*, Vol. I (San Francisco, CA: ASP)
- Bally, J., Cunningham, N. J., Moeckel, N., et al. 2011, *ApJ*, 727, 113
- Bally, J., & Zinnecker, H. 2005, *AJ*, 129, 2281
- Barinova, G., & van Hemert, M. C. 2006, *ApJ*, 636, 923
- Bates, D. R. 1951, *MNRAS*, 111, 303
- Beckwith, S., Persson, S. E., Neugebauer, G., & Becklin, E. E. 1978, *ApJ*, 223, 464
- Bergin, E. A. & Herschel Hexos Team 2011, in IAU Symp. 280, *The Molecular Universe*, 93
- Beuther, H., Zhang, Q., Greenhill, L. J., et al. 2004, *ApJL*, 616, L31
- Beuther, H., Zhang, Q., Greenhill, L. J., et al. 2005, *ApJ*, 632, 355
- Black, J. H., & Dalgarno, A. 1973, *ApL*, 15, 79
- Black, J. H., Dalgarno, A., & Oppenheimer, M. 1975, *ApJ*, 199, 633
- Blake, G. A., Sutton, E. C., Masson, C. R., & Phillips, T. G. 1987, *ApJ*, 315, 621
- Boissé, P., Rollinde, E., Hily-Blant, P., et al. 2009, *A&A*, 501, 221
- Boreiko, R. T., & Betz, A. L. 1996, *ApJL*, 467, L113
- Brown, J. M., & Evenson, K. M. 1983, *ApJL*, 268, L51
- Caselli, P., Hasegawa, T. I., & Herbst, E. 1993, *ApJ*, 408, 548
- Chernin, L. M., & Wright, M. C. H. 1996, *ApJ*, 467, 676
- Comito, C., Schilke, P., Phillips, T. G., et al. 2005, *ApJS*, 156, 127
- Cooksy, A. L., Saykally, R. J., Brown, J. M., & Evenson, K. M. 1986, *ApJ*, 309, 828
- Crane, P., Lambert, D. L., & Sheffer, Y. 1995, *ApJS*, 99, 107
- Crawford, I. A. 1995, *MNRAS*, 277, 458
- Crockett, N. R., Bergin, E. A., Neill, J. L., et al. 2014a, *ApJ*, 781, 114
- Crockett, N. R., Bergin, E. A., Neill, J. L., et al. 2014b, *ApJ*, 787, 112
- Cunningham, N. J. 2006, PhD thesis, Univ. Colorado
- Davidson, S. A., Evenson, K. M., & Brown, J. M. 2001, *ApJ*, 546, 330
- de Graauw, T., Helmich, F. P., Phillips, T. G., et al. 2010, *A&A*, 518, L6
- de Vicente, P., Martín-Pintado, J., Neri, R., & Rodríguez-Franco, A. 2002, *ApJL*, 574, L163
- Douglas, A. E., & Herzberg, G. 1941, *ApJ*, 94, 381
- Draine, B. T., & Katz, N. 1986a, *ApJ*, 306, 655
- Draine, B. T., & Katz, N. 1986b, *ApJ*, 310, 392
- Draine, B. T., Roberge, W. G., & Dalgarno, A. 1983, *ApJ*, 264, 485
- Erickson, N. R., Goldsmith, P. F., Snell, R. L., et al. 1982, *ApJL*, 261, L103
- Falgarone, E., Ossenkopf, V., Gerin, M., et al. 2010, *A&A*, 518, L118
- Feng, S., Beuther, H., Henning, T., et al. 2015, *A&A*, 581, A71
- Flower, D. R., & Pineau des Forêts, G. 1998, *MNRAS*, 297, 1182
- Friedel, D. N., & Snyder, L. E. 2008, *ApJ*, 672, 962
- Genzel, R., Reid, M. J., Moran, J. M., & Downes, D. 1981, *ApJ*, 244, 884
- Genzel, R., & Stutzki, J. 1989, *ARA&A*, 27, 41
- Gerin, M., Ruaud, M., Goicoechea, J. R., et al. 2015, *A&A*, 573, A30
- Gerlich, D., Disch, R., & Scherbarth, S. 1987, *JChPh*, 87, 350
- Godard, B., & Cernicharo, J. 2013, *A&A*, 550, A8
- Godard, B., Falgarone, E., Gerin, M., et al. 2012, *A&A*, 540, A87
- Godard, B., Falgarone, E., & Pineau Des Forêts, G. 2009, *A&A*, 495, 847
- Godard, B., Falgarone, E., & Pineau des Forêts, G. 2014, *A&A*, 570, AA27
- Goddi, C., Greenhill, L. J., Humphreys, E. M. L., Chandler, C. J., & Matthews, L. D. 2011, *ApJL*, 739, L13
- Goicoechea, J. R., Chavarría, L., Cernicharo, J., et al. 2015a, *ApJ*, 799, 102
- Goicoechea, J. R., & Le Bourlot, J. 2007, *A&A*, 461, 1
- Goicoechea, J. R., Teyssier, D., Etxaluz, M., et al. 2015b, *ApJ*, 812, 75
- Goldsmith, P. F., & Langer, W. D. 1999, *ApJ*, 517, 209
- Graff, M. M., Moseley, J. T., & Roueff, E. 1983, *ApJ*, 269, 796
- Gredel, R. 1997, *A&A*, 320, 929
- Gredel, R., van Dishoeck, E. F., & Black, J. H. 1993, *A&A*, 269, 477
- Greenhill, L. J., Gwinn, C. R., Schwartz, C., Moran, J. M., & Diamond, P. J. 1998, *Natur*, 396, 650
- Griffin, M. J., Abergel, A., Abreu, A., et al. 2010, *A&A*, 518, L3
- Gupta, H., Rimmer, P., Pearson, J. C., et al. 2010, *A&A*, 521, L47
- Guzmán, V., Roueff, E., Gauss, J., et al. 2012, *A&A*, 548, A94
- Hamilton, J. R., Faure, A., & Tennyson, J. 2016, *MNRAS*, 455, 3281
- Hierl, P. M., Morris, R. A., & Viggiano, A. A. 1997, *JChPh*, 106, 10145
- Hirota, T., Bushimata, T., Choi, Y. K., et al. 2007, *PASJ*, 59, 897
- Indriolo, N., Oka, T., Geballe, T. R., & McCall, B. J. 2010, *ApJ*, 711, 1338
- Johnston, K. J., Stolovy, S. R., Wilson, T. L., Henkel, C., & Mauersberger, R. 1989, *ApJL*, 343, L41
- Keene, J., Schilke, P., Kooi, J., et al. 1998, *ApJL*, 494, L107
- Kester, D., Avruch, I., & Teyssier, D. 2014, in AIP Conf. Proc. 1636, *Bayesian Inference and Maximum Entropy Methods in Science and Engineering*, ed. R. K. Niven et al. (Melville, NY: AIP), 62
- Kramers, H. A., & Ter Haar, D. 1946, *BAN*, 10, 137
- Kristensen, L. E., Ravkilde, T. L., Pineau des Forêts, G., et al. 2008, *A&A*, 477, 203
- Kwan, J., & Scoville, N. 1976, *ApJL*, 210, L39
- Langer, W. D., Graedel, T. E., Frerking, M. A., & Armentrout, P. B. 1984, *ApJ*, 277, 581
- Langer, W. D., & Penzias, A. A. 1990, *ApJ*, 357, 477
- Langer, W. D., & Penzias, A. A. 1993, *ApJ*, 408, 539
- Le Bourlot, J., Le Petit, F., Pinto, C., Roueff, E., & Roy, F. 2012, *A&A*, 541, A76
- Le Petit, F., Le Bourlot, J., Nehmé, C., & Roueff, E. 2006, *ApJS*, 164, 506
- Le Petit, F., Roueff, E., & Herbst, E. 2004, *A&A*, 417, 993
- Levriér, F., Le Petit, F., Hennebelle, P., et al. 2012, *A&A*, 544, A22
- Lim, A. J., Rabadán, I., & Tennyson, J. 1999, *MNRAS*, 306, 473
- Liszt, H., & Lucas, R. 2002, *A&A*, 391, 693
- Liszt, H., Lucas, R., & Pety, J. 2005, in IAU Symp. 231, *Astrochemistry: Recent Successes and Current Challenges*, ed. D. C. Lis et al. (Cambridge: Cambridge Univ. Press), 187
- López-Sepulcre, A., Kama, M., Ceccarelli, C., et al. 2013, *A&A*, 549, A114
- Mathis, J. S., Rumpl, W., & Nordsieck, K. H. 1977, *ApJ*, 217, 425

- McKellar, A. 1940, *PASP*, **52**, 312
- Menten, K. M., & Reid, M. J. 1995, *ApJL*, **445**, L157
- Menten, K. M., Reid, M. J., Forbrich, J., & Brunthaler, A. 2007, *A&A*, **474**, 515
- Menten, K. M., Walmsley, C. M., Henkel, C., et al. 1986, *A&A*, **169**, 271
- Menten, K. M., Walmsley, C. M., Henkel, C., & Wilson, T. L. 1988, *A&A*, **198**, 253
- Müller, H. S. P. 2010, *A&A*, **514**, L6
- Müller, H. S. P., Goicoechea, J. R., Cernicharo, J., et al. 2014, *A&A*, **569**, L5
- Müller, H. S. P., Schlöder, F., Stutzki, J., & Winnewisser, G. 2005, *JMoSt*, **742**, 215
- Nagy, Z., Van der Tak, F. F. S., Ossenkopf, V., et al. 2013, *A&A*, **550**, A96
- Nehmé, C., Gry, C., Boulanger, F., et al. 2008, *A&A*, **483**, 471
- Neufeld, D. A. 2012, *ApJ*, **749**, 125
- Neufeld, D. A., Schilke, P., Menten, K. M., et al. 2006, *A&A*, **454**, L37
- Ossenkopf, V., Röllig, M., Neufeld, D. A., et al. 2013, *A&A*, **550**, A57
- Pan, K., Federman, S. R., Cunha, K., Smith, V. V., & Welty, D. E. 2004, *ApJS*, **151**, 313
- Pearson, J. C., & Drouin, B. J. 2006, *ApJL*, **647**, L83
- Peng, T.-C., Wyrowski, F., Zapata, L. A., Güsten, R., & Menten, K. M. 2012a, *A&A*, **538**, A12
- Peng, T.-C., Zapata, L. A., Wyrowski, F., Güsten, R., & Menten, K. M. 2012b, *A&A*, **544**, L19
- Persson, C. M., Olofsson, A. O. H., Koning, N., et al. 2007, *A&A*, **476**, 807
- Phillips, T. G., Bergin, E. A., Lis, D. C., et al. 2010, *A&A*, **518**, L109
- Pickett, H. M., Poynter, R. L., Cohen, E. A., et al. 1998, *JQSRT*, **60**, 883
- Pilbratt, G. L., Riedinger, J. R., Passvogel, T., et al. 2010, *A&A*, **518**, L1
- Plambeck, R. L., Wright, M. C. H., Friedel, D. N., et al. 2009, *ApJL*, **704**, L25
- Plume, R., Bergin, E. A., Phillips, T. G., et al. 2012, *ApJ*, **744**, 28
- Poglitsch, A., Waelkens, C., Geis, N., et al. 2010, *A&A*, **518**, L2
- Polehampton, E. T., Menten, K. M., Brünken, S., Winnewisser, G., & Baluteau, J.-P. 2005, *A&A*, **431**, 203
- Rangwala, N., Maloney, P. R., Glenn, J., et al. 2011, *ApJ*, **743**, 94
- Rangwala, N., Maloney, P. R., Glenn, J., et al. 2014, *ApJ*, **788**, 147
- Roelfsema, P. R., Helmich, F. P., Teyssier, D., et al. 2012, *A&A*, **537**, A17
- Röllig, M., & Ossenkopf, V. 2013, *A&A*, **550**, A56
- Röllig, M., Ossenkopf, V., Jeyakumar, S., Stutzki, J., & Sternberg, A. 2006, *A&A*, **451**, 917
- Schöier, F. L., van der Tak, F. F. S., van Dishoeck, E. F., & Black, J. H. 2005, *A&A*, **432**, 369
- Schulz, A., Henkel, C., Beckmann, U., et al. 1995, *A&A*, **295**, 183
- Shaw, G., Ferland, G. J., Srianand, R., & Abel, N. P. 2006, *ApJ*, **639**, 941
- Sheffer, Y., Rogers, M., Federman, S. R., et al. 2008, *ApJ*, **687**, 1075
- Stäuber, S., & Bruderer, S. 2009, *A&A*, **505**, 195
- Sternberg, A., & Dalgarno, A. 1989, *ApJ*, **338**, 197
- Sternberg, A., & Dalgarno, A. 1995, *ApJS*, **99**, 565
- Turpin, F., Stoecklin, T., & Voronin, A. 2010, *A&A*, **511**, A28
- van der Tak, F. F. S., Black, J. H., Schöier, F. L., Jansen, D. J., & van Dishoeck, E. F. 2007, *A&A*, **468**, 627
- van der Tak, F. F. S., Nagy, Z., Ossenkopf, V., et al. 2013, *A&A*, **560**, 95
- van der Werf, P. P., Goss, W. M., & O'Dell, C. R. 2013, *ApJ*, **762**, 101
- van der Werf, P. P., Isaak, K. G., Meijerink, R., et al. 2010, *A&A*, **518**, L42
- van der Werf, P. P., Stutzki, J., Sternberg, A., & Krabbe, A. 1996, *A&A*, **313**, 633
- van Dishoeck, E. F., & Black, J. H. 1986, *ApJS*, **62**, 109
- Visser, R., Kristensen, L. E., Bruderer, S., et al. 2012, *A&A*, **537**, A55
- Wang, S., Bergin, E. A., Crockett, N. R., et al. 2011, *A&A*, **527**, AA95
- Weilbacher, P. M., Monreal-Ibero, A., Kollatschny, W., et al. 2015, *A&A*, **582**, A114
- White, R. E. 1984, *ApJ*, **284**, 685
- Wilson, T. L., Johnston, K. J., Henkel, C., & Menten, K. M. 1989, *A&A*, **214**, 321
- Wilson, T. L., Muders, D., Kramer, C., & Henkel, C. 2001, *ApJ*, **557**, 240
- Woodall, J., Agúndez, M., Markwick-Kemper, A. J., & Millar, T. J. 2007, *A&A*, **466**, 1197
- Xu, L.-H., & Lovas, F. J. 1997, *JPCRD*, **26**, 17
- Zanchet, A., Godard, B., Bulut, N., et al. 2013, *ApJ*, **766**, 80
- Zapata, L. A., Schmid-Burgk, J., & Menten, K. M. 2011, *A&A*, **529**, A24
- Zapata, L. A., Schmid-Burgk, J., Muders, D., et al. 2010, *A&A*, **510**, A2
- Zsargó, J., & Federman, S. R. 2003, *ApJ*, **589**, 319
- Zuckerman, B., Kuiper, T. B. H., & Rodríguez Kuiper, E. N. 1976, *ApJL*, **209**, L137